



UNIVERSITY OF NAPLES FEDERICO II

DEPARTMENT OF INDUSTRIAL ENGINEERING

- MECHANIC AND ENERGETIC SECTION -

PH.D. SCHOOL IN INDUSTRIAL ENGINEERING – XXXII CYCLE

INTERNAL COMBUSTION ENGINE BASE CALIBRATION: COMPUTER AIDED TOOLS AND METHODOLOGIES FOR THE EXPERIMENTAL EFFORT REDUCTION

Doctoral Thesis

Ph.D. School Coordinator

prof. Michele Grassi

Tutor

prof. Alfredo Gimelli

ing. Massimiliano Muccillo

ing. Francesco de Nola (Teoresi SPA)

Ph.D. Candidate

Giovanni Giardiello

Contents

LIST OF FIGURES	III
LIST OF TABLES	VII
ABBREVIATION AND NOMENCLATURE	VIII
ABSTRACT	1
INTRODUCTION	3
1. ENGINE ELECTRONIC CONTROL UNIT	1
1.1. STRUCTURE OF AN ELECTRONIC CONTROL UNIT	4
1.2. STRUCTURE OF AN ECU FUNCTION: MAPS, VECTORS, SCALARS	6
1.3. ENGINE CONTROL MODULE OPERATION	8
1.4. BASE ENGINE CALIBRATION PROCESS	9
2. COMPUTER AIDED CALIBRATION: MAIN STAGES AND CALIBRATION PERFORMANCES	14
2.1. APPLICATION OF THE REGRESSION TECHNIQUE TO THE CALIBRATION OF THE VOLUMETRIC EFFICIENCY FUNCTION	17
2.2. APPLICATION OF THE REGRESSION TECHNIQUE TO THE TARGET THROTTLE ANGLE FUNCTION	19
3. NEURAL NETWORKS: RADIAL BASIS FUNCTION	27
3.1. THE PROPOSED METHODOLOGY: NEURAL NETWORKS APPLIED TO THE ENGINE CALIBRATION PROCESS	33
3.2. ANALYSIS AND RESULTS: APPLICATION OF THE METHODOLOGY TO THE CALIBRATION OF THE VOLUMETRIC EFFICIENCY FUNCTION	35
3.3. ANALYSIS AND RESULTS	39
4. SECOND PROPOSED METHODOLOGY: 0D-1D ENGINE MODEL APPLIED TO THE ENGINE CALIBRATION PROCESS	44
4.1. 0D/1D EQUATIONS: VOLUMES AND PIPES	46
4.2. 0-D COMBUSTION AND TURBULENCE MODEL	51
4.3. THERMAL EXCHANGE MODEL	56
4.4. VALVE MODEL	56
4.5. FRICTION MODEL	57
4.6. PID CONTROLLER MODEL	58
5. ENGINE DESCRIPTION AND OPTIMIZATION	61
5.1. ENGINE ARCHITECTURE	61
5.2. ENGINE MODELLING	62
5.3. OPTIMIZATION – MOGA	67
5.3.1. Calibration of the friction model	71
5.3.2. Calibration of the throttle model	72
5.3.3. General multi-variable multi-objective methodology applied to the engine model: MOGA	74

5.3.4. Validation 5x18.....	78
5.3.5. Validation 5x30.....	80
5.3.6. Validation 5x96.....	82
5.4. ANALYSIS AND RESULTS OF THE VALIDATIONS	84
6. DEVELOPMENT OF EXPERIMENTAL CAMPAIGN THOUGHT THE USE OF VALIDATED 1D-0D ENGINE MODEL.....	88
6.1. DESCRIPTION OF THE ENGINE CALIBRATION WITH 1D SIMULATION	88
6.2. DEVELOPMENT OF EXPERIMENTAL CAMPAIGN: STRATEGY A	88
6.3. DEVELOPMENT OF EXPERIMENTAL CAMPAIGN: STRATEGY B	90
6.4. ANALYSIS AND RESULTS.....	92
7. CONCLUSIONS AND FUTURE DEVELOPMENT	99
REFERENCES	101

List of figures

Figure 0.1 - Mechatronic components and systems for automobiles and engines [1]	3
Figure 0.2 - main stages of the base engine calibration process	4
Figure 0.3 - Measurements for step inputs. a stationary behavior (steady state). b dynamic behavior [1].....	5
Figure 1.1 - timeline of some of the most important events concerning the evolution of the vehicle	1
Figure 1.2 - example of the various types of ECM on board the vehicle [26].....	2
Figure 1.3 - Visual comparison between a multi-wire configuration and a CAN-BUS configuration	3
Figure 1.4 – schematization of the structure of an ECU	4
Figure 1.5 – schematization of the structure of an ECM	5
Figure 1.6 – schematization of the function (2)	7
Figure 1.7 – structure of map c after the calibration	7
Figure 1.8 – map c before the calibration.....	8
Figure 1.9 – schematization of the ECM functioning	9
Figure 1.10 – timeline of the design and development of a new vehicle	10
Figure 1.11 – schematization of the traditional engine base calibration process	12
Figure 1.12 – structure of a datasheet.....	13
Figure 2.1 – main steps of the computer aided calibration software.....	14
Figure 2.2 - Mass-spring-damper analogy adopted for the discrete regression technique within the proposed calibration tool.....	16
Figure 2.3 – error distribution for the uncalibrated function.....	18
Figure 2.4 – error distribution for the calibrated function.....	19
Figure 2.5. Schematic representation of the function providing the throttle angle as a function of the mass flow rate and pressure ratio.	20
Figure 2.6. Mass flow through an orifice.	21
Figure 2.7. De Saint Venant model optimization scheme.....	23
Figure 2.8. Correlation of the error with the mass flow rate	24
Figure 2.9. Calibration scheme adopted for the vector quantity A_{DSV} in the updated version of the DSV model.....	24

Figure 2.10. Results of regression analysis performed on the updated version of the throttle angle model.....	25
Figure 2.11. Throttle angle map: comparison between the oversimplified (grey surface) and updated version of the model (colored)	26
Figure 2.12. Distributions of the error for the throttle angle estimation: simplified model (on the left) and updated model (on the right).	26
Figure 3.1 - Trends of the Gaussian radial function (green) and the Multiquadratic function (magenta).	30
Figure 3.2 – schematization of the structure of an ANN	31
<i>Figure 3.3 - Regression example with Gaussian RBF for the points of a generic training set. ...</i>	32
Figure 3.4 - spread factor influence	32
Figure 3.5 - Detailed scheme of the enhanced calibration methodology.	34
Figure 3.6 - Structure of a neural network with specification of the ECU engine quantities adopted within the input and output layers.....	35
Figure 3.7 - Error distribution for the volumetric efficiency after a 40% cut of the original datasheet.....	37
Figure 3.8 - Error distribution for the volumetric efficiency after a 70% cut of the original datasheet.....	38
Figure 3.9 - error distribution for the calibrated volumetric efficiency function using a datasheet containing 660 experimental conditions	39
Figure 3.10 - Error distributions for the volumetric efficiency function: calibration achieved by using NN methodology after a 40% cut.....	40
Figure 3.11 - Response surfaces for the parameter “a” obtained from the original data set and NN recalculation.....	40
Figure 3.12 - Error distributions for the volumetric efficiency function: calibration achieved by using NN methodology after a 50% cut (on the left) and 60% cut (on the right) of the original data set.	41
Figure 3.13 - Response surfaces for the parameter “a” obtained from the original data set and NN recalculation after a 60% cut of the original datasheet.	42
Figure 4.1 – main stages of the proposed methodology.....	44
Figure 4.2 – 0D cylinder schematization	48
Figure 4.3 – 1D pipe schematization.....	49
Figure 4.4 – Wiebe heat release law trend	52
Figure 4.5 – 0D cylinder schematization with 2-zone approach.....	53

Figure 4.6 - Schematic representation of the model adopted for the turbulent combustion	54
Figure 4.7 – schematization of the PID controller operation	59
Figure 5.1 – 0D-1D engine schematization.....	63
Figure 5.2 – schematization of the piston-rod-crank mechanism	66
Figure 5.3 - schematization of the combustion chamber.....	67
Figure 5.4 - comparison between trends of some experimental quantities (in black) and those obtained from the model (in red)	70
Figure 5.5 - Calibration achieved for the Chen-Flynn model.	71
Figure 5.6 – schematization of the throttle model.....	73
Figure 5.7 - values of cD vs the opening angle of the throttle valve obtained at the end of the calibration.....	74
Figure 5.8 – schematization of the automated engine model validation process.....	76
Figure 5.9 - comparison between trends of some experimental quantities (in black), numerical quantities using a heuristic validation (in red) and numerical quantities using the validation 5x18 .	79
Figure 5.10 - comparison between trends of some experimental quantities (in black), numerical quantities using a heuristic validation (in red), using a validation 5x18 (in green) and using a validation 5x30 (in blue).....	81
Figure 5.11 - comparison between trends of some experimental quantities (in black), numerical quantities using a heuristic validation (in red), using a validation 5x18 (in green), using a validation 5x30 (in blue) and using a validation 5x96 (in purple).....	83
Figure 5.12 – total mean error using different validation.....	85
Figure 5.13 - total mean error relating to some quantities not used as objective parameters in the validation procedure: volumetric efficiency (left) and fuel mass flow rate (right).....	86
Figure 5.14 - total mean error relating to some quantities not used as objective parameters in the validation procedure: top dead center pressure (left) and manifold pressure (right)	86
Figure 5.15 – trend of the manifold pressure: experimental data (black), validation 5x18 (green), validation 5x30 (blue) and validation 5x96 (purple)	87
Figure 6.1 – 0D-1D engine configuration for Strategy A	89
Figure 6.2 – valve lifts used in different engine conditions	90
Figure 6.3 - 0D-1D engine configuration for Strategy B	91
Figure 6.4 - Comparison between experimental and calculated mean data for Strategy A.	92
Figure 6.5 - Comparison between experimental and calculated mean data for Strategy B.	93
Figure 6.6 - Comparison between experimental and calculated torque at 4400 rpm for the two strategies.....	93

Figure 6.7 – occurrence of the volumetric efficiency function error using the experimental datasheet.....94

Figure 6.8 - occurrence of the volumetric efficiency function error using the virtual datasheet..95

Figure 6.9 – effect of engine speed variation on the valve lift.....97

List of tables

Table 2.1 – characteristics of the engine equipped with the volumetric efficiency function.....	17
Table 3.1 - Errors achieved for the volumetric efficiency obtained by NN after a 40% cut of the original datasheet.	36
Table 3.2 - Errors achieved for the volumetric efficiency obtained by NN after a 70% cut of the original datasheet.	37
Table 4.1 - Classification of the numerical approaches and typical application.....	46
Table 5.1 – main characteristics of the engine used for the 0D-1D modelling.....	62
Table 5.2 - geometrical characteristics of the pipes used in the model.....	64
Table 5.3 – sizes of volumes used in the engine model	65
Table 5.4 - geometrical characteristics of the combustion chamber	66
Table 5.5 – operating conditions used for the validation	67
Table 5.6 - error reached by a comparison between experimental data and numerical quantities using a heuristic validation	68
Table 5.7 - error achieved by a comparison between experimental data and numerical quantities using a heuristic calibration at 3000 rpm	69
Table 5.8 – Calibration parameters values achieved for the Chen-Flynn model	71
Table 5.9 – operating conditions used for the calibration of the throttle model	73
Table 5.10 – values of the decision variables reached at the end of the validation 5x18	78
Table 5.11 - error reached by a comparison between experimental data and numerical quantities after the validation 5x18	80
Table 5.12 - values of the decision variables reached at the end of the validation 5x30	80
Table 5.13 - error reached by a comparison between experimental data and numerical quantities after the validation 5x30	82
Table 5.14 - values of the decision variables reached at the end of the validation 5x96	82
Table 5.15 - error reached by a comparison between experimental data and numerical quantities after the validation 5x96	84
Table 6.1 - extract of the datasheet that highlights the pressure upstream and downstream of the throttle valve	96

Abbreviation and nomenclature

A_{cls}	closing angle of the throttle valve
A_L	surface of discontinuity between burned and unburned gases
$A_{ref,v}$	valve reference area
A_{ref}	constant reference section
A_{thr}	effective section set by the throttle
A_{tot}	section of the pipe
C	calibration parameter
c_D	throttle valve flow coefficient
c_{dc}	popped valve flow coefficient
c_{dw}	valve discharge coefficient
c_p	specific heat at constant pressure
c_v	specific heat at constant volume
c_w	equivalent velocity of the fluid
D	cylinder bore
E	total internal energy per unit mass
$err\%$	percentage error of the volumetric efficiency
F_w	calibration coefficient of the heat exchanges
\mathbf{H}	matrix of all the RBF
H	total enthalpy per unit mass
h_w	coefficient of conductive heat exchange
\mathbf{h}_j	basis function
K	Springer stiffness
m_b	burned mass
m_e	encapsulated mass

m	characteristic exponent
M_{AIR}	air mass trapped within the engine cylinder
M_{REF}	theoretical trapped air mass in the cylinder
p	pressure
p_{amb}	environment pressure
p_{eg}	exhaust gas pressure
$PRES$	value of the manifold pressure
Q_{EXP}	Experimental quantity
Q_{EST}	quantity estimated by the ECU
\dot{Q}_w	thermal power
R	universal gas constant
RPM	engine speed
S_L	flame laminar speed
S_T	flame turbulent speed
StD	Standard Deviation
T	initial training set
T_{amb}	environment temperature
T_{AIR}	air temperature
u	flow velocity
U_{ref}	reference speed of the induced air at ambient conditions
V_c	engine displacement
V_{cc}	combustion chamber volume
VOL_{EFF}	volumetric efficiency evaluated by the ECU
$VOL_{EFF_{TB}}$	volumetric efficiency evaluated at bench test
VVT	angle of valve closing

Acronyms

ACS	Automated Calibration Software
ABS	Anti Block System
BCM	Brake control module
CAE	Computer Aided Engineering
CAN	Control Area Network
CO	carbon monoxide
EGR:	Exhaust Gas Recirculation
EVS	Engine Verification Software
DSV	De Saint Venat flow model
GDI	Gasoline Direct Injection
ECU	Electronic Control Unit
EECM	Engine Electronic Control Unit
DoE	Design of Experiment
GDI	Gasoline Direct Injection
NN	Neural Networks
NMHC	non-methane hydrocarbons
NOx	nitrogen oxides
MSE	Mean Squared Error
PCM	Powertrain Control Module
PM	particulate matter
RBF	radial basis function
SCM	suspension control module
SSE	sum of the squared errors
THC	total hydrocarbon

VVA: Variable Valve Actuation

Greek symbols

β	pressure ratio
θ_{cls}	angle at the closed throttle
θ_{geo}	geometric throttle angle
θ_{ecu}	throttle angle measured by the ECU
γ	the adiabatic expansion coefficient
λ	front thickness
ρ	density of the mixture
ρ_{ref}	density of the induced air at ambient conditions
τ	chemical reaction time
ω_j	neural networks weights

Subscripts

Abstract

Over the last decades, internal combustion engines have undergone a continuous evolution to achieve better performance, lower pollutant emissions and reduced fuel consumption. The pursuit of these often-conflicting goals involved changes in engine architecture in order to carry out advanced management strategies. Therefore, Variable Valve Actuation, Exhaust Gas Recirculation, Gasoline Direct Injection, turbocharging and powertrain hybridization have found wide application in the automotive field. However, the effective management of such a complex system is due to the contemporaneous development of the on-board Engine Electronic Control Unit. In fact, the additional degrees of freedom available for the engine regulation highly increased the complexity of engine control and management, resulting in a very expensive and long calibration process. Indeed, the functions of the engine control units are calibrated trying to reduce the error between the quantity obtained from the ECU algorithms and the experimental quantity in a wide range of engine working conditions. To this aim, extensive experimental campaigns are carried out on the test bench, in which thousands of operating conditions are analyzed, resulting in high costs for the realization of the process. *Figure - A* schematizes the traditional base engine calibration process.

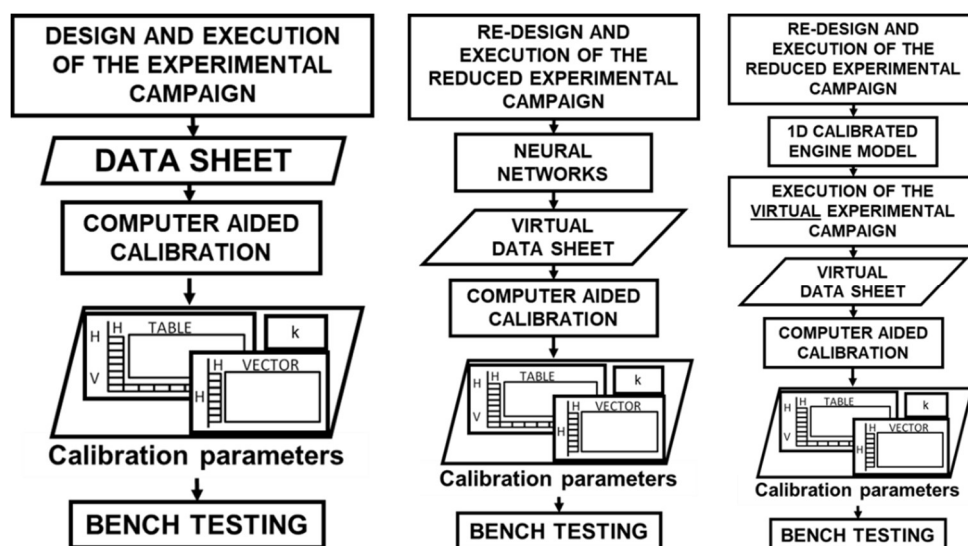


Figure - A - main stages of the traditional base engine calibration process (on the left), and the proposed methodologies (on the center and on the right)

With the aim to overcome the above issues, two methodologies have been investigated. The purpose of the proposed methodologies is to reduce the number of the experimental bench tests without reducing the performance of the control unit functions.

A first effective methodology is based on the use of Neural Networks (NN) to overcome some critical issues concerning the calibration of engine control parameters. NN are adopted to provide a detailed engine data sheet starting from a reduced number of experimental data. The potential of the proposed methodology has been verified using this detailed data set as input to a specific Computer Aided Calibration algorithm developed in this work and evaluating the achievable calibration performance. In particular, the calibration performance has been assessed with reference to a specific ECU function. The research clearly demonstrates the effectiveness of the proposed approach since the calibration performance falls within acceptable limits even after a 60% cut of the experimental data usually acquired for calibration purposes, highlighting how the use of neural networks can allow a significant reduction of the experimental effort along with its related times and costs.

A second methodology based on the adoption of 1D thermo-fluid dynamic analysis is proposed. In particular, starting from a complete experimental set of data currently used for the base calibration of a reference spark ignition engine, a novel procedure based on vector optimization approach is used to reliably calibrate a 1D engine model starting from a reduced experimental dataset. Once validated, the engine model is used as a virtual test bench to reproduce the experimental campaign numerically, thus obtaining a detailed and complete dataset exploitable for calibration purposes, here called numerical or virtual dataset. The potential of the proposed methodology has been verified by comparing the experimental and virtual dataset. The research clearly demonstrates the effectiveness of the proposed approach since the mean errors are comparable with the measurement errors. Therefore, the methodology shows promising results concerning the use of numerical dataset obtained from reliable 1D CFD engine models as input to computer aided calibration software. In this way, a significant cut to the experimental campaign required for calibration purposes is achieved, with their related times and costs.

Introduction¹

Object of this Thesis work is the development of methodologies that may lead to a reduction in the costs of carrying out the base engine calibration process through a reduction in experimental tests. The calibration process is an industrial process used by a small number of actors such as large car manufacturers, who tend not to share their processes, resulting in a lack of literature. However, the information in this Thesis is common to all the base calibration processes used by car manufacturers. In fact, the process cannot be separated from an intense experimental campaign, in which the engine is placed on a test bench and realizes thousands of operating conditions, resulting in high construction costs. The ultimate goal of this process is to calibrate the electronic control units that manage and control the engine: they now play a fundamental role in the evolution of the engine and vehicle.

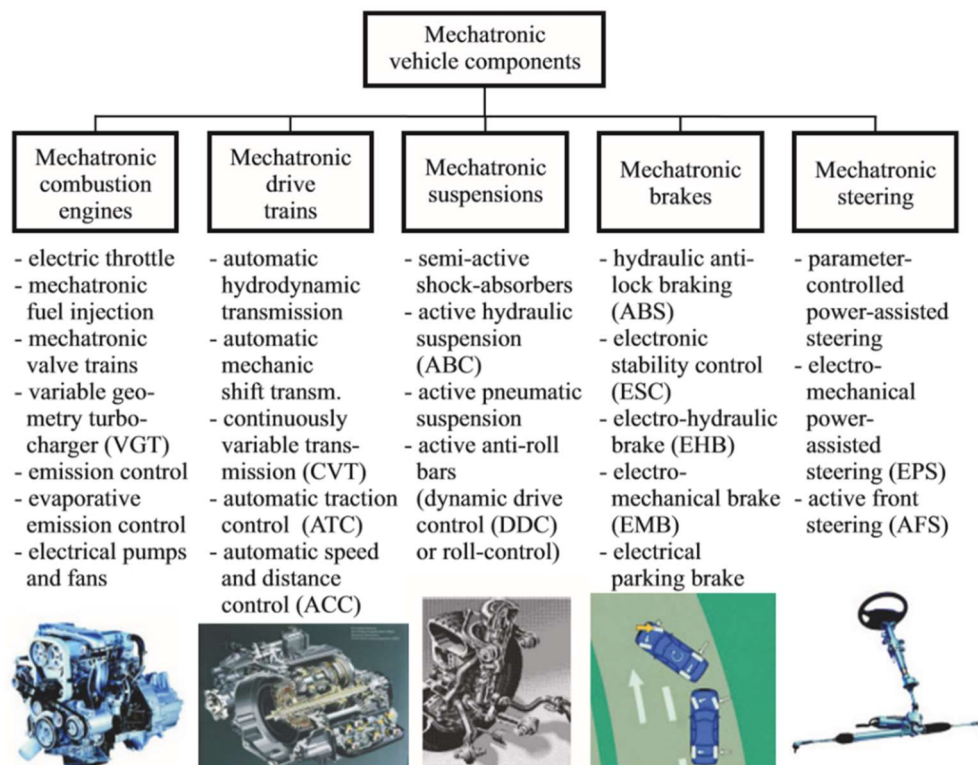


Figure 0.1 - Mechatronic components and systems for automobiles and engines [1]

The increasing electronification and electrification is a dominant feature of modern automotive developments. This is demonstrated by an increasing part of electrics/electronics of the manufacturing costs from about 20% in 1995 to 35% in 2012 [1].

¹ Much of the information that appears in this introduction comes from [1]. It is a complete guide on internal combustion engine control and management systems.

The development of sensors, actuators and electronic control for automobiles is depicted in *Figure 0.1*. Moreover, there has been an increase in devices, sensors and/or actuators, mounted onboard the vehicle, thanks also to the development of bus systems such as the CAN bus network. This evolution is strictly connected to the improvements of the combustion, fuel consumption and emission reductions.

The main tasks of the electronic engine control unit (ECU) deals with the control, optimization and the supervision of all the relevant functions of an internal combustion engine trying to achieve simultaneously these goals:

- torque generation according to the driver's accelerator pedal
- low fuel consumption
- low exhaust emissions and low noise (compliance with legislation)
- good driving behavior.

The control unit functions must be optimized and calibrated in order to ensure the achievement of these objectives. In particular, the estimation and the target functions modeled in the engine electronic control unit, must be able to recreate experimental quantities over the entire operating range of the engine. The functions are calibrated by reducing the error assessed as the difference between the quantity obtained from the function and the experimental quantity under the same operating conditions. The greater the number of conditions in which the error is reduced, the more reliable the calibrated function will be.

An appropriate test bench and a computer-based development environment are fundamentals in order to carry out a basic experimental test.

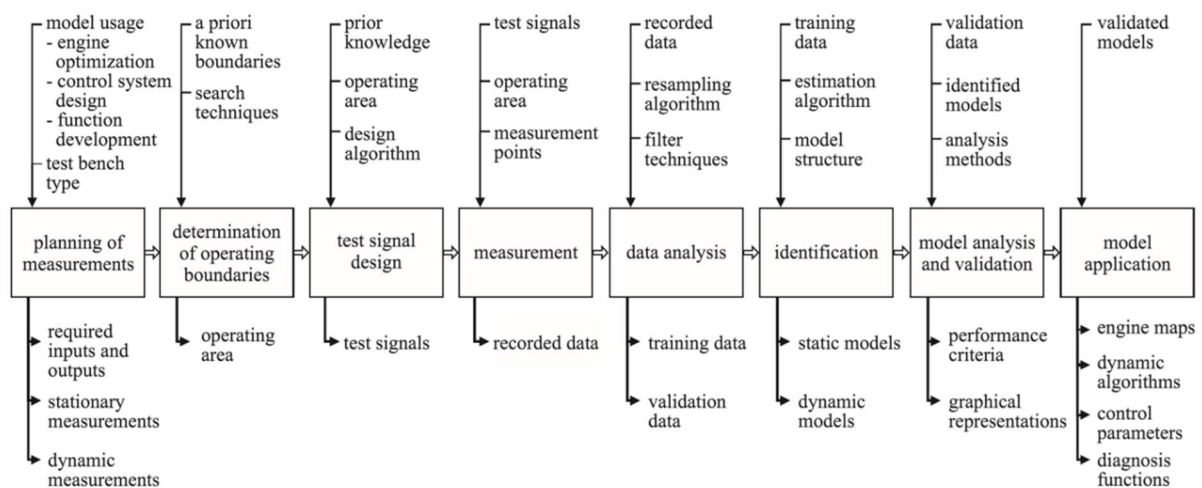


Figure 0.2 - main stages of the base engine calibration process

The *Figure 0.2* shows a general procedure for the experimental modeling (identification) of engines on test benches, and it's an expose of the steps represented in the *Figure 1.11*.

According to the functions to be calibrated, it is necessary to choose the points to be analysed on the test bench, determining the operating limits of the engine in order to avoid damages. The choice of points to analyse also depends on other factors such as the type of control (e.g. speed or torque control) or if it is preferred to perform a stationary or dynamic test.

The measurements therefore can be carried out by measuring a large number of experimental quantities, both input and output, also decided a priori. They are stored in a datasheet. Then the data should be analyzed before they are used for experimental modeling. For example, graphical tools are used to check for consistency of the data and to remove outliers. There are various methods for choosing the points to be analysed on the test bench over the entire operating range of the engine, both in the stationary and in the dynamic case, for example using DoE techniques [2] [3] or reduced grid measurement [4]. In recent years, there is a growing interest in dynamic testing and modelling of the dynamic behaviour. The reason is to optimize the dynamic behaviour of the engine in order, for example, to reduce pollutant emissions during an acceleration phase. About 50% of the emissions in the NEDC or FTP75 driving cycles result from acceleration states.

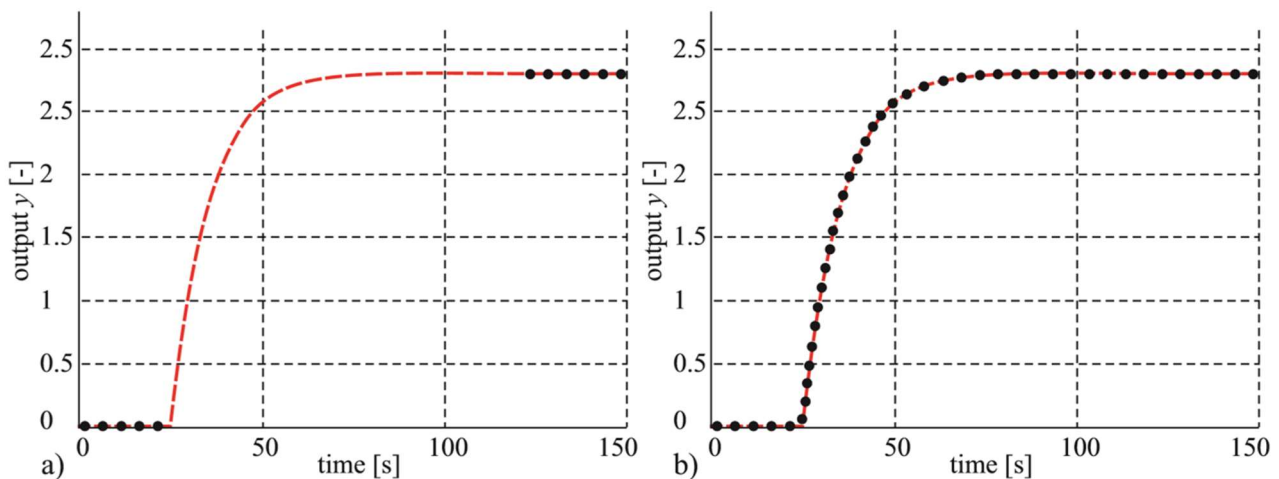


Figure 0.3 - Measurements for step inputs. a stationary behavior (steady state). b dynamic behavior [1]

The figure shows the difference in acquisitions between a stationary test and a dynamic test. After analysing the congruence of the experimental data, the functions to be calibrated are identified. The knowledge of the structure of the models to be calibrated, whether it is grey-box or black-box, static or dynamic models, is fundamental in order to proceed with the validation of the model ensuring that the experimental tests carried out are those necessary for validation. It has to be checked whether

the model complies with the recorded input and output data of the real process. Model validation checks if the obtained models describe the real behavior of the engine, using e.g. performance criteria, such as the sum of least squares of equation errors or map-based performance, for the already measured or additional validation. In this phase, as explained in detail in the following chapters, the calibration of the scalars, vectors and maps of the control unit functions takes place.

The process described requires the need to carry out thousands of experimental tests to calibrate the control unit functions which will then be used for the subsequent phases such as engine and vehicle optimization.

The aim of this thesis is to develop methodologies that allow reducing the number of experimental tests necessary for the base calibration of the control unit functions, resulting in a reduction in the costs of the entire process. Two methodologies will be described:

- The first methodology consists in the use of neural networks (NN) in order to extend the experimental tests in operating conditions that have not been explored, involving the generation of datasheets which are formed partly by real operating conditions and partly by virtual operating conditions recreated through neural networks. In this way, with the same amount of operating conditions used to calibrate the functions, fewer real acquisitions carried out on the test bench are required. Their field of application is wide, covering the following different topics: control systems, medicine, robotics, power systems, manufacturing, optimization, signal processing, social and psychological sciences [5]. The use of NN in the automotive field is more recent [6] [7] [8] and mainly concerned the prediction of performance and emissions of internal combustion engines [9]. For example, in [10] the author investigates the capability of neural networks to estimate the intake mass flow rate of an intercooled turbocharged Diesel engine, demonstrating how results from NN model are close to the experimental data. In [11], the authors propose a neural network modelling to predict different emission and combustion performance of a light-duty diesel engine. In [12], the authors used NN to estimate soot and NO_x emissions as a function of several combustion parameters. Moreover, the effects of different topological configurations and training algorithms of the NN have been analysed. A neural network model to predict torque and brake specific fuel consumption of a gasoline engine has been proposed in [13]. Similar applications of NN can also be found in [14] [15] [16] [17], while more control-oriented models are discussed in [18] [19]. However, despite the extensive use of neural networks, NN have not been used yet to provide mixed experimental-numerical data sheets usefully adopted as input to calibration software in base calibration applications.

- The second method consists in using of 1D-0D simulation models of the engine. In this case, a validated and robust model of the engine is used as a virtual test bench with which it is possible to carry out the experimental tests and obtain all the quantities necessary for the calibration of the control unit functions. In this way, it's possible to limit test bench acquisitions to those that are strictly required for the validation of the 1D-0D model. The use of thermo-fluid-dynamic simulation models is also widely used in the automotive sector: they are used for the analysis of physical phenomena such as noise prediction [20], for the modelling of combustion, for the analysis of the scavenging [21], for the prediction of harmful phenomena such as the knock [22]. Another effective use is the optimization of engine control to improve performance or reduce fuel consumption and emissions [23] [24]. In addition, another application is the use of numerical models for the analysis and optimization of the vehicle. The use of thermo-fluid-dynamic simulation in the basis engine calibration has not yet been explored as demonstrated also by a lack of scientific literature.

Both methodologies will be widely described, paying attention to the tools used and the results obtained.

1. Engine Electronic Control Unit

Throughout its history, the vehicle has undergone continuous evolution. As shown in *Figure 1.1*, this evolution concerned the improvement of on-board comfort, the improvement of safety and the increase in power and the reduction of fuel consumption and pollutants. It is interesting to note that this evolution has been guided over the years by different motivations and guidelines. In the early twentieth century until the 1960s, research has been focused on increasing engine performance and improving vehicle comfort.

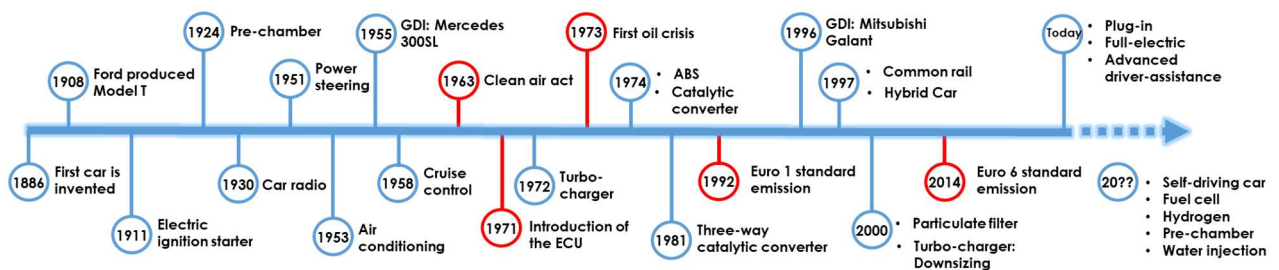


Figure 1.1 - timeline of some of the most important events concerning the evolution of the vehicle²

1963 is an important date, as the "Clean air act" was issued in California [25], which is one of the United States' first and most influential modern environmental laws, and one of the most comprehensive air quality laws in the world. This law is important not so much for the immediate consequences, but because the problem of pollutant emissions is raised for the first time. The 70s is an important transition period. The energy crises of 1973 and 1979 led to a sharp increase in the price of oil: research in the automotive sector adapted accordingly, pushing towards solutions that reduce fuel consumption, without focusing on performance. Finally, in the 90s, the growing demand for a reduction of pollutant emissions, also thanks to a greater awareness of the public opinion, pushed towards solutions that aimed for this purpose. The first European pollutant standards law, called Euro I, was issued in 1992. In the European Union emissions of nitrogen oxides (NO_x), total hydrocarbon (THC), non-methane hydrocarbons (NMHC), carbon monoxide (CO) and particulate matter (PM) are regulated for most vehicle types, including cars, trucks (lorries), locomotives, tractors and similar vehicles, barges, but excluding seagoing ships and aeroplanes. For each vehicle type, different standards are applied. Compliance is determined by running the engine on a standardised test cycle. Non-compliant vehicles cannot be sold in the EU, but new standards do not apply to vehicles already

² graph built on the basis of data found in literature

on the roads. No use of specific technologies is mandated to meet the standards, though available technology is considered when setting the standards. Along with Emissions standards the European Union has also mandated a number of computer on-board diagnostics for the purposes of increasing safety for drivers. In recent years, the development of on-board electronics has made it possible to pursue the three major objectives of research in the automotive sector simultaneously. Thanks to the development of on-board electronics, it is possible to control increasingly complex physical phenomena in an ever more precise way. Interestingly, the first car equipped with GDI was a Mercedes 300SL in 1955. Although potentials have been glimpsed, this solution was abandoned because the techniques to precisely control this phenomenon were lacking. The GDI came back into vogue in 1996 when this solution was re-proposed on a Mitsubishi Galant, because the development of electronics had made it possible to control the phenomenon of direct injection for SI engines.

In a similar way, the "rediscoveries" of the turbocharger and the prechamber must be considered. Originally, these solutions were designed to improve the performance of the vehicle whereas today they have been revisited in the broader perspective of reducing consumption and emissions by maintaining high performance thanks to the development of the control strategies.

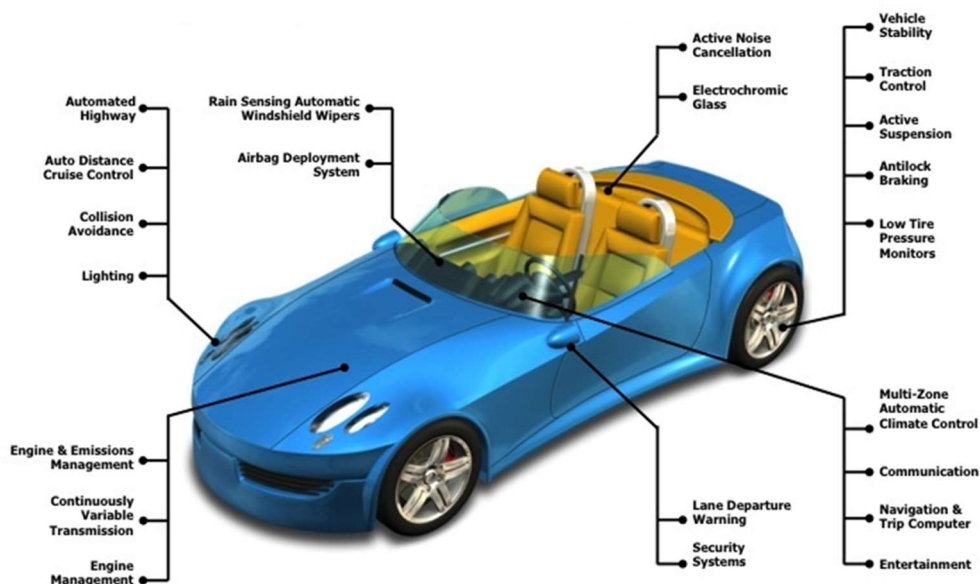


Figure 1.2 - example of the various types of ECM on board the vehicle [26]

It can be said that the biggest automotive revolution in terms of control strategies dates back to 1971 with the introduction of the first simple on-board Electronic Control Unit (ECU). It has played

a fundamental role in evolution of Automobiles from being a completely mechanical to an electronics dominated device.

As shown in *Figure 1.2*, modern cars have dozens of ECUs (up to 150) for specific tasks and control of all devices (engine, brakes, air conditioning, driving assistance ...). Each device takes on its own intelligence, making many operations automatic. Some control units deal with safety: they allow to have a better control of the vehicle, in conditions of low grip (ABS) and to reduce the possibility of serious damage to the driver and passengers by operating in extreme cases a series of airbags, perhaps after having tightened the seat belts. Other electronic control units control the locks, the windscreen wiper that adapts its speed to the intensity of the rain, the lights that turn on automatically when the available light decreases. The presence of intelligence on all the various devices allows for complex functions. To obtain these functions, all the various devices must be interconnected. If on a modern vehicle every necessary connection was made ad hoc, the number of connections, and therefore of wires, on the vehicle would be enormous.

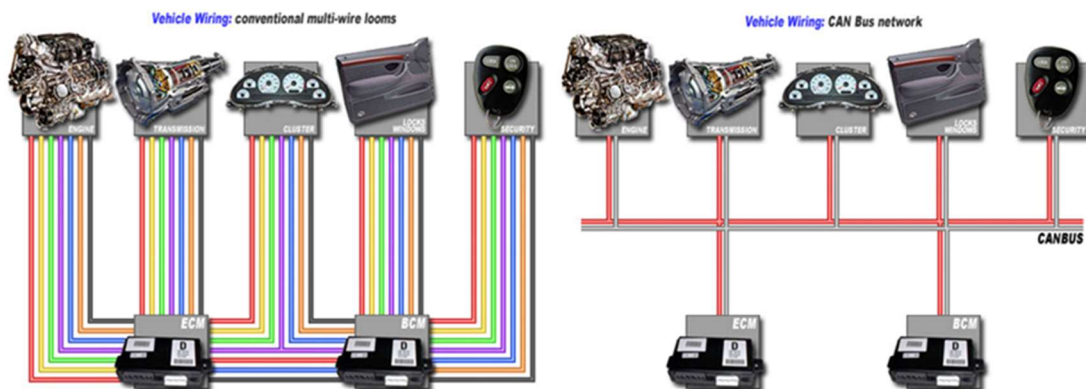


Figure 1.3 - Visual comparison between a multi-wire configuration and a CAN-BUS configuration

Fortunately, electronics provided a solution to this problem: in 1987 Intel, in collaboration with Bosch, made the first CAN network chip called (82256). CAN is an acronym for Control Area Network and defines a real on-board network protocol just as it happens in LAN networks for personal computers. In practice, a single twisted pair which acts as a BUS connects all the vehicle's on-board control units to each other, so they can communicate with each other by exchanging various types of information. CAN bus is designed to carry data at high speed up to 1 Mbit/s in some implementation [27]

1.1. Structure of an Electronic Control Unit

Going into detail, there are dozens of control units on board a vehicle, and each control unit is composed of various modules (ECM). Types of ECM include Engine Control Module (EECM), Powertrain Control Module (PCM), Transmission Control Module (TCM), Brake Control Module (BCM or EBCM), Central Control Module (CCM), Central Timing Module (CTM), General Electronic Module (GEM), Body Control Module (BCM), Suspension Control Module (SCM).

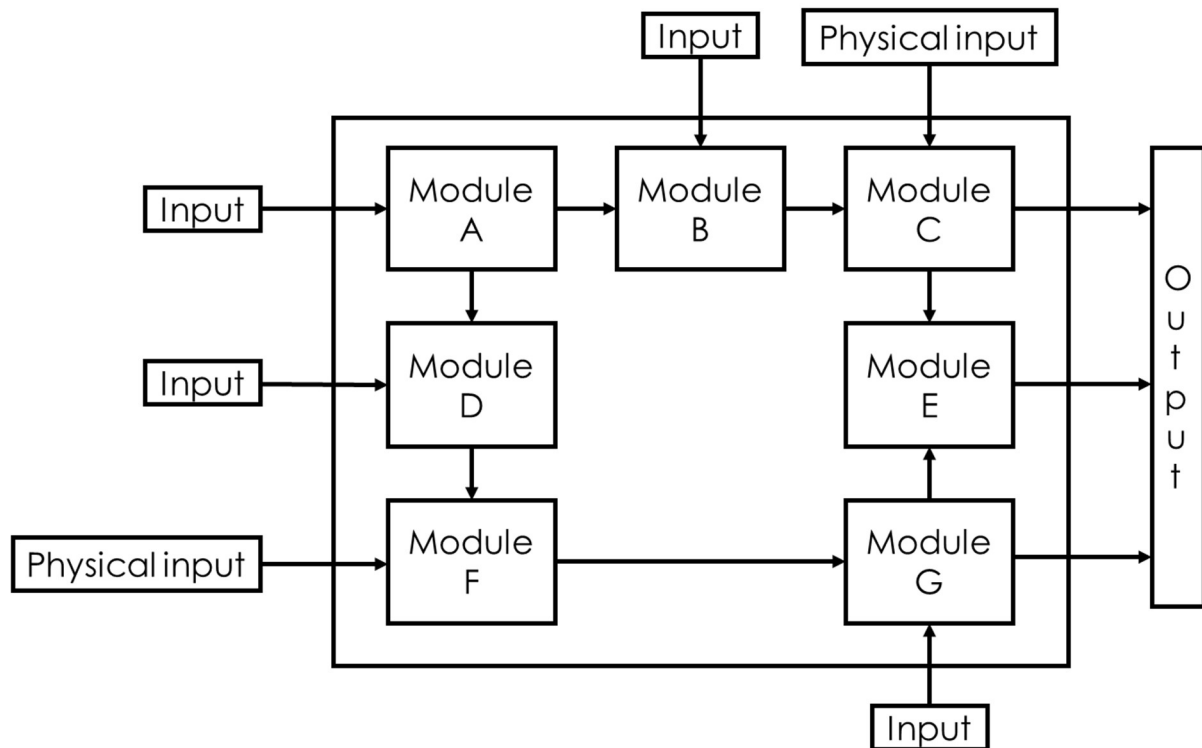


Figure 1.4 – schematization of the structure of an ECU

In Figure 1.4, a schematization of the structure of a control unit is shown. The various modules of which it is composed communicate with each other by receiving electrical input signals. These signals, which can derive from other control units or from on board sensors, are processed by the individual functions of which the modules are composed and returned as output. The processed signals can be sent to other control units or to actuators. The purpose of the Modules is to receive electrical input signals that determine the operating conditions of the engine or the vehicle, process these signals, and supply them as output to the actuators in order to respond to the Driver's requests. Each ECM is composed of a series of functions, each used for a specific calculation. In the Engine Control Module, each function has the task of estimating a specific physical quantity: for example, the air flow, the required and delivered torque, the position of the throttle valve, and so on.

As schematized in *Figure 1.5*, each function can be composed of maps, vectors and / or scalars. In the schematization, the module is composed of three functions. Function 1 is in turn composed of a vector and a map; function 2 consists of a vector and a scalar and function 3 processes the signal of function 1 and function 2 with a table.

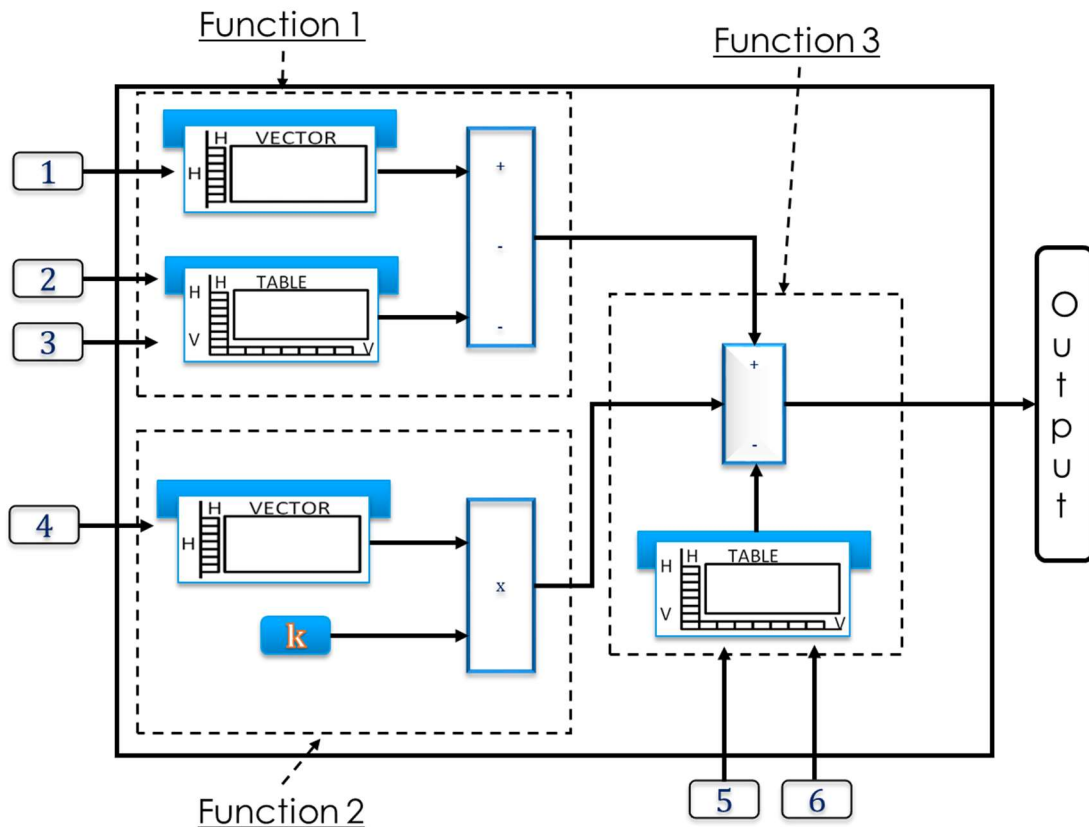


Figure 1.5 – schematization of the structure of an ECM

The use of maps, vectors and scalars is of fundamental importance to simplify the functions and speed up the calculations: an ECU, in fact, must calculate hundreds or thousands of functions and return output in real-time. Add to this the fact that the ECUs normally used in the automotive field have very limited computing power: just think that the computing power of the ECU is about 2 GFLOPS, while an Intel Core i7-8086K processor can reach 120 GFLOPS. To overcome the limited computing power and the high number of functions to be processed in real-time, the functions "written" in the control unit are simplified equations. Simplification is so deep that it minimizes the physics present in the equation. Consequently, the equations are able to recreate the physical phenomena in all the engine operating conditions using parameters (i.e. Maps, vectors and scalars). The parameters must be appropriately calibrated to ensure that the values of the physical quantity

calculated by the control unit function are as close as possible to the experimental ones in the same operating conditions.

Below is an example of a function used to estimate the volumetric efficiency.

$$VOL_{EFF} = \frac{M_{AIR}}{M_{REF}} \quad (1.1)$$

Where:

$$M_{AIR} = \frac{(p_{amb} \cdot V_c \cdot a - V_{cc} \cdot p_{eg} \cdot b)}{R \cdot T_{amb}} \cdot c \quad (1.2)$$

The estimation of the volumetric efficiency is given by the ratio between the estimate of the air mass trapped in the cylinders and the one at the reference conditions (1.1). In turn, the estimated air mass is described in equation (1.2) where: p_{amb} e T_{amb} are respectively the pressure and the environment temperature estimated by the probes present on the vehicle, R is the universal constant of the gases, V_c is the cylinder volume, V_{cc} is the combustion chamber volume, p_{eg} is the exhaust gas pressure, a , b and c are three corrective maps.

As can be seen the equation (1.2) is a derivative of the Ideal gas law (1.3):

$$p \cdot V = m \cdot R \cdot T \quad (1.3)$$

That is, we are trying to model a three-dimensional physical phenomenon that depends on many variables with a simple stationary equation. It is impossible for function (1.1) to assess volumetric efficiency in all operating conditions of the engine with an acceptable error. Precisely for this reason, the function is equipped with three corrective maps which, if properly calibrated, manage to ensure that the volumetric efficiency obtained from the function is very close to the experimental one throughout the operating range of the engine.

1.2. Structure of an ECU function: Maps, vectors, scalars

Equation (1.2) can be represented according to the schematization seen in *Figure 1.5* and shown in *Figure 1.6*. The figure shows the inputs that are sent by on board probes or by other control unit functions. In particular, it can be noted that the map a is a two-dimensional map which depends on the rpm and closing angle of the intake valves (VVA), the map b also depends on the rpm and closing angle of the intake valves and the map c which depends on the pressure in the manifold and closing angle of the throttle valve (A_{cls}). Maps, as well as scalars and vectors, are simply a set of numbers.

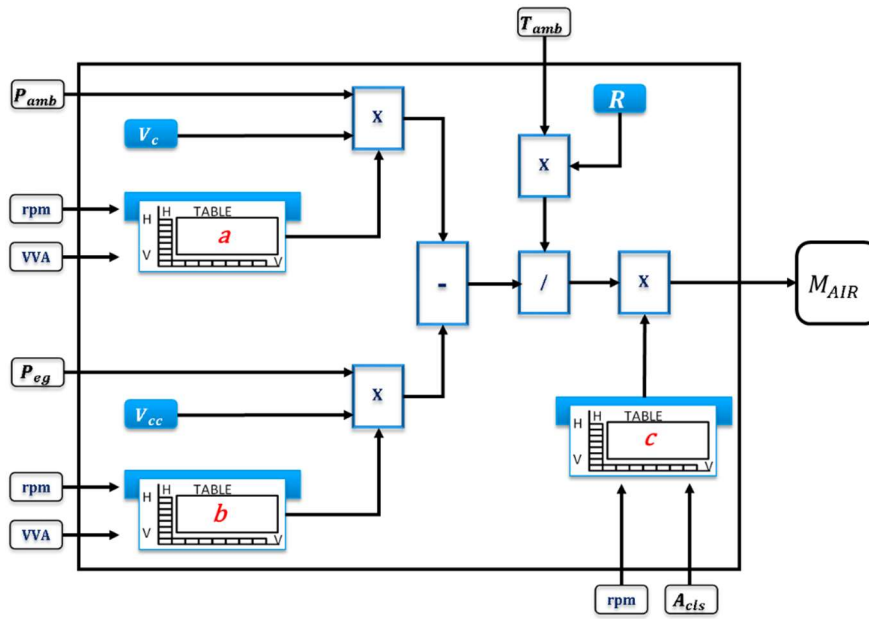


Figure 1.6 – schematization of the function (2)

The maps are a set of numbers that depend on two or more parameters: for example, the map *c* is a set of values that depends on the engine speed and the closing angle of the throttle valve. This map is shown in the *Figure 1.7*. In practice, the map receives the manifold pressure and throttle angle signals as input and returns the output value.

Vacl [°]														
RPM		800	900	1000	1100	1200	1300	1400	1500	1600	1700	1800	1900	2000
0	0.377	0.379	0.378	0.373	0.347	0.331	0.318	0.309	0.298	0.290	0.274	0.268	0.255	
2.5	0.442	0.438	0.430	0.424	0.401	0.385	0.366	0.365	0.352	0.343	0.326	0.322	0.311	
5	0.503	0.499	0.499	0.494	0.476	0.464	0.436	0.428	0.406	0.388	0.366	0.361	0.350	
7.5	0.572	0.572	0.572	0.577	0.557	0.546	0.519	0.509	0.482	0.435	0.397	0.384	0.371	
10	0.648	0.646	0.642	0.651	0.629	0.622	0.607	0.600	0.583	0.515	0.445	0.418	0.401	
12.5	0.721	0.724	0.727	0.730	0.709	0.694	0.688	0.680	0.658	0.606	0.530	0.480	0.433	
15	0.780	0.793	0.797	0.798	0.785	0.778	0.766	0.749	0.725	0.694	0.634	0.572	0.502	
17.5	0.836	0.849	0.848	0.853	0.847	0.833	0.828	0.801	0.783	0.769	0.725	0.669	0.602	
20	0.882	0.893	0.905	0.908	0.901	0.887	0.878	0.866	0.845	0.835	0.806	0.756	0.696	
22.5	0.926	0.942	0.959	0.957	0.953	0.947	0.940	0.924	0.923	0.903	0.884	0.838	0.795	
25	0.969	0.981	0.997	0.995	0.991	0.988	0.979	0.979	0.975	0.960	0.948	0.925	0.882	
27.5	1.004	1.012	1.022	1.024	1.026	1.020	1.016	1.019	1.022	1.019	0.999	0.988	0.952	
30	1.032	1.037	1.037	1.037	1.039	1.038	1.045	1.043	1.054	1.054	1.040	1.032	1.003	
32.5	1.038	1.041	1.041	1.041	1.043	1.041	1.054	1.055	1.067	1.065	1.055	1.047	1.024	
35	1.036	1.040	1.039	1.038	1.043	1.044	1.058	1.060	1.073	1.069	1.066	1.061	1.042	
37.5	1.028	1.038	1.037	1.037	1.040	1.041	1.058	1.063	1.074	1.075	1.075	1.072	1.057	
40	1.018	1.033	1.032	1.033	1.035	1.037	1.054	1.058	1.071	1.079	1.082	1.081	1.070	
42.5	1.010	1.025	1.025	1.028	1.032	1.033	1.048	1.053	1.067	1.077	1.085	1.085	1.078	
45	0.999	1.017	1.021	1.023	1.026	1.025	1.041	1.049	1.062	1.075	1.084	1.085	1.083	
47.5	0.989	1.007	1.004	1.009	1.013	1.017	1.032	1.036	1.055	1.071	1.080	1.080	1.081	
50	0.979	0.993	0.990	0.999	1.002	1.008	1.016	1.024	1.044	1.055	1.064	1.069	1.074	
52.5	0.966	0.980	0.977	0.984	0.988	0.996	1.000	1.011	1.031	1.045	1.056	1.057	1.060	
55	0.952	0.963	0.963	0.970	0.974	0.982	0.986	0.990	1.013	1.030	1.034	1.040	1.047	
57.5	0.922	0.927	0.932	0.933	0.937	0.939	0.946	0.952	0.968	0.977	0.989	0.993	1.004	
60	0.847	0.862	0.871	0.875	0.881	0.885	0.893	0.903	0.920	0.928	0.946	0.954	0.961	
62.5	0.784	0.797	0.806	0.811	0.825	0.834	0.846	0.855	0.869	0.876	0.892	0.906	0.914	

Figure 1.7 – structure of map *c* after the calibration

For example, at 1000 mbar and 70 ° of angle of the throttle valve the map returns a value of 1.084 which will be multiplied by the value returned by the remaining part of the function to obtain the mass of air trapped in the cylinder.

In a similar way, vectors are presented as a set of numbers, but this time they depend on a single variable. The scalars, on the other hand, are unique values for the whole operating range of the engine. The values of the map *c* shown in *Figure 1.7* must be chosen appropriately, i.e. the map must be calibrated using advanced calibration software described in chapter 2. In fact, all maps values, as well as all vectors and scalars, are random during the design phase. In most cases the values are equal to 1, as shown in *Figure 1.8*.

	Vacl [°]													
RPM		800	900	1000	1100	1200	1300	1400	1500	1600	1700	1800	1900	2000
	0	1	1	1	1	1	1	1	1	1	1	1	1	1
	2.5	1	1	1	1	1	1	1	1	1	1	1	1	1
	5	1	1	1	1	1	1	1	1	1	1	1	1	1
	7.5	1	1	1	1	1	1	1	1	1	1	1	1	1
	10	1	1	1	1	1	1	1	1	1	1	1	1	1
	12.5	1	1	1	1	1	1	1	1	1	1	1	1	1
	15	1	1	1	1	1	1	1	1	1	1	1	1	1
	17.5	1	1	1	1	1	1	1	1	1	1	1	1	1
	20	1	1	1	1	1	1	1	1	1	1	1	1	1
	22.5	1	1	1	1	1	1	1	1	1	1	1	1	1
	25	1	1	1	1	1	1	1	1	1	1	1	1	1
	27.5	1	1	1	1	1	1	1	1	1	1	1	1	1
	30	1	1	1	1	1	1	1	1	1	1	1	1	1
	32.5	1	1	1	1	1	1	1	1	1	1	1	1	1
	35	1	1	1	1	1	1	1	1	1	1	1	1	1
	37.5	1	1	1	1	1	1	1	1	1	1	1	1	1
	40	1	1	1	1	1	1	1	1	1	1	1	1	1
	42.5	1	1	1	1	1	1	1	1	1	1	1	1	1
	45	1	1	1	1	1	1	1	1	1	1	1	1	1
	47.5	1	1	1	1	1	1	1	1	1	1	1	1	1
	50	1	1	1	1	1	1	1	1	1	1	1	1	1
	52.5	1	1	1	1	1	1	1	1	1	1	1	1	1
	55	1	1	1	1	1	1	1	1	1	1	1	1	1
	57.5	1	1	1	1	1	1	1	1	1	1	1	1	1
	60	1	1	1	1	1	1	1	1	1	1	1	1	1
	62.5	1	1	1	1	1	1	1	1	1	1	1	1	1

Figure 1.8 – map *c* before the calibration

It is clear that a function, and therefore a control unit, that uses uncalibrated functions will never return the correct value of the calculated quantity, in almost all the operating range of the engine.

1.3. Engine Control Module operation

As schematized in *Figure 1.9*, an ECM is structured in two parallel networks: the first network consists of the objective algorithms. The task of these functions is to evaluate the quantities required by the driver. The other network consists of estimation algorithms: these algorithms must estimate the current experimental quantities in real time. The objective algorithms receive signals from the driver in real-time and process these signals to evaluate the target quantities to be achieved: for

example, based on the position of the acceleration pedal, the torque function evaluates the torque required by the driver.

At the same time, always in real time, in the other network the estimation algorithms evaluate the current experimental quantities: for example, based on the rpm, the volumetric efficiency, the fuel flow rate, the function evaluates the torque in that instant delivered by the engine.

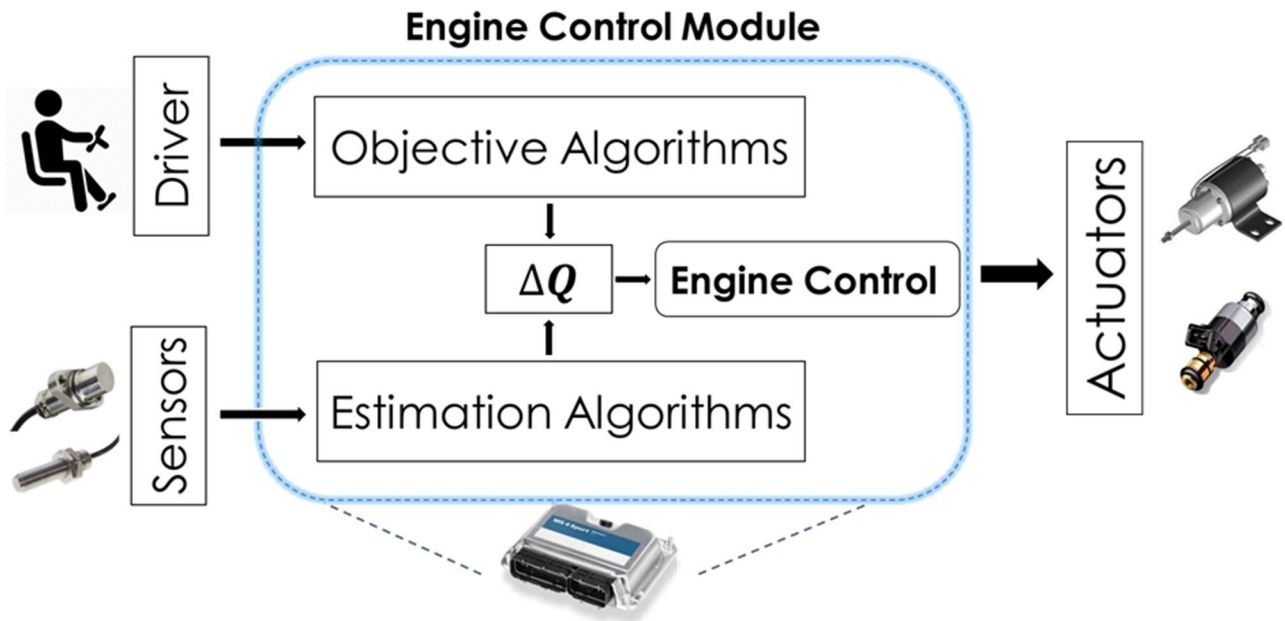


Figure 1.9 – schematization of the ECM functioning

If the two quantities, the one evaluated by the objective algorithms and the one evaluated by the estimation algorithms, differ from each other, the controller acts on the actuators in order to reduce this difference. For a correct functioning of the ECM and consequently of the engine and of the vehicle in general, the functions, both the objective and the estimation ones, must be able to evaluate the physical quantities over the whole operating range of the engine. These calibration parameters are evaluated, through advanced software, by a comparison between the quantities obtained from the functions and those obtained from experimental engine tests. It is clear that the experimental tests are carried out on a wide engine operating range to make the function precise in each working condition.

1.4. Base engine calibration process

The engine base calibration process is one of the longest industrial processes in the design on a new vehicle. As shown in *Figure 1.10* during the design phase, the functions are developed according to the choice of the hardware to be used on the vehicle. Contemporarily to the development of the control strategy, the base calibration takes place. In this phase, thousands of operating conditions are

analyzed on a test bench and hundreds of experimental quantities are acquired. As will be seen later, and in more detail in chapter 2, the experimental campaigns are very extensive both in terms of costs and in terms of implementation times. The reason for using extensive experimental campaigns consists in the fact that the experimental quantities are compared with those obtained from the ECUs. It is clear that the more extensive is the comparison, the more correct the functioning of the ECU, and therefore of the engine and vehicle, will be.

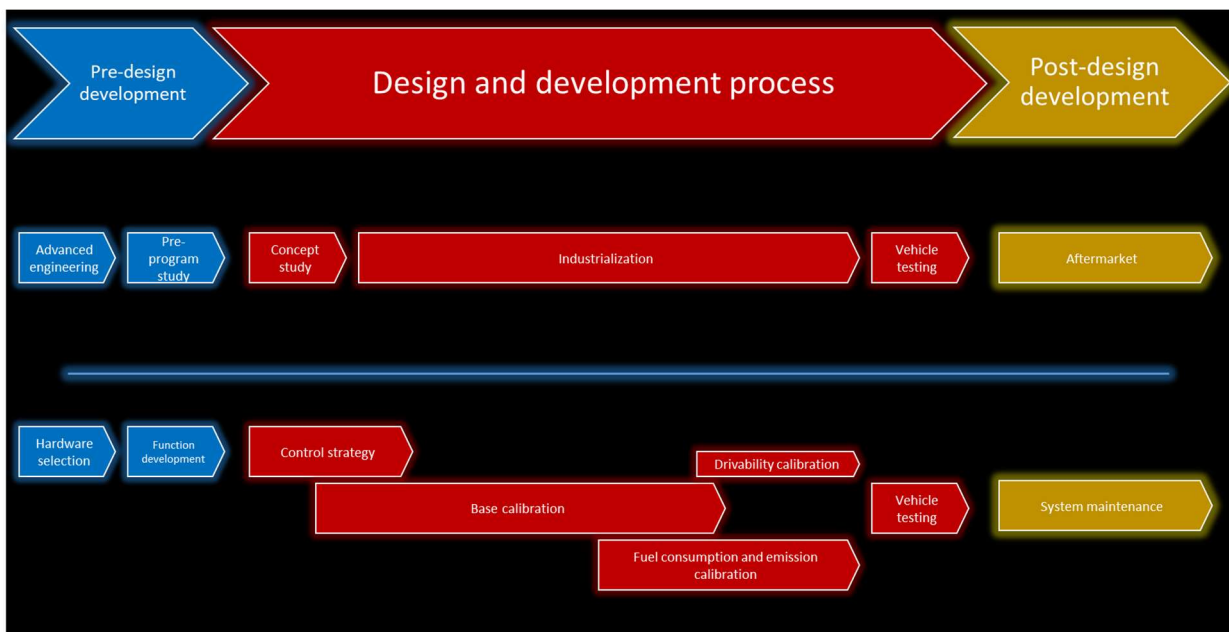


Figure 1.10 – timeline of the design and development of a new vehicle

The entire base calibration process can be schematized as a series of steps as shown in Figure 1.11. The first step is the design and execution of the experimental campaign: the engine is placed on a test bench and is connected to a large number of sensors. The points to be analyzed are chosen by choosing a series of parameters such as the rpm, the position of the throttle valve, the use of the wastegate to limit the power of the turbine, the use of the variable timing, etc... As previously written, the experimental data are measured over the entire operating range of the engine by performing a sweep of predetermined elements for a fixed engine rpm. An example of an experimental campaign is the following, called Full Lift Campaign, divided into 2 phases:

- The engine speed is fixed and the following values are analyzed: 1000, 1200, 1500, 1800, 2100, 2400, 2700, 3000, 3300, 3600, 4000, 4300, 4600, 4900, 5200, 5500, 5800, 6200.
- The opening and closing angle of the intake valves is fixed, i.e. the VVA is deactivated.

Phase 1:

- The wastegate valve is completely open.
 - For each engine speed, a throttle valve opening angle sweep is made from the minimum possible opening for correct engine operation at that rpm, up to the maximum opening of the valve, with a manifold pressure step of 50 mbar. For example, at 3000 rpm, starting from 400 mbar of pressure in the manifold, 13 different openings of the throttle valve are identified, determining 13 different operating conditions:
 - 3000 rpm, manifold pressure 400 mbar,
 - 3000 rpm, manifold pressure 450 mbar,
 - 3000 rpm, manifold pressure 500 mbar,
 - ...
 - 3000 rpm, manifold pressure 1000 mbar,
 - The spark advance is varied in all operating conditions to reach the maximum torque or incipient detonation.
- Phase 2:
- Once the maximum opening of the throttle valve is reached, for each engine speed an additional manifold pressure sweep is carried out: the opening of the wastegate is adjusted to increase the manifold pressure in steps of 50 mbar. For example:
 - 3000 rpm, manifold pressure 1050 mbar,
 - 3000 rpm, manifold pressure 1100 mbar,
 - 3000 rpm, manifold pressure 1150 mbar,
 - ...
 - 3000 rpm, manifold pressure 2400 mbar,
 - The spark advance is varied in all operating conditions to reach the maximum torque or incipient detonation.

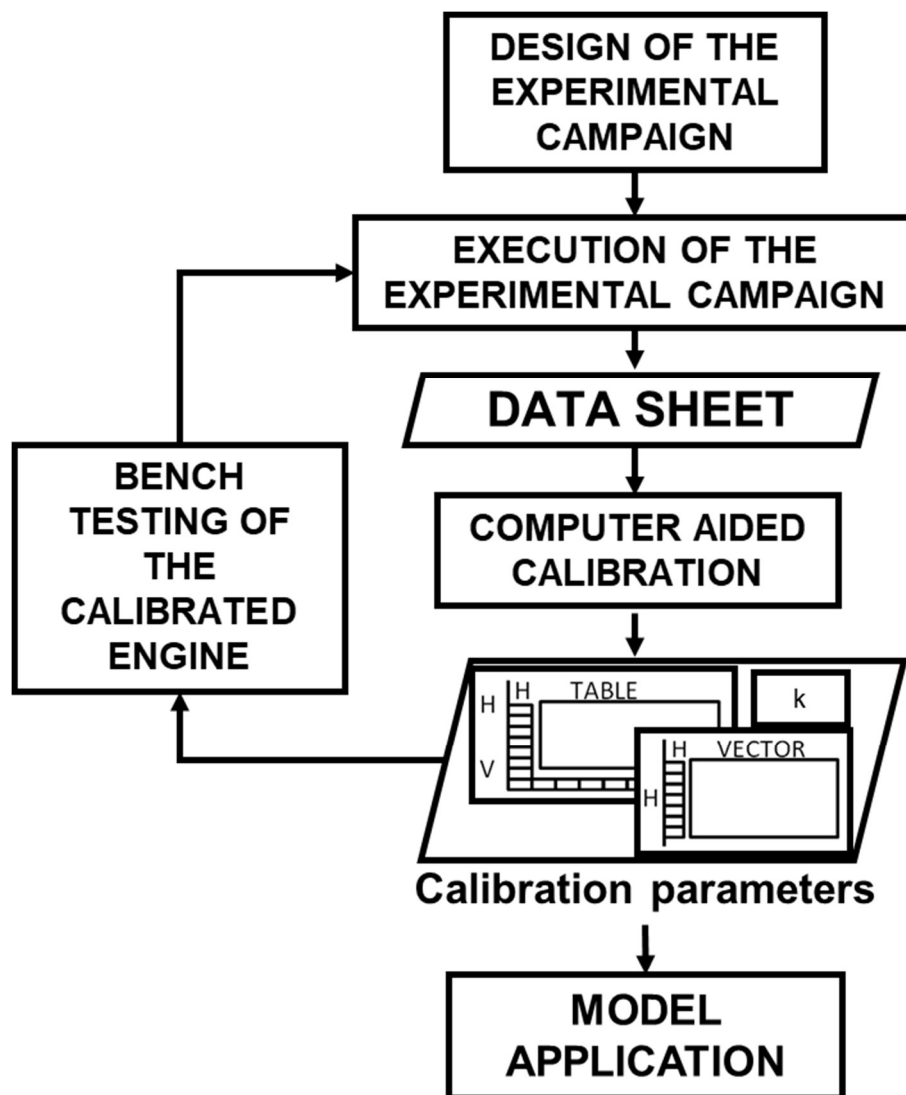


Figure 1.11 – schematization of the traditional engine base calibration process

In the third step, all the experimental data acquired on the test bench during step 2 are collected in different datasheets such as the one shown in *Figure 1.12*, where each row represents an operating condition and each column represents an experimental quantity measured on a test bench. This is only a partial datasheet, as a single datasheet can contain hundreds to thousands of rows (and therefore operating conditions) and hundreds of columns (quantities acquired on the test bench).

These datasheets are used as input in the Computer Aided Calibration to derive the calibration parameters. These two phases are described in more detail in chapter 2. Subsequently, the calibrated ECUs are tested both on the engine and directly on the vehicle.

Various experimental campaigns are carried out to calibrate the control unit functions. Each campaign follows certain strategies that span the entire operating range of the engine, also exploring the ones that will hardly be used in its actual operation. Considering the fact that each experimental

campaign can contain thousands of operating conditions and that in every operating condition the engine runs for about 5 minutes, it is understood that the entire base calibration process is very long and expensive. The object of this Thesis is to try to reduce the execution costs by reducing the experimental tests, without, however, reducing the calibration performance and affecting the operation of the engine and vehicle.

1	RPM	ThrottAng	SparkAdv	h_consum	BSFC	Torque	VolEff	Lambda	P_CV	P_KW	Pmax	Pmax1	Pmax2	PME	PM
2	-	deg	deg	kg/h	g/kW.h	Nm	-	-	CV	kW	bar	bar	bar	bar	bar
3	6200	81.94	18.7	20.189	347.75	89.42	1.2601	0.825	78.956	58.1	85.606	88.8	82.412	12.8459	
4	6200	81.92	16.1	18.536	303.37	94.11	1.3001	0.917	83.098	61.1	80.099	82.06	78.135	13.5197	
5	6200	81.92	16.6	18.811	308.19	94.02	1.2976	0.907	83.014	61	82.323	85.09	79.56	13.5061	
6	6200	81.92	10.1	26.41	374.3	108.65	1.6538	0.822	95.958	70.6	79.695	82.33	77.061	15.612	
7	6200	81.91	8.5	30.98	407.44	117.1	1.9053	0.809	103.411	76	81.133	82.19	80.078	16.8246	
8	6200	80.63	12.7	22.291	335.76	102.29	1.4718	0.862	90.305	66.4	77.697	78.93	76.462	14.6922	
9	6200	38.63	19.4	19.195	343.85	85.98	1.212	0.833	75.92	55.8	82.985	84.6	81.367	12.3522	
10	6200	31.36	19.4	18.586	342.69	83.54	1.1811	0.842	73.76	54.2	80.14	81.74	78.54	12.0004	
11	6200	27.08	20.2	17.794	338.42	80.99	1.1397	0.854	71.509	52.6	78.316	81.11	75.52	11.6342	
12	6200	24.26	19.7	17.009	336.21	77.93	1.105	0.852	68.802	50.6	74.367	76.02	72.716	11.1937	
13	6200	23.27	20.3	16.498	331.66	76.61	1.0831	0.862	67.653	49.7	74.936	76.43	73.441	11.0069	
14	6200	17.35	22.3	12.357	311.83	61.07	0.8805	0.938	53.891	39.6	59.608	60.29	58.925	8.7674	
15	6200	14.5	25.5	9.39	319.42	45.28	0.7052	0.989	39.98	29.4	48.454	48.31	48.595	6.5045	
16	6200	12.18	28	7.261	358.1	31.24	0.5497	0.997	27.575	20.3	37.655	36.83	38.478	4.4863	
17	6200	10.29	31.3	5.617	441.4	19.62	0.4254	1.001	17.308	12.7	29.93	29.51	30.354	2.8159	
18	6200	8.3	34.9	4.103	756.7	8.37	0.3095	0.997	7.379	5.4	21.154	20.9	21.407	1.2005	
19	6200	6.07	43.5	2.792	-1379.53	-3.14	0.2113	0.995	-2.768	-2	13.208	13.05	13.367	-0.4503	
20	5900	81.94	11.8	20.346	317.06	103.81	1.4503	0.885	87.272	64.2	81.233	80.62	81.85	14.9132	
21	5900	81.94	7.2	26.836	366.25	118.53	1.8008	0.839	99.649	73.3	82.75	82.47	83.033	17.0281	

Figure 1.12 – structure of a datasheet

2. Computer aided calibration: main stages and calibration performances

Figure 2.1 shows a detailed scheme of the “Computer aided calibration” stage represented in Figure 1.11 adopted in the current work to optimize the EECU calibration parameters. In particular, the process includes the following stages: the bench data set obtained from the experimental campaign is used as input to the algorithm. Through the Engine Verification Software (EVS), the performance of uncalibrated algorithms are analyzed and only the values necessary in that specific calibration are selected. In this stage, default values are assigned to the functions’ calibration parameters and so the output values from the functions can be affected by high errors. Subsequently, after the launch of the Automated Calibration Software (ACS), the specific calibration algorithm is launched. For example, discrete regression or multi-map optimization algorithm can be selected. At the end of this stage, the ACS generates the calibrated parameters. These values can be object of further manual refinement by changing specific parameters values in order to minimize the algorithm estimation error. After the values of the calibration parameter have been obtained, the performance of the calibration process is checked again through the EVS. The calibration performance is evaluated by mean of the percentage error between the values provided by the control unit function and the related experimental values. It is calculated as follows:

$$err_{\%} = \frac{Q_{EXP} - Q_{EST}}{Q_{EXP}} \cdot 100 \quad (2.1)$$

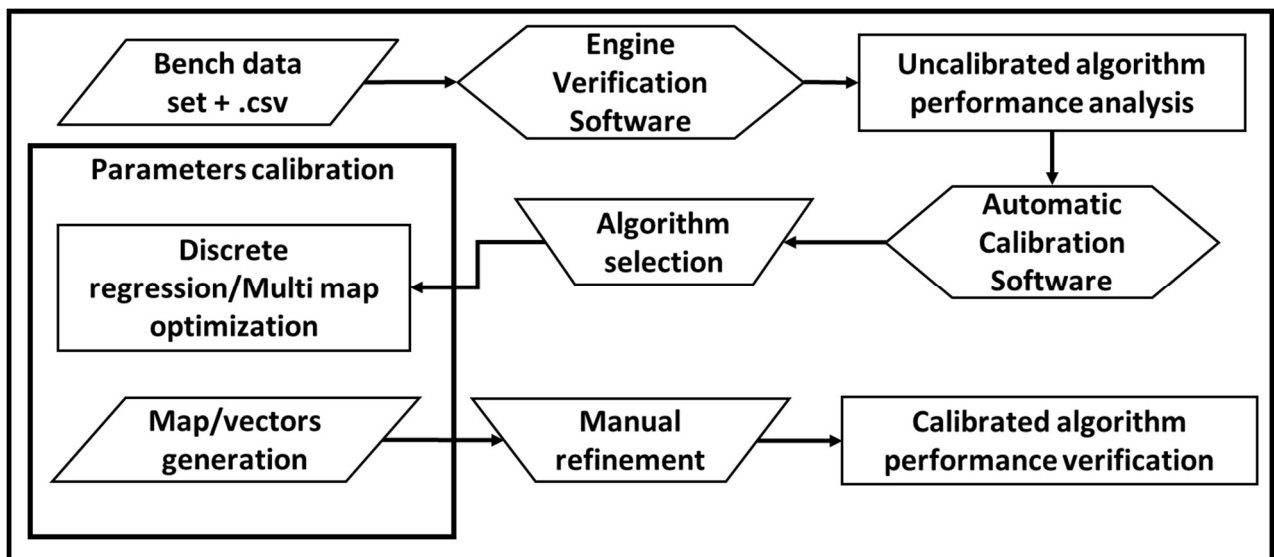


Figure 2.1 – main steps of the computer aided calibration software

If the calibration results do not fall within the acceptable limits, after the performance verification stage, a manual refinement is repeated. It also highlights how modifications to the parameters of the control unit functions affect the calibration results.

At the end of the calibration process, the optimized parameters values included within the functions of the actual engine control unit and the ECU are tested in their real operation. Although the proposed approach is quite complex, the computational speed is very high and the results are much more accurate than those obtained with traditional methods, such as manual calibration. As shown in *Figure 2.1* the software is based on a discrete regression technique, suggested by Riegel et al., that is briefly described in this section, whereas further details are provided in [28]. The algorithm is used to calibrate lookup tables starting from the discrete values of three channels. Two of these data channels are considered to be independent variables (X and Y), while the third is the dependent variable and the output of the map. The values of the lookup tables are optimized to minimize the difference between their output and values of the reference test bench quantity. In particular, the regression algorithm will provide the output Z values that minimize the root mean square of the distance between the points of a surface that are obtained through a bi-linear interpolation of the map values and the related experimental points. To achieve this result, the proposed algorithm exploits the analogy with the mass-spring-damper mechanical system shown in *Figure 2.2*. Each experimental point for the output quantity (the red circles in *Figure 2.2*) is fixed in space, while the blue lines, which represent the regression map object of optimization, can move along the z axis. The red points are bound with springs, the stiffness of which is the same for each point, to the map. A dynamic damper, characterized by a critical damping ratio, is supposed to be placed in parallel to each spring.

The blue segments of the map have mass and react to the forces exerted by the springs and dampers in accordance with the second principle of dynamics. These forces tend to reduce the distance of the map from the fixed points. The balance is achieved by configuring the map to minimize the potential energy of the spring system, which can be expressed as follows:

$$E = \sum_{i=0}^N K \cdot \Delta z_i^2 \quad (2.2)$$

where K is the stiffness of the springs, Δz_i^2 is the distance along the z-axis between the i-th fixed point and regression map and N is the number of experimental points.

Equation (2.2) represents the sum of the squared errors (SSE) between the experimental data and regression map. If the quantity E in equation (2.2) is divided by $K \cdot N$, both of which are constants, it returns the mean square error (MSE). Therefore, the solution of the calibration problem is the same as the physical problem. A smoothing process of the engine maps is also needed to ensure drivability

to the target vehicle. The difficulty of this step is in staying as close as possible to the experimental points while keeping a smooth map shape, as stated in [29] [30].

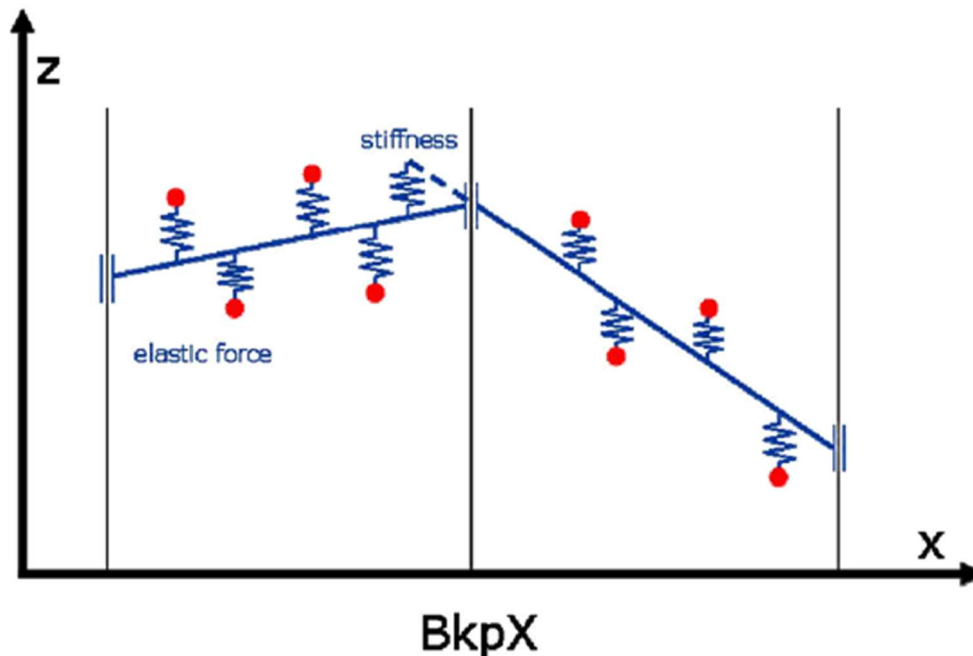


Figure 2.2 - Mass-spring-damper analogy adopted for the discrete regression technique within the proposed calibration tool

For this reason, to reduce the angularity between two adjacent segments, the adopted regression technique also involves the use of springs between the segments of the physical model depicted in *Figure 2.2*, whose rigidity could be defined by the user. In this way, the user may increase the smoothness of the map by changing the supplementary spring rigidity. Indeed, it is possible to impose a desired stretch ratio of the surface so that, at the expense of an increase in the root mean square error, it can be smoothed out to make the map a more suitable representation of a physical phenomenon without blindly following acquisitions that may be affected by errors. This novel algorithm has the potential to reduce over fitting because of the dynamic interaction during its running, which facilitates control of the smoothness and root mean square error for regression curves and surfaces. When a calibration function makes use of more than one calibration parameter, a multi-map optimizer is adopted within the proposed algorithm. That optimizer can simultaneously calibrate all parameters and make use of a technique from the steepest descent algorithm [31] [32] [33].

2.1. Application of the Regression Technique to the Calibration of the Volumetric Efficiency Function

In this section there is a demonstration of the application of the proposed regression technique to the volumetric efficiency function seen in the equations (1.1) and (1.2). Specifically, the results refer to a two-cylinder turbocharged engine equipped by a fully flexible electro-hydraulic valve actuation system for the intake valves (*Table 2.1*).

Table 2.1 – characteristics of the engine equipped with the volumetric efficiency function

Model	Turbocharged, 2 cylinders, 8 valves, VVA
Displacement	875 cm ³
Stroke/Bore	86 mm / 80.5 mm
Connecting Rod Length	136.85 mm
Compression Ratio	9.9

As mentioned, in this function there are 3 corrective maps to be calibrated: a , b and c , which depend on rpm, closing angle of the intake valves (VVA), manifold pressure and closing angle of the throttle valve (A_{cls}). The experimental campaign used to calibrate the volumetric efficiency function includes data concerning 680 engine operating conditions. The volumetric efficiency is a fundamental engine quantity which is not directly measurable from the sensors available on marketed vehicles. It is used to evaluate the engine torque, to set the spark advance and the throttle position. These maps include default values at the beginning of the calibration process. If these values are set to 1 and a performance evaluation of the uncalibrated function is carried out, as described in *Figure 2.1*, an analysis of the uncalibrated functions can be made. The results of the analysis of the uncalibrated volumetric efficiency function are shown in *Figure 2.3*.

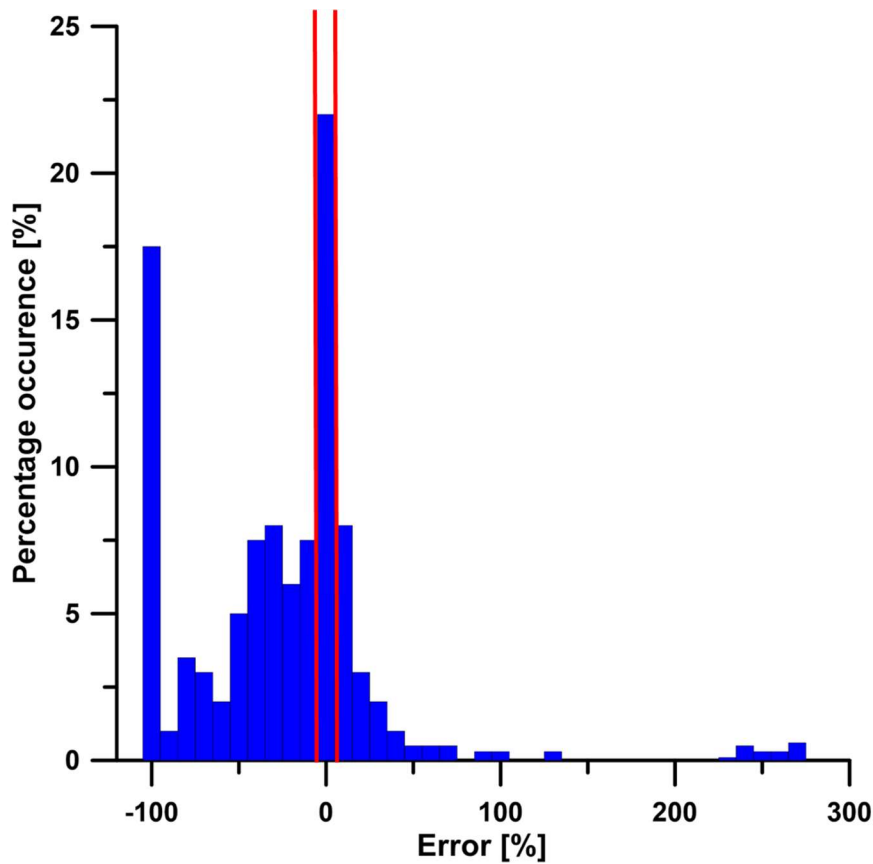


Figure 2.3 – error distribution for the uncalibrated function

The calibration performance of the control unit function is evaluated through the percentage of error values, calculated as differences between the quantity evaluated by the function and the experimental quantity in the same operating conditions (function (2.1)), which falls within an acceptable range, established a priori. *Figure 2.3* shows the performance of the function (1.1) and (1.2) using default maps' values. As can be seen, the performance of the function is very poor: because of default values adopted to fill in the lookup tables, only 22% of the values estimated by the function are within the acceptable limit. In particular, a limit of 5%, identified by the red lines in *Figure 2.3*, has been imposed by the engine manufacturer for this function. It is evident how the three maps need a proper calibration, thus allowing the volumetric efficiency to be as close as possible to the values measured at test bench. If functions with such a low calibration performance were modelled on an ECU connected to an engine, the engine could have serious functioning problems which could also lead to breakage. For this reason, the calibration performance must be as high as possible in a wide range of engine operation.

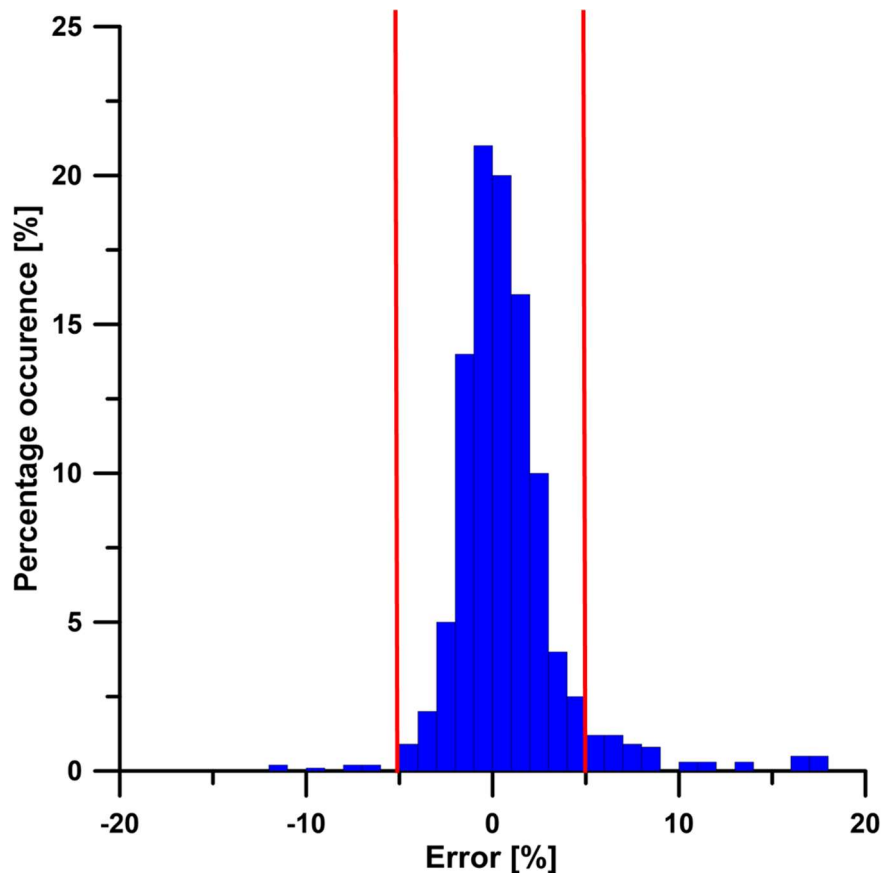


Figure 2.4 – error distribution for the calibrated function

Figure 2.4 shows the results obtained after the calibration process obtained by mean of the proposed computer aided calibration methodology. The figure highlights how the 94.5% of the percentage errors fall now within the acceptable range. Moreover, a further manual refinement process, allowed by the software tool, could even increase the calibration performance. The acceptability range depends on the function, but are generally between ± 5 and $\pm 10\%$. Calibration performance is high when 90-95% of function errors fall within the acceptability range.

2.2. Application of the Regression Technique to the Target Throttle Angle Function

In the previous chapter it was said that the control unit functions are such simplified equations as to lose the physics of the phenomenon they try to describe, causing poor functioning of the ECUs and consequently of the vehicle: hence the adoption of maps, vectors and scalars. Despite this, the equations are still simplified, resulting in a non-optimal functioning of the ECU. This paragraph shows that an increase in the physics of the equations leads to an improvement in the performance of the equation itself, increasing the number of errors that fall within the acceptable range.

An implementation of a Computer Aided Calibration software has been developed to overcome a critical issue of the traditional calibration process: improve the calibration accuracy. The algorithm includes some innovative features aimed at error minimization through a complete parametric analysis of a target ECU functions. Therefore, it is possible to assess if further quantities that are not considered as calibration parameters within the current ECU function model actually affect the quantity estimated by the function itself. If so, a more accurate physical model can be implemented within the ECU function to increase the accuracy of the calibration process. The reference engine has the same characteristics reported in *Table 2.1*. The developed calibration algorithm has been used as an analysis tool to investigate the prediction capability of the function adopted to estimate the target throttle angle. This approach was useful to highlight the limits of the model adopted for estimating the throttle angle. The limits were mainly due to an over-simplification of the implemented physical model. Therefore, the ECU function was properly modified according to the results of the analysis. As for the throttle control model adopted during the torque control, the ECU software assigns the selection of the throttle position to a specific map. The dependent variable of this map is the throttle angle, while the independent variables are the corrected target mass flow rate in the manifold and corrected pressure ratio across the throttle valve (*Figure 2.5*).

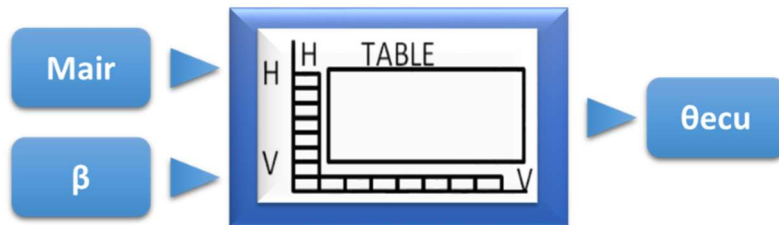


Figure 2.5. Schematic representation of the function providing the throttle angle as a function of the mass flow rate and pressure ratio.

Where M_{air} is the air mass flow rate and β is the pressure ratio downstream/upstream the throttle. Both are evaluated by the ECU.

The values in this map are based on the De Saint Venant equation, which describes mass flow through an orifice, whose scheme is represented in *Figure 2.6*, with consideration of the isentropic flow hypothesis while the following simplifying assumptions are accepted:

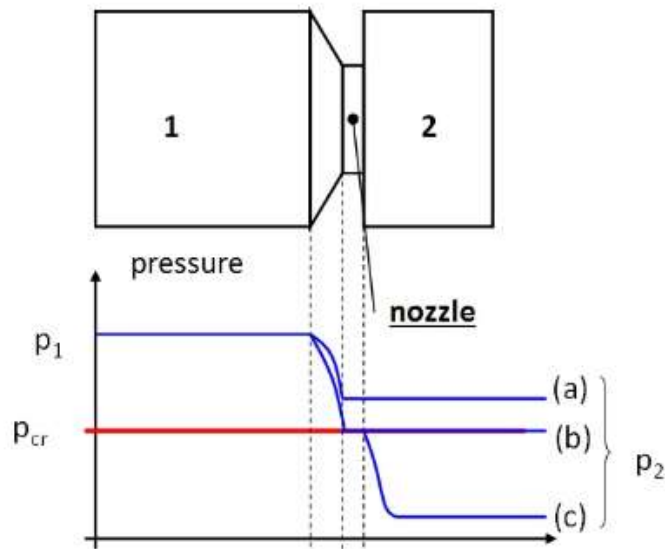


Figure 2.6. Mass flow through an orifice.

- 1) Negligible gas velocity at the inlet, making it possible to find the compression ratio at which the speed of sound is reached in the throat section:

$$\beta_{cr} = p_{cr}/p_1 = \left(\frac{2}{k+1}\right)^{\frac{k}{k-1}} \quad (2.3)$$

- 2) The gas is air ($k=1.40$), so the value of β_{cr} is known:

$$\beta_{cr} = 0.5283 \quad (2.4)$$

It is possible to identify three possible cases for the pressure p_2 downstream the orifice:

- $p_2 > p_{cr}$: subsonic flow; the pressure drops from p_1 to p_2 . The mass flow rate depends on the pressure ratio and throat section.
- $p_2 = p_{cr}$: sonic flow; the pressure drops from p_1 to p_{cr} . The mass flow rate depends on the throat section alone.
- $p_2 < p_{cr}$: sonic flow, the outlet pressure drops abruptly to p_2 , but the mass flow rate depends on the throat section alone (choked flow).

The system of equations that describes the flow and returns the mass flow rate is:

$$M_{air} = A_{tot} \cdot C_v \cdot \frac{A_{thr}}{A_{tot}} \cdot \sqrt{2 \cdot \frac{k}{k-1} \cdot \frac{p_{ups}^2}{R \cdot T_{man}} \left[\beta^{\frac{2}{k}} - \beta^{\frac{k+1}{k}} \right]} \quad (2.5)$$

$$\frac{A_{thr}}{A_{tot}} = 1 - \cos(\theta_{geo}) \quad (2.6)$$

$$\theta_{geo} = \theta_{ecu} + \theta_{cls} \quad (2.7)$$

where the mass flow rate is M_{air} in the first equation and is obtained from the values of the section of the pipe (A_{tot}), the effective section that is set by the throttle (A_{thr}), the discharge coefficient (C_v), the upstream pressure (p_{ups}), the air temperature in the manifold (T_{man}), the gas constant (R) and the pressure ratio (β), which becomes β_{cr} in case $p_2 \leq p_{cr}$. The section ratio in the second equation is related to the geometric throttle angle (θ_{geo}), while θ_{geo} in the third one is defined as the sum of the throttle angle measured by the ECU (θ_{ecu}) and the angle at the closed throttle (θ_{cls}).

In the reverse model, which allows for calculation of the throttle angle as a function of the flow rate and pressure ratio, this equation is written as follows, instead of (2.5):

$$A_{tot} \cdot C_v \cdot \frac{A_{thr}}{A_{tot}} = \frac{M_{air}}{\sqrt{2 \cdot \frac{k}{k-1} \cdot \frac{p_{ups}^2}{R \cdot T_{man}} \left[\beta^{\frac{2}{k}} - \beta^{\frac{k+1}{k}} \right]}} \quad (2.8)$$

The first step is to create an algorithm based on the direct model (equations (2.5),(2.6) and(2.7) so that through multi-map optimization, the De Saint Venant model can be calibrated. To this aim, it is possible to define:

$$A_{DSV} = C_v \cdot A_{tot} \quad (2.9)$$

$$A_{rel} = \frac{A_{thr}}{A_{tot}} = f(\theta_{ecu}, \theta_{cls}) \quad (2.10)$$

The experimental data input into this algorithm (i.e., the direct DSV model function) are θ_{ecu} , β , p_{ups} , and T_{man} , while the output is M_{air} . To complete the calculation, two scalar calibration parameters are needed, A_{DSV} and θ_{cls} . *Figure 2.7* shows the optimization scheme adopted for the De Saint Venant model, where M_{exp} is the measured air mass flow rate. The experimental data are represented in green boxes, while the scalar parameters to be optimized are represented in red.

During the optimization, the percentage root mean square of the error between M_{exp} and M_{air} , calculated by the algorithm, gradually decreases by changing the values of A_{DSV} and θ_{cls} .

At the end of the calibration the percentage root mean square of the error reaches a value of 4.85%, while the two scalar parameters are calibrated to the following final constant values: $A_{DSV} = 224.4 \text{ mm}^2$ and $\theta_{cls} = 3.4^\circ$. Therefore, the adopted physical model allows for a good estimation of the air flow. After tuning A_{DSV} and θ_{cls} in the direct DSV model, the reverse model is used to create a set of

values of θ_{ecu} , by sweeping between all of the values of M_{air} and β within the range of the definition of the lookup table.

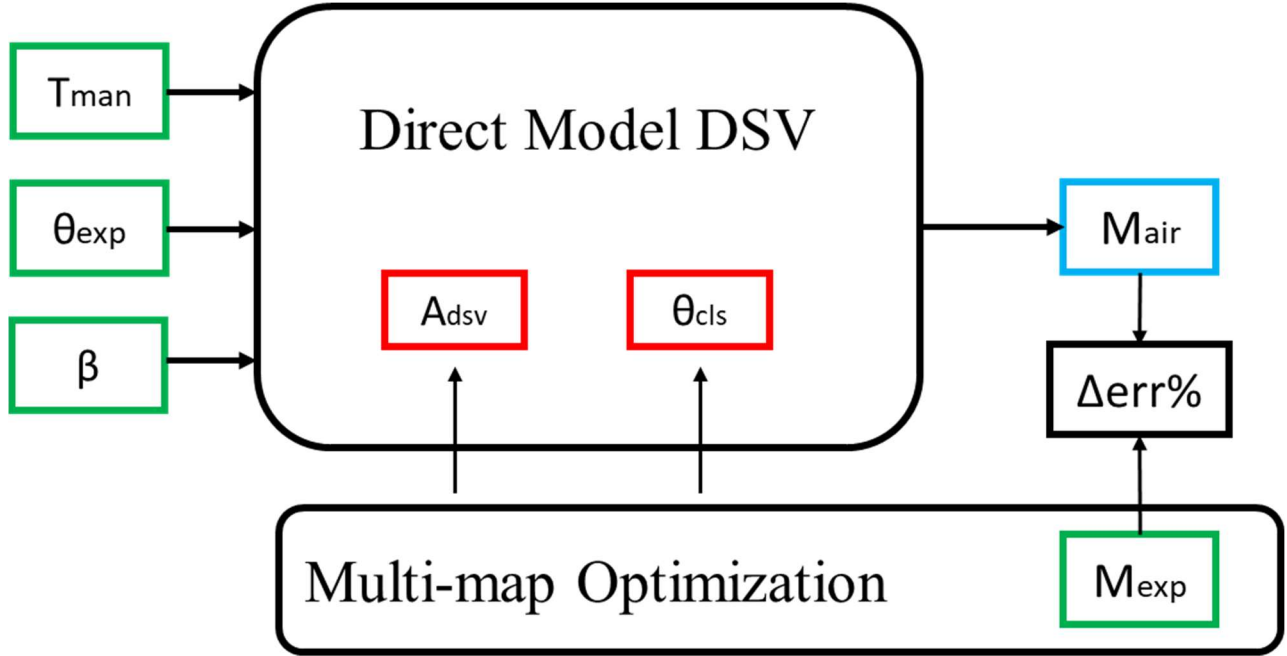


Figure 2.7. De Saint Venant model optimization scheme.

This allows for the creation of a spreadsheet with three columns, which represent two dependent variables and one independent variable. Starting from this spreadsheet, it is possible to use the discrete regression technique to shape the required map for the throttle angle function. To verify the validity of the basic simplified model, the developed automated tool is adopted to estimate the mass flow as a function of all of the acquired channels. The automated procedure could be innovatively used to analyze the variation of the root mean square error as a function of other significant quantities that are not included in the model to have important indications about possible improvements for the standard model. If the error is not correlated with the examined quantity, the graph must show a scattered cloud plot. Conversely, in case of an evident correlation, the points should highlight a definite trend, ensuring the identification of a regression curve that fits the points. This tool sorts the regression results (which can be linear or parabolic) from most to least significant using the following fictitious slope as a yardstick:

$$x(y_{max}) - x(y_{min}) \tag{2.11}$$

The analysis demonstrated a significant dependence on M_{air} , as shown in *Figure 2.8*.

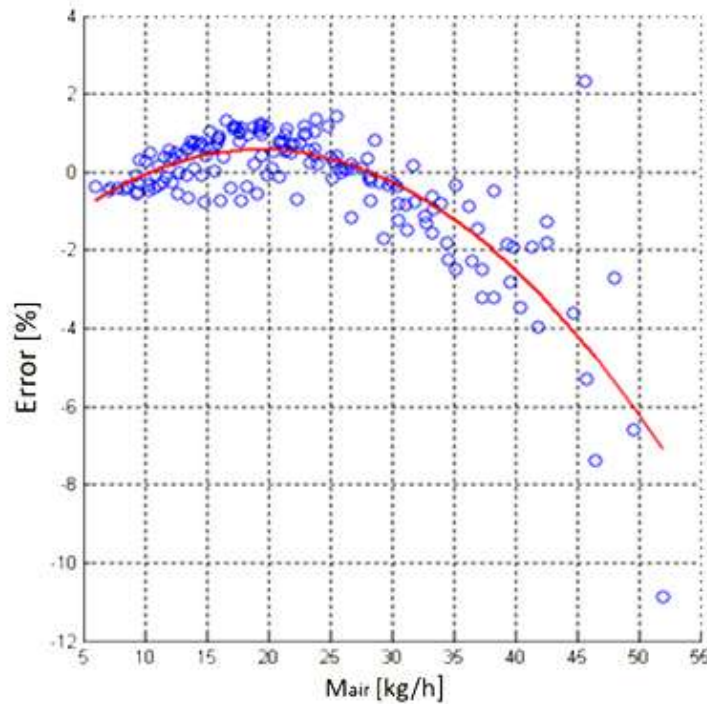


Figure 2.8. Correlation of the error with the mass flow rate

As seen from the graph, the trend of the error is well reproduced by a quadratic with a relatively small standard deviation. The trend is due to an oversimplification of the model, especially for A_{DSV} , which is considered to be a scalar, whereas it includes the discharge coefficient. Therefore, this scalar calibration parameter should more rigorously be represented by a vector to provide different values when the mass flow rate changes due to changes in C_v through the orifice, according to the scheme shown in Figure 2.9.

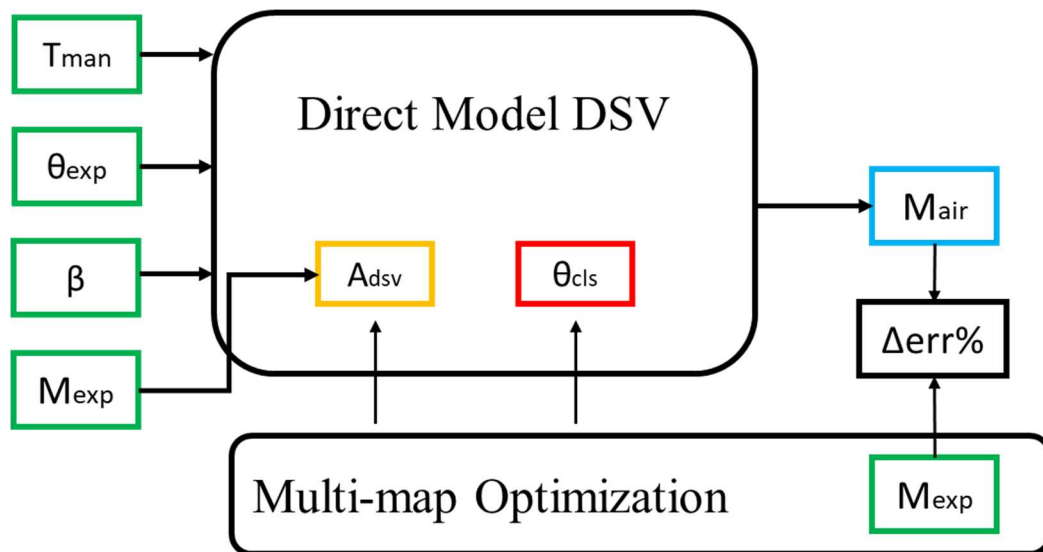


Figure 2.9. Calibration scheme adopted for the vector quantity A_{DSV} in the updated version of the DSV model

In the figure A_{DSV} is represented in orange because it's turned into a vector: for this reason, it will not have a single value, but its value will change depending on M_{exp} . Once the calibration parameter A_{DSV} is turned into a vector within the engine model, the automated calibration tool is executed again. The optimization process takes more time because of the slight complication in the parameter structure. After approximately 600 cycles, the percentage root mean square error for the estimated mass flow rate reaches a value of 2.14%, with an accuracy that is more than doubled compared to the previous case, while the calibration scalar parameter θ_{cls} settles at 5.3° . The results are shown in *Figure 2.10*.

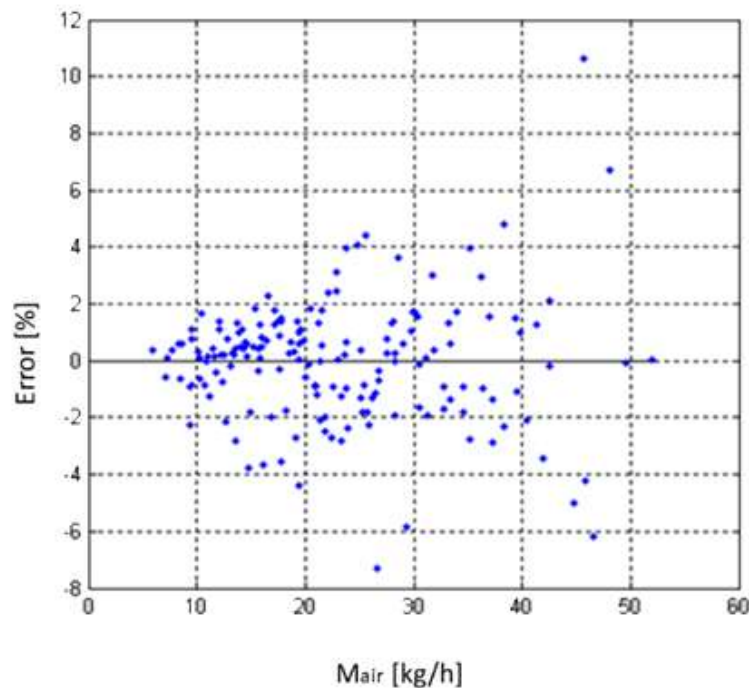


Figure 2.10. Results of regression analysis performed on the updated version of the throttle angle model.

After the new calibration of the direct DSV flow model, the reverse model is used to create a set of data and the discrete regression is used to create the updated map for the throttle angle model. The result is shown in *Figure 2.11*, where the colored surface is the map obtained through the updated model to estimate the throttle angle, while the grey surface is the output obtained when the oversimplified model is used. It should be noted that the second surface is almost completely below the first.

Finally, a further performance comparison between the first and second throttle angle model is performed. In particular, *Figure 2.12* shows the distributions of the error (Θ_{error}) in the throttle angle prediction for both the simplified (on the left) and updated (on the right) model. Both estimation models provide satisfactory results, and the large majority of predicted angles (98.2% in the first case

and 99.4% in the second) fall within the acceptance limits of the ECU calibration (represented by vertical red lines in *Figure 2.12*).

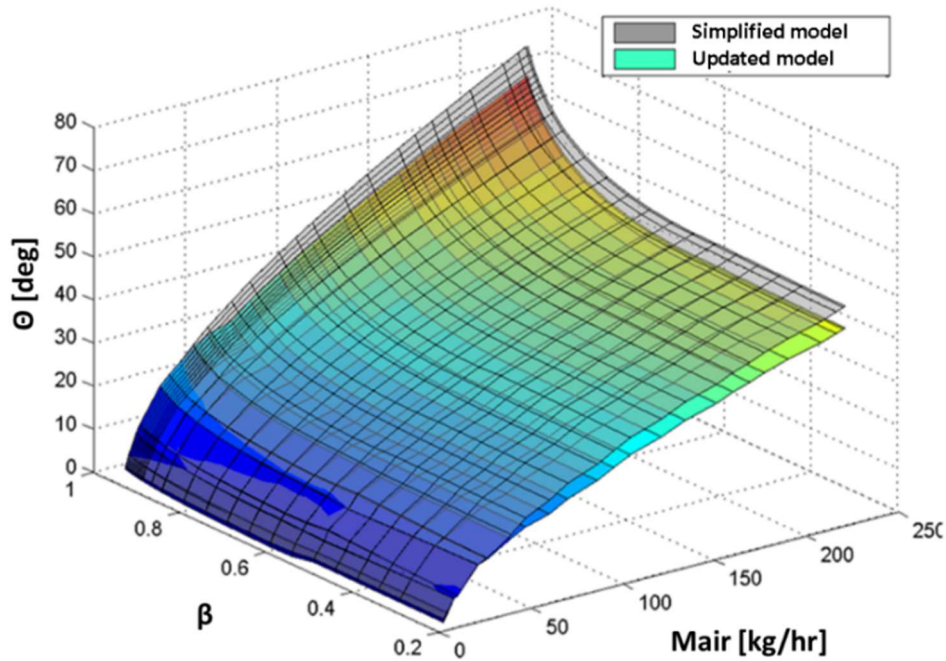


Figure 2.11. Throttle angle map: comparison between the oversimplified (grey surface) and updated version of the model (colored)

However, the updated model allows for an improvement of the calibration performance with a reduction in the error between the estimated and experimental values of the throttle angle. Therefore, the more accurate physical model is definitively adopted for target throttle angle control. This approach has promising results and a better performance, while reducing the development costs.

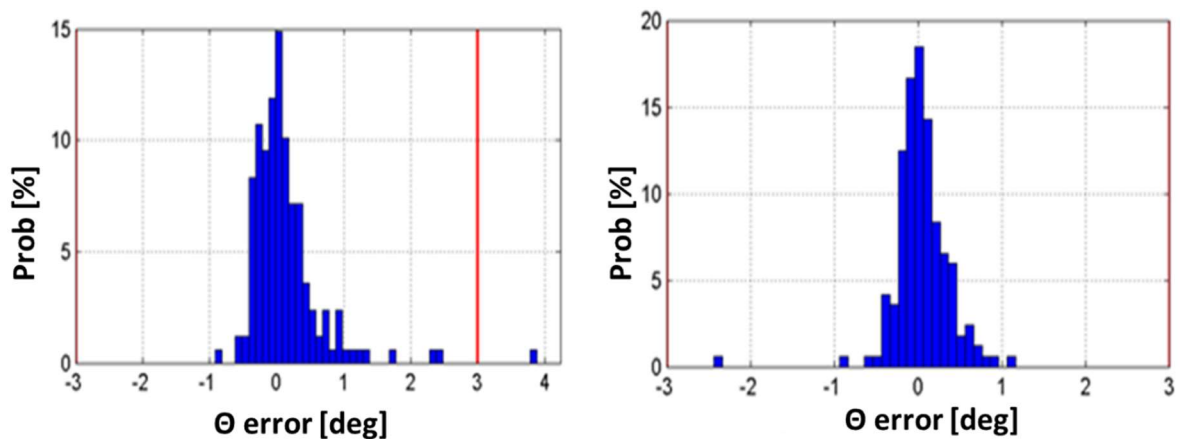


Figure 2.12. Distributions of the error for the throttle angle estimation: simplified model (on the left) and updated model (on the right).

3. Neural networks: radial basis function

Artificial neural networks (NN) are non-linear structures of statistical data organized as modeling tools. They can be used to simulate complex relationships between inputs and outputs that other analytical functions cannot represent. NN can be trained to provide reliable output values of a quantity starting from an adequate number of input variables [34] .

In very general terms, a NN is a system inspired by the functioning principles of the nervous system of advanced organisms [35], consisting of the interconnection of elementary computational units (by analogy also called neurons), with a key feature: knowledge is acquired from the environment through an adaptive learning process [36] [37] and is stored in the parameters of the network, in particular, in the weights associated with the connections. The neurons, which can be seen as nodes of an oriented network provided with processing capacity, receive a combination of signals from the outside or from the other units at the input and transform them through a function, typically non-linear, called function of activation. The output of each neuron is then sent to the other nodes or directly to the network output, through oriented and weighted connections. In function approximation problems (or regression, according to exact terminology), the input is usually a vector of real numbers representing the independent variables and the output represents the dependent variable indicative of the functional link; more generally, inputs and outputs can also consist of real-value function vectors, which represent, for example, temporal trends of some magnitude. The input-output link made by the network essentially depends on:

- the type of elementary units, which can have a more or less complex internal structure and have activation functions characterized by different types of non-linearity;
- the architecture of the network, that is, the number of nodes, the structure and orientation of the connections;
- the values of the internal parameters associated with the elementary units and connections, which must be determined through learning techniques.

Neurons are modelled on the basis of mathematical models: this type of approach is useful in various fields. From the engineering point of view the ideal is to create machines capable of learning in complete autonomy (or partially - in this case it is a supervised learning) and to go back to certain scenarios by reproducing, for example, the human brain features such as the face recognition. Furthermore, as happens in biological memory, the process is also very robust: in fact, it is possible to trace information even if it is communicated with errors (noise).

It is possible to distinguish different types of neural networks, classifying them according to different aspects. A first significant distinction can be made according to the time dependence:

- dynamic networks, in which neurons are units with temporal dynamics and are therefore described by differential equations;
- static networks, in which the link between the inputs and outputs of each unit is supposed to be instantaneous.

A second important distinction, related to the type of connections:

- feedforward networks, (open loop control, forward or predictive) in which the structure of the connections can be represented through an acyclic oriented graph;
- recursive networks, in which there are feedback connections between the outputs and inputs of some pair of units.

Further distinctions can be introduced in relation to the learning methodology used to determine the parameters (coefficients and weights of the network) starting from the data. Learning is generally based on the availability of a training set, consisting of a set of input-output pairs, which can be interpreted as examples of the functional relationship that you want to approximate. A network trained on the basis of the samples of the training set must then be able to generalize, that is to give the correct answer at inputs not considered in the training set and this constitutes the application use of the network in classification problems or regression.

Two basic learning methodologies can be distinguished:

- unsupervised learning, in which the output samples are not known (or are not used), and the network parameters are determined through clustering techniques applied only to the input samples;
- supervised learning, in which the network parameters are determined also taking into account the outputs related to the training samples, most often taking into account human feedback, downstream of the classification process. These feedbacks are therefore added to the knowledge base of the network (knowledge base), which over time becomes richer, tending to always provide better results (learning).

Another important distinction, relating to learning methodologies, concerns the ways in which the set of training samples is acquired or used during learning. From this point of view it can be distinguished:

- online learning, in which the examples of the training set are acquired (or used) incrementally during the training process;

- batch or offline learning, in which it is assumed that the whole training set is available before the training starts.

In the methodology, one of the most common and studied classes of neural networks has been considered: the RBF (radial basis functions) feedforward networks. The main advantages related to the use of the RBF are [38]:

- training methods that require substantially little time and resources;
- much simpler architecture than other types.

Regression has the purpose of making predictions (for example to predict future data of a time series), statistical inference, to test hypotheses or to model dependency relationships. This is carried out on the basis of a training set of initial data indicated as follows [39]:

$$T = (x_i, \hat{y}_i) \quad (3.1)$$

Where $i = 1, \dots, n$

The value of \hat{y}_i indicates that the value of the response variable is not exactly determined, as it could be affected by dispersion or distorted by measurement errors. In other words, the precise value of y is unknown: only a value is known which will be affected by a certain alteration.

The function in question can be obtained by considering the following model:

$$f(x) = \sum_{j=1}^m \omega_j h_j(x) \quad (3.2)$$

expressed as a linear combination of a set of m functions $h_j(x)$ called basis functions (from the analogy with the concept of vector, formed precisely by a linear combination of bases), and parameters ω called weights.

For $h_j(x)$ a particular class of functions is chosen, called radial functions: these have the characteristic of decreasing or increasing monotonically, as the distance of the points of the function increases from a fixed center. A typical example is the Gaussian function which takes the mathematical form:

$$h(x) = e^{-\frac{(x-c)^2}{r^2}} \quad (3.3)$$

whose regulatory parameters are the center c (or centroid) and the radius r (or spread) that denotes the distance of the points of the function from the center. The Gaussian function, for its part, decreases monotonically moving away from the center.

Another radial function with similar properties, is the direct multiquadratics:

$$h(x) = \sqrt{1 + \frac{(x - c)^2}{r^2}} \quad (3.4)$$

it grows monotonically moving away from the center. *The Figure 3.1* shows a Gaussian function with $c = 0$ and $r = 1$ and compared with a multiquadratic.

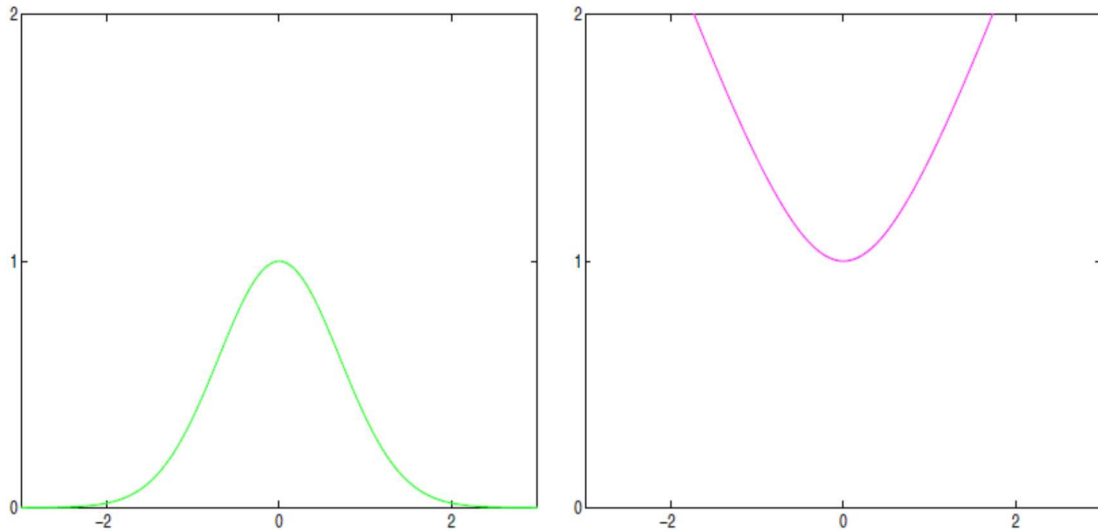


Figure 3.1 - Trends of the Gaussian radial function (green) and the Multiquadratic function (magenta).

By inserting one of these particular functions in the expression of $f(x)$, an RBF is obtained. A set of such functions can be used in a neural network as activation functions.

Such a network, whose schematization is shown in the *Figure 3.2*, is made up of three layers [40]:

- an input layer, directly connected with the sensory units (training set);
- a hidden layer, seat of the neurons in which non-linear transformations take place by means of the RBF;
- an output layer.

The RBFs that act as activation in the neurons of the hidden layer, have centers selected from the input data, called centroids, which constitute the nodes of the layer itself. Each of the samples in the input set feeds these nodes and in particular the functions that transform them. The resulting function $f(x)$ is therefore the approximator of a series of m d-dimensional, nonlinear functions, supplied at the output to the output layer as a linear combination of the same functions,

$$f(x) = \sum_{i=1}^m \omega_i h_i(x)(\|x - c_i\|) = H\omega \quad (3.5)$$

Where:

- ω_i are the weights of the vector ω to be determined, calculated in such a way that the distance between the final predictive model and the RBF is tending to zero;
- $\|x - c_i\|$ expresses the Euclidean distance between a centroid and the points of the entrance set;
- m it is the matrix of all RBFs and is called the interpolation matrix;
- H , in addition to representing the number of RBF, it is also the number of neurons in the hidden layer; each of these neurons acts in a localized region of space transforming the data assigned by the input. The activation of one of these neurons is determined by the distance between the input vector and the predictive vector of the response.

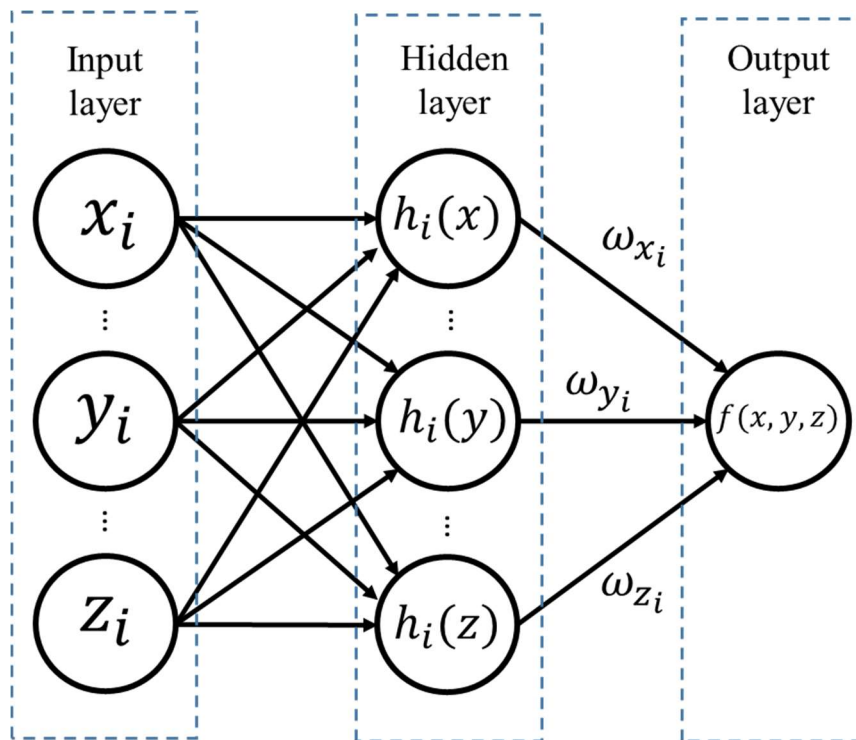


Figure 3.2 – schematization of the structure of an ANN

Then solving the system (3.5) the approximation function is obtained. The H matrix must be chosen under certain conditions, expressed by the Micchelli theorem:

“the interpolating matrix H of dimensions $m \cdot m$ whose elements are:

$$h_{ji} = h(\|x - x_i\|) \tag{3.6}$$

is a non-singular matrix”

A singular matrix is a square matrix with determinant equal to 0. In particular, no singular matrix is invertible. There are numerous functions capable of satisfying Micchelli's theorem; these include the four classes of radial functions most used (but they are not the only ones) for which reference will always be made below:

- Gaussian;
- Direct multiquadratic;
- Inverse multiquadratic;
- Cauchy.

Data (which will be conventionally called training set) must be presented to the network in the form of input-output pairs (patterns). In order to obtain the most precise approximation $f(x)$ possible of the objective function, the training algorithm has the purpose of determining the weights, but before that, of the distance $\|x - c_i\|$ for each function, known as radius or spread factor.

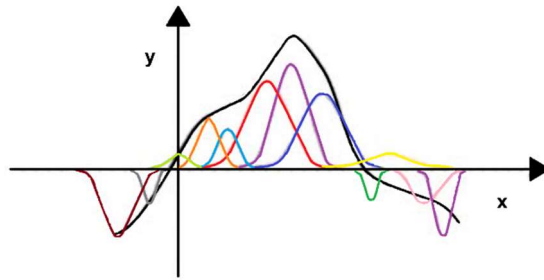


Figure 3.3 - Regression example with Gaussian RBF for the points of a generic training set.

Figure 3.4 shows the influence of the spread factor of the to the Gaussian function (3.3). It's an important parameter used to obtain the trend in Figure 3.3.

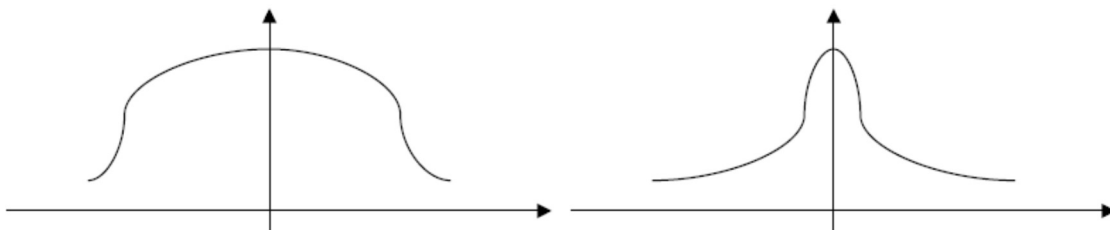


Figure 3.4 - spread factor influence

Neurons show greater sensitivity to data points near the centroid. For the Gaussian function, as for any other RBF, this sensitivity, which determines the shape of the curve, can be adjusted by modifying the spread factor r . In fact, a larger value implies a lower sensitivity to directional gradients, while

the opposite happens for lower values. Two alternatives are considered for the determination of the spread factor:

- 1) a constant value for all the functions; it can be selected according to the following expression:

$$r = \frac{d_{max}}{\sqrt{2m}} \quad (3.7)$$

where m is the number of centers and d_{max} is the maximum distance between centers. This option provides a compromise between roughness and smoothness of the function $f(x)$. It could lead to an optimal solution if data are uniformly distributed in the input layer, resulting in a uniform distribution of centroids. Unfortunately, real cases show non-uniform data distributions. The method is therefore inadequate in practice and the assumption of a constant spread for all functions should be avoided.

- 2) The second alternative consists in independently estimating the spread for each Gaussian function. This can be done by calculating the standard deviation of the distance between the available data and the corresponding centroid. Spread factors can be calculated as follows:

$$r_i = \frac{1}{N} \left(\sum_1^n (\|c_i - c_j\|^2) \right)^{\frac{1}{2}} \quad (3.8)$$

where c_i are the n centroids near to the centroid in question c_j , with a value of two suggested for n . Further approaches combining both the above alternatives have been also proposed. More comprehensive and rigorous discussions can be found in [41] [42] [43] or other specialized literature.

3.1. The proposed methodology: neural networks applied to the engine calibration process

The methodology proposed in this work enables a redefinition of the previous scheme according to the enhanced base calibration process depicted in *Figure 3.5*. In particular, the traditional experimental campaign is replaced by a redesigned (reduced) bench test activity where much less engine operating conditions are acquired if compared to those required by traditional calibration processes. The reduced experimental campaign is then performed and the related set of measured data is obtained. Neural networks are then adopted to enlarge the reduced datasheet, thus numerically estimating the missing operating conditions and providing a virtual datasheet (here called VDS). The VDS is then used as input to the computer aided calibration algorithm and the calibration process is carried out as previously described.

Specifically, to verify the effectiveness of the proposed methodology, a complete set of available experimental data has been used in this paper. An increasing fraction of these measured quantities related to whole engine operating conditions have been subsequently cut.

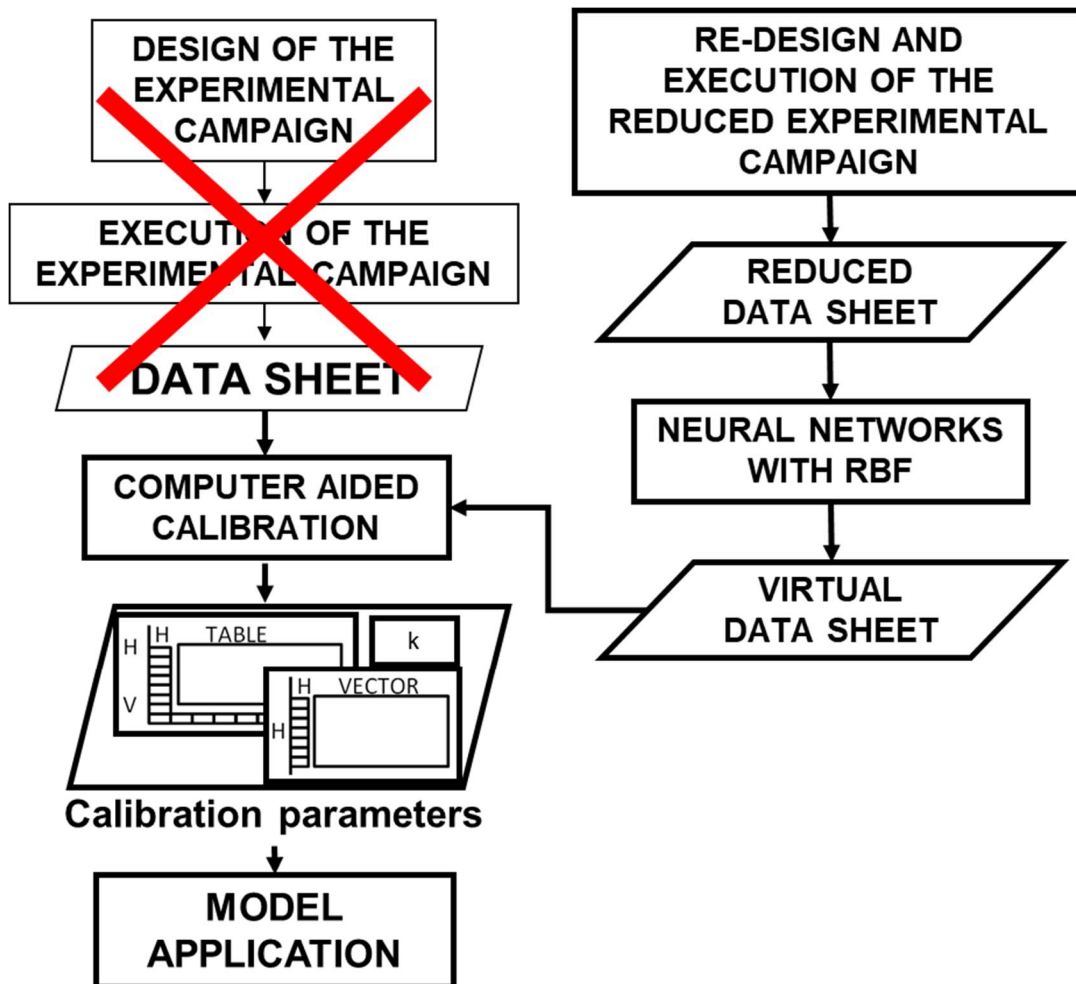


Figure 3.5 - Detailed scheme of the enhanced calibration methodology.

The resulting reduced data sheets have been then adopted as input to the neural network to obtain extended sets of data characterized by the same number of data which characterized the original data sheet. These reconstructed sets of data (VDS) have been then used to calibrate the volumetric efficiency function of a reference two-cylinder turbocharged spark ignited engine. Finally, the calibration performance achievable by applying different cutting rates to the original experimental data have been compared.

3.2. Analysis and results: Application of the methodology to the Calibration of the Volumetric Efficiency Function

In this paragraph, a NN with Radial Basis Functions has been used to reduce the experimental effort required for the calibration of the volumetric efficiency function implemented into the ECU of the reference internal combustion engine whose characteristics are shown in *Table 2.1*. To this aim, starting from the experimental datasheet usually used for the calibration of the volumetric efficiency function and previously adopted to achieve the results represented in *Figure 2.4*, an increasing number of rows, which represents the number of measured engine operating conditions, has been randomly deleted from the available set of data. The reduced datasheet is used to train the neural network whose structure is represented in *Figure 3.6*. In this way, the neural network is used to estimate the volumetric efficiency represented in equations (1.1) and (1.2) in the operating conditions whose experimental data have been previously deleted. Finally, the reconstructed data sheet is used for the calibration of the ECU function under investigation. Eventually, the calibration performance achieved is compared to the reference calibration obtained through the application of the calibration process to the original data sheet.

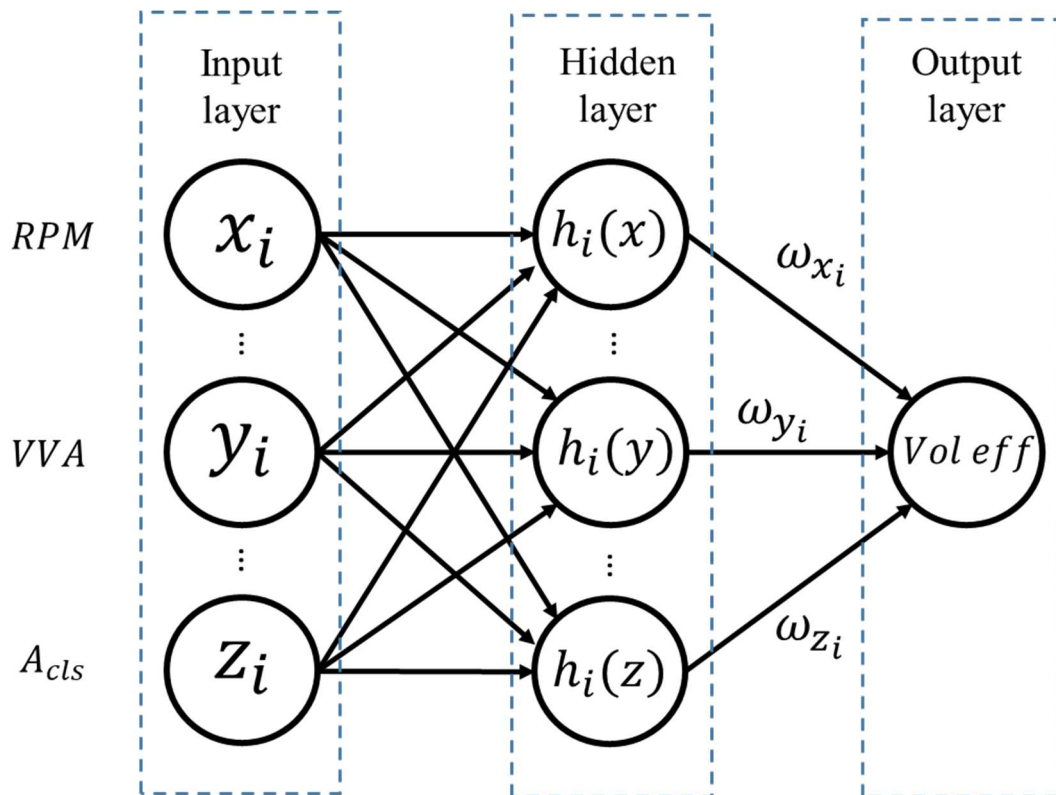


Figure 3.6 - Structure of a neural network with specification of the ECU engine quantities adopted within the input and output layers

As represented in *Figure 1.6*, the maps of volumetric efficiency function are dependent on *RPM*, *VVA*, and *A_{cls}*. In *Figure 3.6*, the input layer, x_i represents the parameter *RPM*, y_i the values of *VVA* and z_i the values of *A_{cls}*, i represents the i -th experimental condition, while the volumetric efficiency has been set as dependent variable and its values are obtained as output. The neural network defines a functional relationship between the input and the output, providing estimation values for the volumetric efficiency in the operating conditions previously deleted. Therefore, a mixed experimental-numerical datasheet (here called virtual datasheet) consisting of 680 operating conditions, which includes the same operating conditions previously deleted, can be generated. The proposed methodology is validated using the virtual datasheet as input to the calibration software as represented in *Figure 3.5* The volumetric efficiency function is then calibrated and the calibration performance compared with that obtained through the complete experimental datasheet. The results achieved with a random reduction of 40, 50 and 60% of the experimental values for the volumetric efficiency are reported and discussed.

In order to be sure of the effectiveness of the methodology, two tests have been carried out with the aim of understanding whether the neural networks have been capable of assessing the values of volumetric efficiency under certain operating conditions. The steps of the two tests are:

1. Cutting the datasheet by 40% (70% in the second test).
2. Use of the remaining operating conditions to train neural networks, recreating the link between input (*RPM*, *VVA*, *A_{cls}*) and output (*Volumetric Efficiency*).
3. Recreate the volumetric efficiency values by imposing the operating conditions cut in point 1 as input.
4. Comparison between the values of volumetric efficiency obtained with neural and experimental networks.

When a 40% cut of the available data is adopted, a training set of 422 operating conditions is obtained, which constitutes the initial set of data used to train the neural network and return a complete set of 680 operating points.

Table 3.1 - Errors achieved for the volumetric efficiency obtained by NN after a 40% cut of the original datasheet.

	Training set	RBF points	Max error	Min error	Mean error	StD	MSE
Absolute	422	680	0.03	2.28E-06	-2.15E-05	6.82E-04	6.82E-04
Relative			6.92	3.46E-05	-0.06	1.28	1.28

In this way, the deleted experimental values of the volumetric efficiency are calculated by feeding the RBFs with the values of the independent variables corresponding to the deleted operating conditions.

Table 3.1 summarizes the absolute and the relative error assessed by the difference between the volumetric efficiency calculated by the neural networks and the experimental volumetric efficiency for the first test carried out with a 40% cut of the datasheet and its subsequent reconstruction through the neural networks. It can be noted that the maximum relative error is less than 7%. Figure 3.7 shows the relative and absolute error distribution.

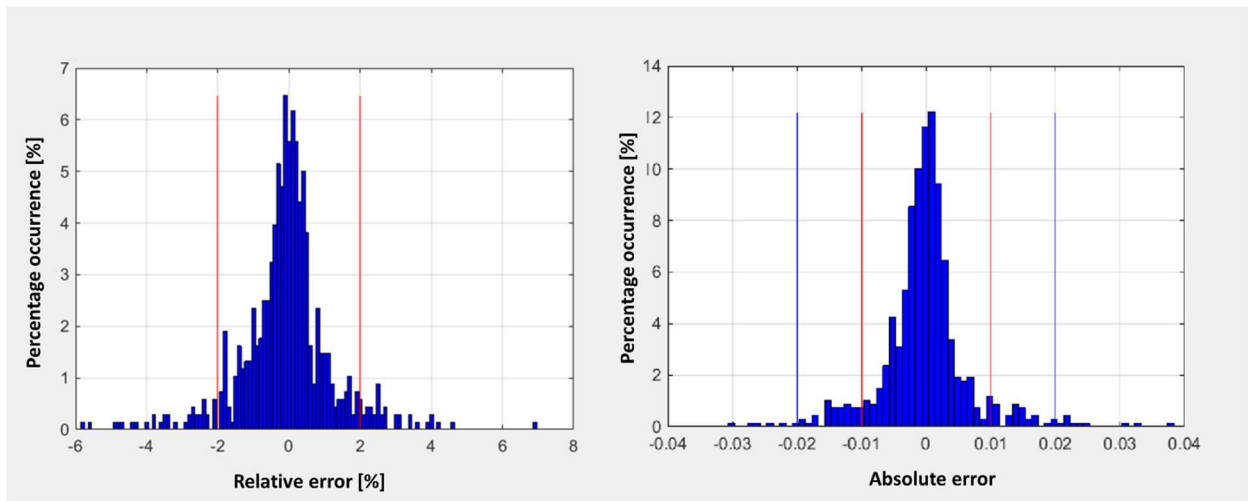


Figure 3.7 - Error distribution for the volumetric efficiency after a 40% cut of the original datasheet.

It can be noted that 89.26% of the relative error is within $\pm 2\%$. Furthermore, the distribution of the absolute error shows that 97.79% of the values are within the range of ± 0.02 and that 87.5% of the values fall within the range of ± 0.01 . These results are very positive and show the ability of the NNs to recreate the volumetric efficiency values from inputs as RPM , VVA and A_{cls} with a very low absolute and relative errors.

Table 3.2 - Errors achieved for the volumetric efficiency obtained by NN after a 70% cut of the original datasheet.

	Training set	RBF points	Max error	Min error	Mean error	StD	MSE
Absolute	210	680	0.05	4.46E-06	-4.62E-05	0.01	0.01
Relative			24.06	5.73E-05	-0.41	3.84	3.86

La *Table 3.2* summarizes the absolute and the relative assessed by the difference between the volumetric efficiency calculated by the neural networks and the experimental volumetric efficiency for the second test carried out in the case of the random cutting of the original datasheet of 70% and its subsequent reconstruction through the use of neural networks. In this case, it can be noted that the errors between volumetric efficiency obtained from neural networks and experimental volumetric efficiency begin to become high: in fact, the maximum relative error is greater than 24%.

Again, it is reported in *Figure 3.8* the distribution of both relative and absolute errors. It can be noted that 53.53% of the relative error remains between $\pm 2\%$, while as regards the absolute error, 85% of the values are within the range of ± 0.02 .

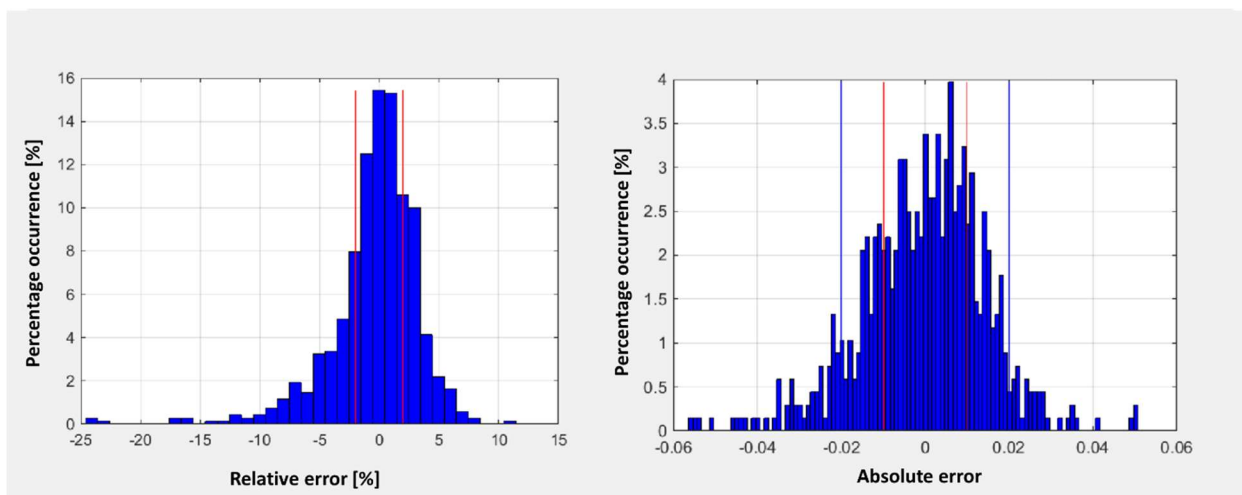


Figure 3.8 - Error distribution for the volumetric efficiency after a 70% cut of the original datasheet.

This shows that a too high fractionation of the original datasheet can lead to too high errors in the assessment of the volumetric efficiency, and consequently of the performance of the function calibration. The performance of the calibration of the volumetric efficiency function is shown below by making gradually higher random cuts, with cuts of 40%, 50% and 60%.

3.3. Analysis and results

La *Figure 3.9* shows the performance of the calibration using the original datasheet. The 660 operating points are used to calibrate the parameters a , b and c of the volumetric efficiency function (see equations (1.1) and (1.2)) and the estimated values by the function of the volumetric efficiency have been compared with those measured at test bench at the same operating conditions.

In this case, 95.44% of the values falls within the acceptance range of $\pm 5\%$, showing a very high calibration performance.

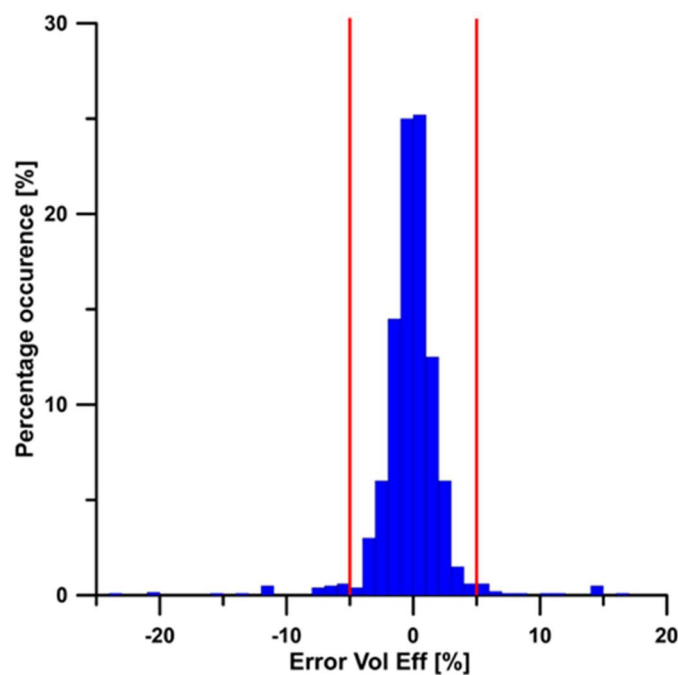


Figure 3.9 - error distribution for the calibrated volumetric efficiency function using a datasheet containing 660 experimental conditions

The VDS previously obtained through the use of neural networks with a 40% cut, it is made up of 60% of real operating conditions and 40% of virtual operating conditions. The datasheet thus obtained has been used as input in the computer aided calibration to calibrate the maps a , b and c of the volumetric efficiency function. The software recalls the channels necessary for calibration, which include both experimental and virtual ones.

Figure 3.10 shows the performance of the calibration using the 40% virtual datasheet.

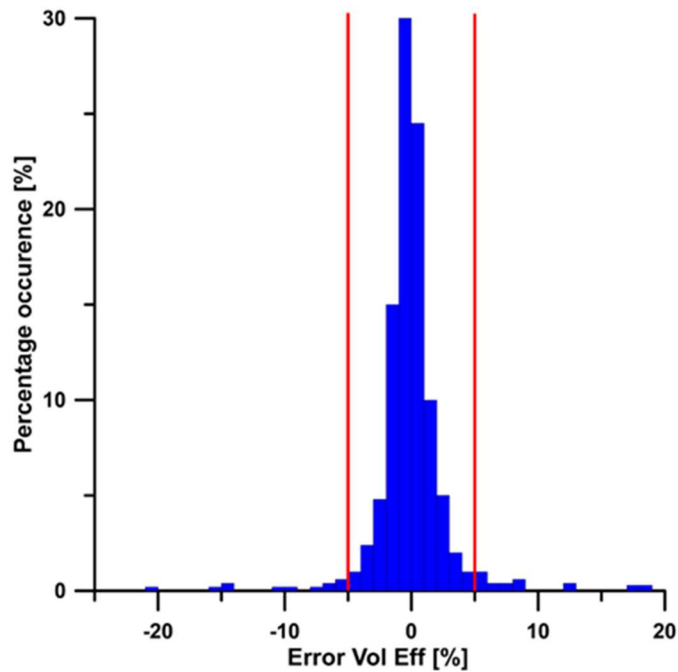


Figure 3.10 - Error distributions for the volumetric efficiency function: calibration achieved by using NN methodology after a 40% cut

In this case the calibration performance remained almost unchanged, going from a percentage of the 95.44% to a percentage of the 94.71%. Almost the same calibration performance can be obtained despite a 40% cut to the experimental acquisitions, given that 94.71% of the values fall within the acceptability range, remembering that a performance of 90% can be considered acceptable.

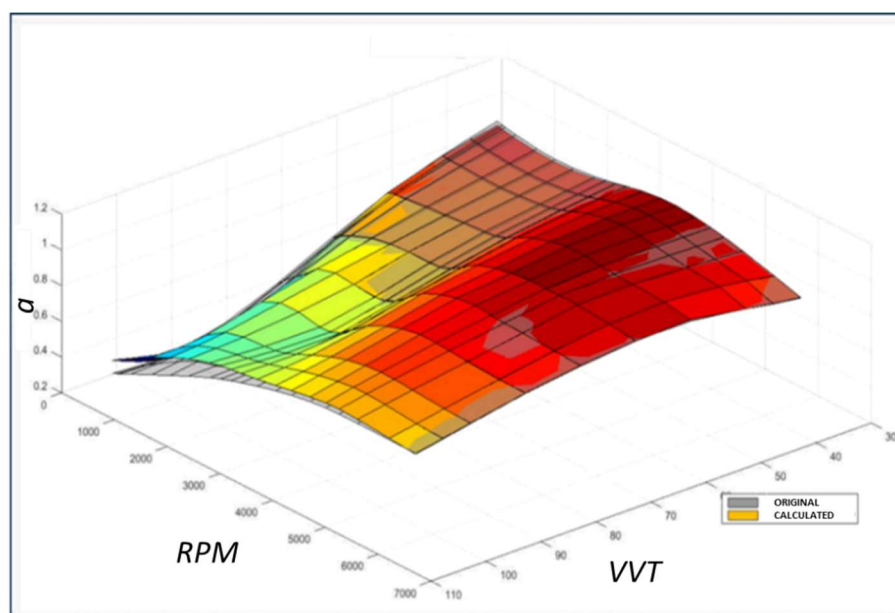


Figure 3.11 - Response surfaces for the parameter “a” obtained from the original data set and NN recalculations.

Figure 3.11 compares the response surfaces obtained for the calibration parameter a once calibrated by using the original experimental data set in input to the calibration algorithm (the grey surface) and the other by adopting the VDS (colored surface). It can be noted that the two surfaces are mostly overlapped.

To verify the potential of the proposed methodology, further calibration processes have been performed after randomly cutting the original experimental data set by 50% and 60% respectively. In the last two cases, a residual number of 339 and 279 operating conditions remain for the training of the NN before the calibration of the target ECU function is performed.

The methodology applied is the same: after training the neural networks, the 321 and 381 points previously deleted have been reconstructed respectively, and use these VDS as input in the computer aided calibration in order to verify the performance of the calibration of the volumetric efficiency function.

Again, results show no significant degradation of calibration performance even if a 60% reduction of the original data set is considered, as demonstrated by Figure 3.12.

In fact, in the first case the 94.26% of the values falls within the acceptable range. A slightly lower percentage of 93.68% falls within the acceptable range even if a 60% reduction of the data set is accepted, showing a calibration performance reduction of approximately 2% if compared to the result achievable using the original data from dynamometer tests.

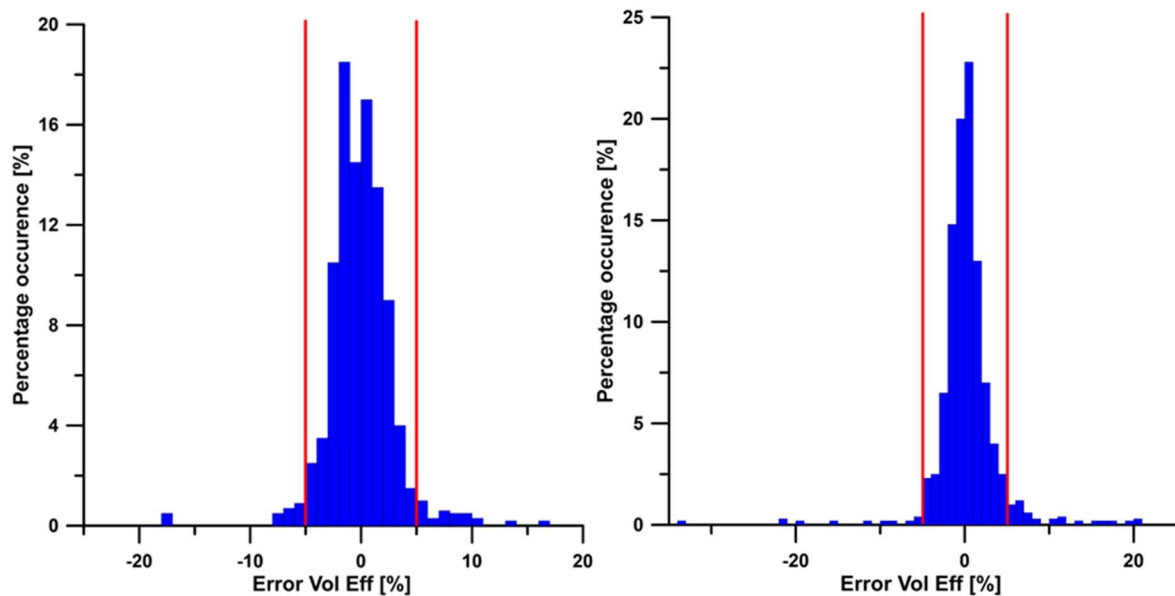


Figure 3.12 - Error distributions for the volumetric efficiency function: calibration achieved by using NN methodology after a 50% cut (on the left) and 60% cut (on the right) of the original data set.

Ultimately, the proposed methodology has demonstrated great effectiveness and promising results, showing how the experimental effort related to the calibration process could be significantly reduced while maintaining similar calibration performance.

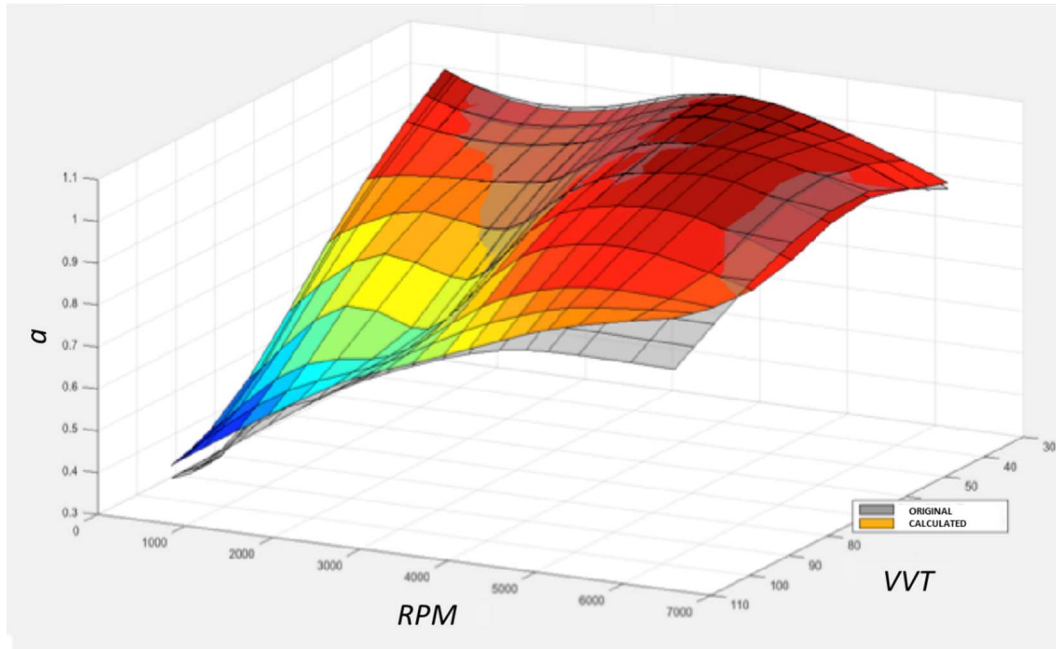


Figure 3.13 - Response surfaces for the parameter “a” obtained from the original data set and NN recalculatation after a 60% cut of the original datasheet.

Also in this case, as shown in *Figure 3.13* the response surfaces of the parameter a evaluated using the 60% reconstructed datasheet as calibration input is almost completely superimposable on the original one.

This paragraph addresses a methodology used to overcome some critical issues concerning the base calibration of ECU estimation functions in engine management systems. Specifically, this research proposes an effective methodology based on the use of Neural Networks to provide a detailed engine data sheet starting from a reduced number of experimental data. The potential of the proposed methodology has been verified using this detailed data set as input to a specific Computer Aided Calibration algorithm and the achievable calibration performance has been evaluated. In particular, the methodology has been applied to the calibration of the volumetric efficiency function implemented in the electronic control unit of a modern downsized engine. The research clearly demonstrates the effectiveness of the proposed approach since the calibration performance falls within acceptable limits even after a 60% cut of the experimental data usually acquired for calibration purposes. The results highlighted that the proposed methodology may lead to a reduction of development time and costs of the calibration process due to a reduction of the experimental effort.

In fact, a cut from 40 to 60% of to the available experimental data can be accepted while obtaining similar calibration performance.

The recommended software to implement the first methodology is a programming platform where it's possible to develop calculation codes to interface with the control unit software. There are many on the market: MATLAB®, developed by the Mathworks® company, is the most used in the industries and has a cost that varies between 10'000 and 15'000 €/year, but there are many that are also free , such as SCILAB®, Octave®, FreeMat®, R® and IDL®.

The code developed in any programming environment must be processed by additional software, e.g. INCA, developed by ETAS, the most widespread in the AUTOMOTIVE field, for communication with the control unit. Even for this software, for a company, the cost varies between € 10-15,000/year. The use of these softwares requires in-depth computer knowledge, especially as regards the use and implementation of neural networks, and a good knowledge of motor physics.

4. Second proposed methodology: 0D-1D engine model applied to the engine calibration process

Chapter 3 is dedicated to the description of the first methodology that can lead to a reduction of experimental tests of the engine base calibration process using neural networks. This method is effective, since, despite a reduction that goes from 40 to 60% of the original experimental datasheet, the calibration performances are still high.

In the remaining chapters, a second methodology is described in detail which can lead to an even higher reduction of the experimental tests to be carried out on the test bench.

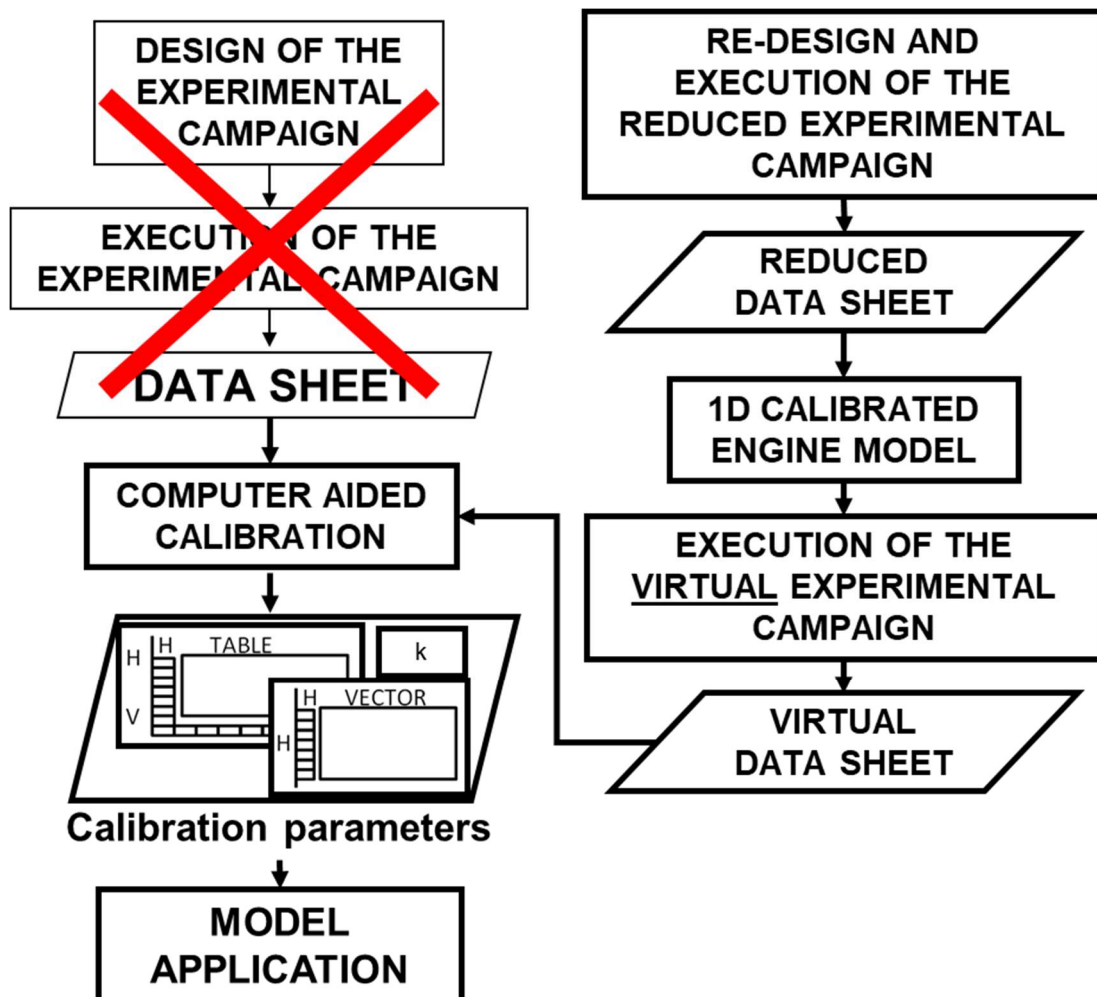


Figure 4.1 – main stages of the proposed methodology

The Figure 4.1 schematizes the main stages of the proposed methodology. As can be seen, the goal of reducing the experimental tests is pursued with the help of the 0D-1D simulation models.

In this Thesis work, the 0D-1D models are used with an innovative approach: it is intended to use the 0D- 1D engine models as virtual test benches in order to carry out extensive experimental campaigns and to obtain all the fundamental quantities for the calibration of the control unit functions. In order to carry out extensive experimental campaigns, it is necessary to use validated and robust 0D-1D models. The validation, described extensively in chapter 5, has been carried out with a multi-objective multi-variable validation process. The new methodology does not completely eliminate the experimental tests currently performed on the test bench, but they are deeply reduced. In fact, only the experimental tests necessary to validate the engine model are required, resulting in a reduction of the tests from thousands to a few tens. The final aim of this line of research is to provide general guidelines, so that the methodology can be used in an industrial context.

In recent years, in the automotive sector, simulation has been used more and more. The simulation of engines and vehicles has ever wider applications, especially in the research and development phase. The design and development of ICE solicits research that can be generally classified according to two main orientations:

- the first is essentially aimed at analysing existing engines. Its purpose is to check and optimize the performances in different operating conditions;
- the second has the main objective of designing a new engine, through the definition of the engine configuration and its main geometric sizes.

In both lines of research, an experimental approach prevailed in the previous years. This is mainly due to the complexity of the physical phenomena that take place inside an internal combustion engine. Just think that the steady state operation of an ICE is not stationary but periodic while the equations that regulate mass transport in the pipes are non-linear and therefore do not lend themselves to an analytical solution. Moreover, the physics that regulates the phenomena of turbulence, combustion and fuel injection is not entirely known. This level of complexity perfectly explains why an experimental approach has been adopted over the years.

The advent of increasingly high-performance computers has allowed a significant acceleration of research: nowadays it is possible to calculate all the thermo-fluid dynamical characteristics of the internal combustion engine using complex mathematical models.

The mathematical models of a system are a collection of equations. The nature of the equations (algebraic or differential, with ordinary or partial derivatives) qualifies the type of model

(instantaneous or dynamic, with concentrated or distributed constant parameters, while their number, together with the interactions between the different variables, quantifies the complexity of the model.

Any mathematical model has three primary objectives:

1. describes the system under study through well-defined (qualitative and quantitative) relationships;
2. interprets the phenomenology in question, highlighting the possible presence of constituent subsystems and clarifying the nature of the mutual relations;
3. predicts qualitatively and quantitatively the behaviour of the system, i.e. the temporal evolution of certain quantities (of output) when other quantities vary (input).

It is appropriate to underline that the predictive intent of a mathematical model probably constitutes its most interesting aspect.

The construction of a mathematical model requires making choices, favouring certain phenomena considered dominant over others. This choice defines the hypotheses and the limits of the model that will be created.

The process of realization, calibration and validation of a mathematical model cannot be separated from comparison with experimentation, which becomes the only referee able to demonstrate the goodness of the choices made.

4.1. 0D/1D equations: volumes and pipes

Generally, the mathematical models used to describe the physical phenomena of a reciprocating internal combustion engine can be classified considering the spatial dependence, or the number of dimensions used to describe the phenomenon. *Table 4.1* shows the approaches typically implemented, taking into account the number of dimensions used in the schematization.

Table 4.1 - Classification of the numerical approaches and typical application

Model type	Typical Application
0D	Combustion
1D	Gas Exchange
Quasi-Dimensional	Combustion
3D	Flow Field, Combustion

In zero-dimensional (0-D) approach, the properties of the control volume do not depend on space, but only on time. The flow properties are dependent on the thermodynamic state (pressure and temperature) and cost throughout the control volume. It is not recommended to use this approach in the intake and exhaust pipes due to the failure to describe the pressure waves.

One dimensional (1-D) approach allows to overcome the limitation of the 0-D approach, since it solves the unsteady equation along the mean flow direction. It is useful to apply these equations in conduits where one direction is predominant over the others. In this way, it is possible to recreate the phenomenon of pressure waves that affect the behaviour of the ICE by travelling in the intake ducts. In this approach, every thermo-fluid-dynamic propriety is considered uniform along each section of the pipe.

Three-dimensional methodologies (3-D) are based on the integration of the Navier-Stokes equations, giving detailed fluid-dynamic information for the complex 3D domains. These models, due to their relevant computational effort, are applied for the simulation of the unsteady mean and turbulent flow motion within a limited portion of the engine, usually intake air-box, after-treatment devices and cylinder, for a reduced set of operating conditions

Generally, the described methodologies are used with a mixed approach. 0-D or 3-D equations can be used to describe phenomena within volumes, such as the air box or cylinders. 1-D equations are used to describe physical phenomena within pipes [44].

A mixed approach has been used in this Thesis, considering volumes, such as cylinders, with a 0-D approach and conduits with a 1-D approach. The latter are widely used for the analysis of the global engine performance due to the good compromise between accuracy and computational time.

In details, in the volumes only the mass and energy conservation equations, eq.(4.1) and (4.2), are solved as a function of time. They can be detailed for in cylinders application and written as follows:

$$\frac{dm}{dt} = \dot{m}_{in} - \dot{m}_{ex} + \dot{m}_{inj} \quad (4.1)$$

$$\frac{d(me)}{dt} = -p \frac{dV}{dt} - \frac{dQ_w}{dt} + \dot{m}_{in}h_{in} - \dot{m}_{ex}h_{ex} + \dot{m}_{inj}h_{inj} \quad (4.2)$$

Equation (4.1) is a mass balance equation applied to the cylinder, where \dot{m}_{in} is the input mass flow rate, \dot{m}_{ex} is the output mass flow rate and \dot{m}_{inj} is the input fuel flow rate.

Equation (4.2) is an energy balance applied to the same control volume as (4.1) as schematized in *Figure 4.2*. The term $-p \frac{dV}{dt}$ represents the mechanical energy exchanged between the flow and the

piston, $-\frac{dQ_w}{dt}$ the thermal power exchanged with the cylinder walls while the terms h_{in} , h_{ex} and h_{inj} are the energy contributions due respectively to the input mass flow rate \dot{m}_{in} , the output mass flow rate \dot{m}_{ex} , and the fuel flow rate \dot{m}_{inj} .

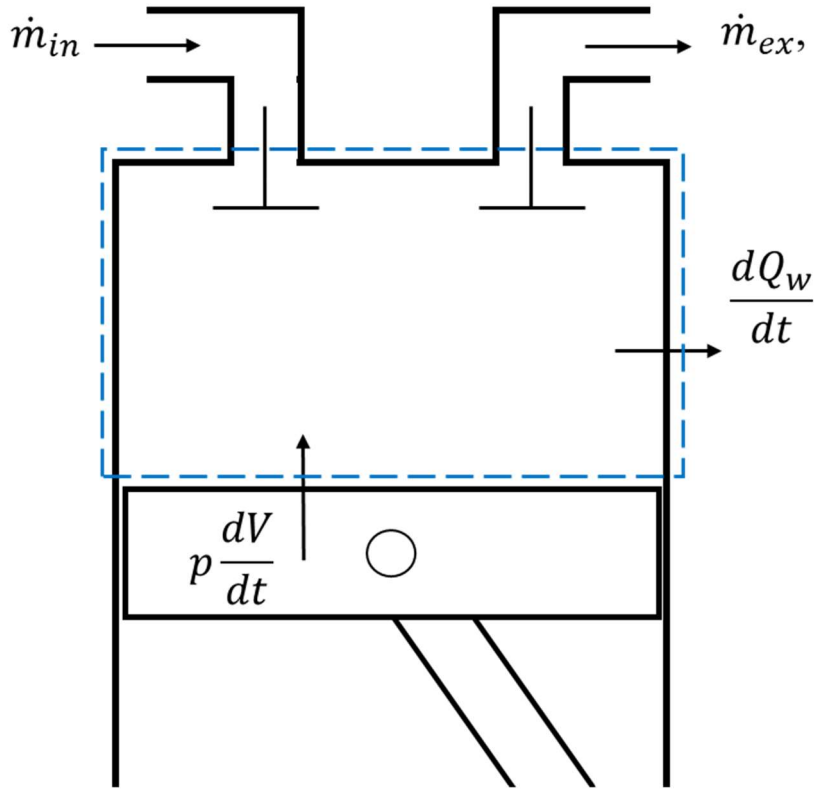


Figure 4.2 – 0D cylinder schematization

Equation (4.2) can be reformulated considering the internal energy of the system as a function of temperature and composition:

$$\frac{dt}{dt} = \frac{1}{mc_v} \left(-p \frac{dV}{dt} - \frac{dQ_w}{dt} + \dot{m}_{in} h_{in} - \dot{m}_{ex} h_{ex} + \dot{m}_{inj} h_{inj} - e \frac{dm}{dt} - \frac{\delta e}{\delta t} \frac{dx_b}{dt} \right) \quad (4.3)$$

The isentropic flow equation is used to evaluate the instantaneous mass flow in and out of the cylinder, which can be characterized according to the conditions of sonic flow (eq. (4.4)) or supersonic flow (4.5).

$$\frac{dm}{dt} = c_d A_{ref} p_1 \sqrt{\frac{2k}{k-1} \frac{1}{RT_1} \left[\frac{p_2^{\frac{2}{k}}}{p_1} - \frac{p_2^{\frac{k+1}{k}}}{p_1} \right]} \quad (4.4)$$

Where p_1 and p_2 are respectively the upstream and downstream valves' pressure, T_1 is the upstream valves' temperature, A_{ref} it is the reference passage area that takes into account the opening of the intake and exhaust valves, R e k are properties of gas.

$$\frac{dm}{dt} = c_d A_{ref} p_1 \sqrt{\frac{k}{RT_1} \left[\frac{2}{(k+1)} \right]^{\frac{(k+1)}{(k-1)}}} \quad (4.5)$$

The parameter c_d is, as described below, of particular interest: it is a correction coefficient that takes into account the physical limits of these equations. Despite the use of exact pressure and temperature conditions, the equations are not able to accurately recreate the physical phenomenon. For this reason the use of calibration parameters is of fundamental importance: these parameters must be suitably modified to ensure that the mass flow rate assessed by equations (4.4) and (4.5) is as close as possible to the experimental one in the same operating conditions

As regards the terms $\frac{dx_b}{dt}$ and $\frac{dQ_w}{dt}$ related respectively to the burning rate and to the heat exchange through the cylinder walls, they are described in greater detail in the paragraphs 4.2 e 4.3.

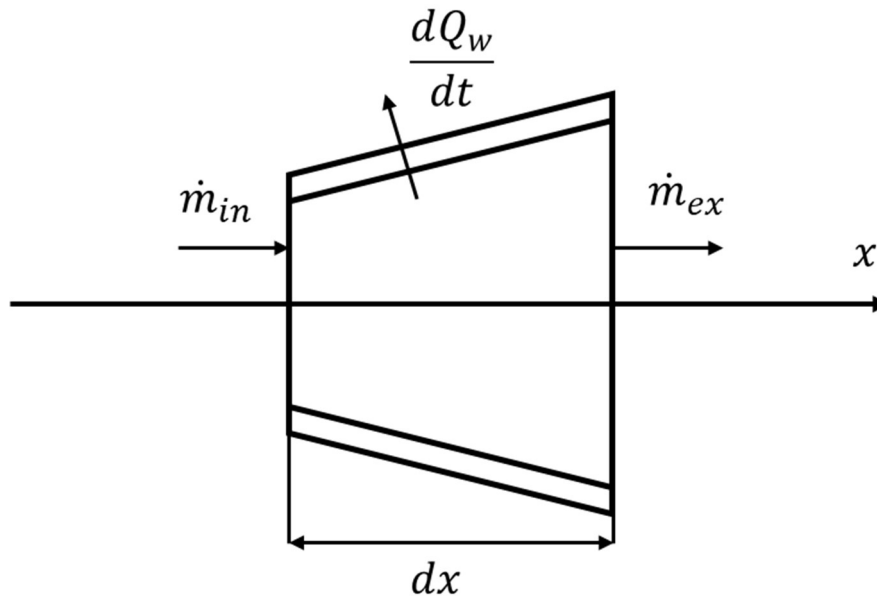


Figure 4.3 – 1D pipe schematization

The equations described so far refer to a 0-D approach, which, as mentioned, has been used to describe thermodynamic phenomena in volumes. As for the pipes, on the other hand, it is generally

preferred to use a 1-D approach because in a pipe one direction is predominant compared to the other two. The latter simplification carried out with respect to a 3-D approach does not affect the computational results. In addition, this approach, compared to the 0-D one, has the advantage of being able to describe the pressure waves that travel within the pipes: this is essential to be able to evaluate the correct filling of the cylinders and consequently to reproduce the behaviour of the engine. Generally, a control volume is not applied to the entire pipe. It is preferred to divide the pipe into many small sub-volumes and apply the 1-D equations to each sub-volume. *Figure 4.3* shows a schematization of a sub-volume. In each sub-volume the continuity equations, i.e. balance of mass, energy and momentum, are resolved.

$$\left\{ \begin{array}{l} \frac{\partial \rho}{\partial t} + \frac{\partial \rho}{\partial x} + \rho u \left(\frac{1}{\Omega} \frac{\partial \Omega}{\partial x} \right) = \frac{\partial \rho}{\partial t} + \frac{\partial \rho}{\partial x} + \rho u \alpha_A \\ \frac{\partial(\rho E)}{\partial t} + \frac{\partial \rho u H}{\partial x} + \rho u H \left(\frac{1}{\Omega} \frac{\partial \Omega}{\partial x} \right) = \frac{\partial(\rho E)}{\partial t} + \frac{\partial \rho u H}{\partial x} + \rho u H \alpha_A \\ \frac{\partial(\rho u)}{\partial t} + \frac{\partial(\rho u^2 + p)}{\partial x} + \rho u^2 \left(\frac{1}{\Omega} \frac{\partial \Omega}{\partial x} \right) = \frac{\partial(\rho u)}{\partial t} + \frac{\partial(\rho u^2 + p)}{\partial x} + \rho u^2 \alpha_A \end{array} \right. \quad (4.6)$$

The equations (4.6) can be represented in a more compact way, as expressed in (4.7) and (4.8), in which U represents the vector of the conservative variables, F is the flux vector and S characterizes the source term vector.

$$\frac{\partial U}{\partial t} + \frac{\partial F(U)}{\partial x} = S \quad (4.7)$$

$$U = \begin{bmatrix} \rho \\ \rho u \\ \rho E \\ \rho x_i \\ \rho x_{fuel} \end{bmatrix} \quad F = \begin{bmatrix} \rho u \\ \rho u^2 \\ \rho u H \\ \rho u x_i \\ \rho u x_{fuel} \end{bmatrix} \quad S = \begin{bmatrix} \rho u \alpha \\ \rho u^2 \left[\alpha + \left(2 \frac{f}{D} + \frac{C_p}{2L} \right) \frac{u}{|u|} \right] \\ \rho u H \alpha - 4 \frac{q}{D} \\ \rho u x_i \alpha \\ \rho u x_{fuel} \alpha \end{bmatrix} \quad (4.8)$$

The terms ρ , u , p , $E=c_v T+u^2/2$, $H=c_p T+u^2/2$ respectively represent the density, speed, pressure, total internal energy and total enthalpy per unit of mass. The flow model also includes sixteen equations describing the scalar transport of chemical species, i.e. the fuel, the air components and the residual components mass fractions.

These equations are represented by the subscript i ; these identify the chemical species involved in calculation, namely C, H, O, N, S, CO₂, H₂O, N₂, O₂, CO, H₂, OH, NO, Ar and SO₂; the fuel and the 15 species are accounted in the calculation by corresponding mass fraction term x_{fuel} and x_i , respectively. The source term S takes into account the effects of the section variations of the pipes ($\alpha=1/\Omega \cdot d\Omega/dt$), of the friction (f_a), which is estimated with the Poiseuille or Blasius formula as a function of the velocity inside the pipes, and of the fluid-wall heat exchange (q) evaluated as:

$$q = \frac{1}{2} \rho |u| f_a c_p (T_{wall} - T) \quad (4.9)$$

Where c_p is the specific heat at constant pressure, T is the gas temperature and T_{wall} is the wall temperature.

4.2. 0-D combustion and turbulence model

The term $\frac{dx_b}{dt}$ present in the equation (4.3) represents the burning rate of combustion. The phenomenon of the combustion that takes place within an ICE is an extremely complex process. Computational fluid dynamics is not able to provide accurate results on the thermodynamic and chemical state inside a cylinder during the combustion process. In a 0D/1D simulation model, this process is modelled through experimental data and/or empirical correlations whose complexity depends on the model adopted. Various combustion models for SI engines have been proposed since many years, trying to physically evaluate the burning rate, under the common hypothesis that the combustion is enhanced by the turbulence [45], [46], [47], [48]. The simplest approach to model the combustion process is to provide the trend of the heat release law for each cycle. It is possible to determine the heat released for each crank angle by knowing the total quantity of energy released. The latter can be determined using the quantity of fuel introduced for each cycle or the air/fuel ratio. Substantially, it is assumed that a certain amount of heat is supplied to the fluid contained in the cylinder from the outside; whereas, in reality, it is provided by the combustion of the mixture itself. One of the equations used to impose combustion is Wiebe's law [49]

$$x_b = 1 - e \left[-a \left(\frac{\vartheta - \vartheta_i}{\vartheta_f - \vartheta_i} \right)^m \right] \quad (4.10)$$

the fraction of burned mixture x_b is calculated as a function of the instantaneous crank angle ϑ and the angles of start and end of combustion, indicated as ϑ_i and ϑ_f , which are imposed. The constants a and m depend on the geometric shape of the chamber and the efficiency of combustion; a is defined as the "efficiency parameter" and measures the completeness of the process, while m is called the "chamber factor" and influences the combustion speed.

The relative amount of heat released can be obtained from the instantaneous fraction of the burned mixture $\frac{dx_b}{dt}$. In *Figure 4.4* a generic trend of the Wiebe heat release law is shown, representing both the fraction of burnt mass and the burning rate.

The Wiebe model does not consider the physics of the combustion and injection system of the mixture and therefore requires a considerable effort to set up before it can be used with a sufficient confidence.

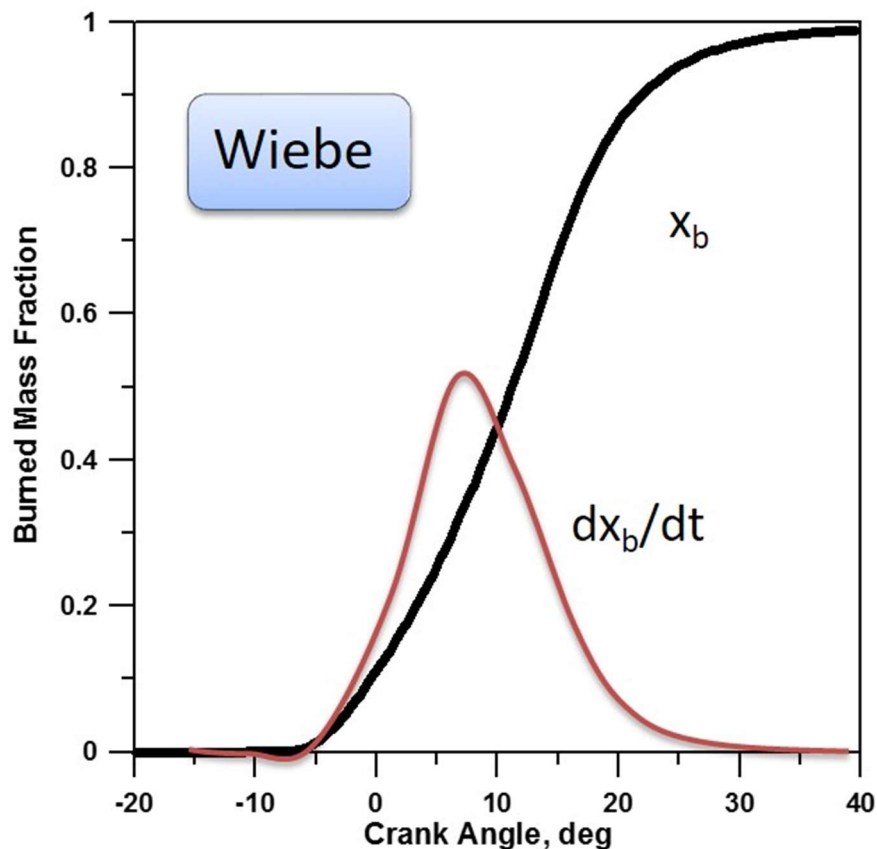


Figure 4.4 – Wiebe heat release law trend

As said, using Wiebe's correlation, combustion is imposed and is not predicted. A step towards a more detailed physical description is the use of a multi-zone approach applied to the combustion

chamber [50]. The schematic view of the cylinder in *Figure 4.2* it is modified as the one shown with closed valves in the *Figure 4.5*.

The combustion chamber is divided into two areas: an area in which there is the mixture not yet combusted (unburned) and an area in which there are the burned gases. The temperature and pressure are uniform within each individual area.

The mass passage between the unburned and the burned zone represents the combustion speed and is unknown. One of the most important aspects of the combustion phenomenon is undoubtedly turbulence. There are various approaches to assessing the term $\frac{dm_b}{dt}$ by taking into account the phenomenon of turbulence.

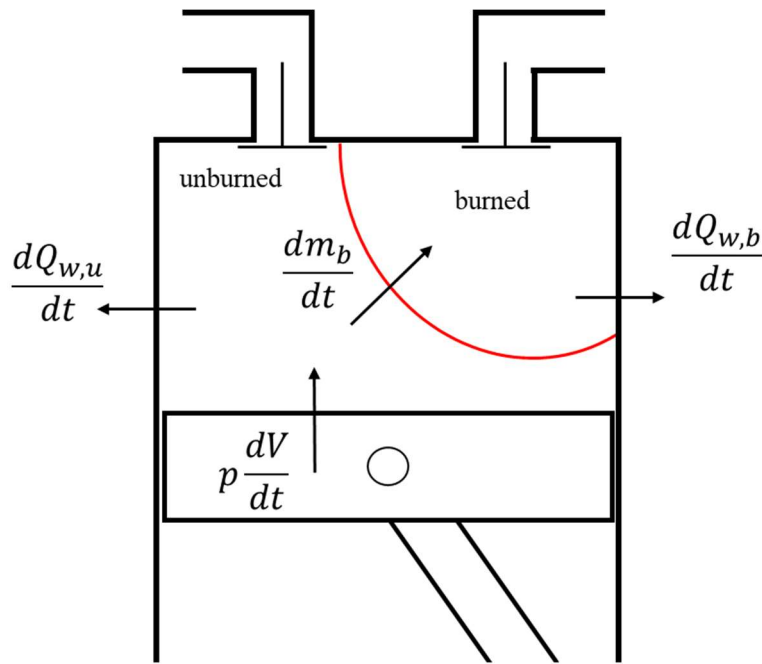


Figure 4.5 – 0D cylinder schematization with 2-zone approach

In this work, a turbulent combustion model considering the influence of cylinder's geometry, spark timing, air motion, valve timing and fuel properties has been adopted to predict the flame front propagation. This model, applicable to homogeneous charge spark-ignition engines, is based on the results reported in [51], [52], [53]. The flame front is assumed to be non-corrugated, of non-infinitesimal thickness, which propagates at the speed $S_L + S_T$ according to scheme in *Figure 4.6*.

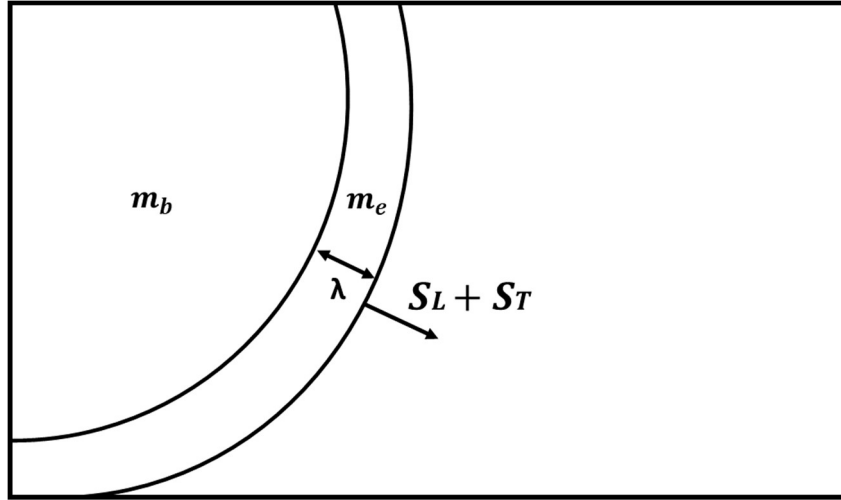


Figure 4.6 - Schematic representation of the model adopted for the turbulent combustion

According to the model, the encapsulation rate is calculated as follows:

$$\left(\frac{dm_e}{dt}\right) = \rho_u A_L (S_T + S_L) \quad (4.11)$$

where ρ_u is the density of the unburned mixture, A_L is the surface of discontinuity between burned and unburned gases, S_T and S_L are the turbulent and laminar flame speed. The burn rate is defined as follows:

$$\left(\frac{dm_b}{dt}\right) = \frac{m_e - m_b}{\tau} \quad (4.12)$$

where m_e is the encapsulated mass, m_b is the burned mass, τ is the chemical reaction time (reaction zone crossing time) expressed as $\tau = \frac{\lambda_T}{S_L}$ in which λ_T is the Taylor microscale and S_L is the laminar flame speed. This model includes three calibration parameters. The first, here called C_1 , is used to modify the flame kernel growth rate. This parameter influences the ignition delay by changing the size of the discontinuity surface between burned and unburned gases according to the relation:

$$A_{LC} = C_1 A_L \quad (4.13)$$

A higher value decreases the ignition delay, advancing the transition from laminar to turbulent combustion. The second multiplier, here called C_2 , is used to scale the calculated turbulent flame

speed. This constant affects the overall duration of combustion. Higher values increase the combustion speed by changing the turbulent speed according to the relation:

$$S_{Tc} = C_2 S_T \quad (4.14)$$

The third multiplier, called C_3 , is used to modify the Taylor Length Scale. The Taylor microscale modifies the combustion time constant of the fuel-air mixture entrained in the flame zone. C_3 mainly affects the tail combustion according to the following relation:

$$\tau_c = C_3 \tau. \quad (4.15)$$

As concerned the turbulence model, a 0-D turbulence approach is adopted. In 0D combustion models turbulence models are used which follow either a K - k energy cascade approach [54], where K is the mean kinetic energy and k is the turbulent kinetic energy, or a k - ε approach [55], where ε is the dissipation rate.

Two differential equations model the mean kinetic energy K and turbulent kinetic energy k . The turbulence dissipation rate ε and integral length scale L_t are modeled using algebraic equations.

In the k - ε approach [55] two differential equations model respectively the turbulent kinetic energy k and its dissipation rate ε . The mean kinetic energy K is taken into account in the turbulent kinetic energy equation through source terms (representing intake flow, turbulence production via shear, etc), while the integral length scale of turbulence is obtained as an output of the two equations via the equation:

$$L_t = \frac{0.164 \cdot k^{\frac{3}{2}}}{\varepsilon} \quad (4.16)$$

The 0-D turbulence model used in this Thesis adopts both the K - k and the k - ε methodologies. A K - k - ε energy cascade approach is used. Four differential equations are solved, one each for the evolution of K , k , ε and tumble. K equation is based on the work done by Poulos et al. [56]

$$\frac{dK}{dt} = \frac{1}{2} \dot{m}_i \cdot V_i^2 - P - K \frac{\dot{m}_e}{m} \quad (4.17)$$

Where m is the mass in the cylinder, \dot{m}_i and \dot{m}_e are respectively the air mass flow rate into the cylinder and out of the cylinder, P is the rate of the turbulent kinetic energy dissipation and V_i is the jet velocity into the cylinder.

The k and ε equations are based on the work done by Morel et al. [57].

$$\rho \frac{dk}{dt} = -\frac{2}{3} \rho \cdot k \cdot D \quad (4.18)$$

$$\frac{d\varepsilon}{dt} = \left(-\frac{2}{3} C_1 + 1 \right) \rho \cdot \varepsilon \cdot D \quad (4.19)$$

Where ρ is the density, D is the velocity divergence and C_1 is a constant. Additional generation of turbulence owing to compressibility effects [23] are also accounted for in this model.

4.3. Thermal exchange model

The Woschni [58], the Hohenberg [59] and the Annand [60] correlations are widely adopted for ICE simulation. In this work, the heat exchange within the cylinder is based on the Woschni model, which provides an estimation for the convective heat transfer coefficient h_w as follows:

$$h_w = F_w D^{m-0.2} p^m c_w^m T^{0.75-1.62m} \quad (4.20)$$

where F_w is the calibration coefficient of the heat exchanges, D is the cylinder bore, c_w is the equivalent velocity of the fluid, p is the pressure, T the temperature and m a characteristic exponent. A calibration parameter called C_4 has been defined to tune the heat exchanged by multiplying the heat transfer coefficient h_w :

$$h_{wc} = C_4 h_w \quad (4.21)$$

The thermal power exchanged can be then evaluated through the fundamental equation:

$$\dot{Q}_w = h_{wc} A_w (T - T_w) \quad (4.22)$$

4.4. Valve model

The pressure drops in the intake system have been reliably estimate, a multiplier C_5 that has been defined to correct the forward flow coefficient through the intake valves as follows:

$$c_{dc} = C_5 c_{dw} \quad (4.23)$$

where c_{dw} is forward flow coefficient obtained from flow tests on the cylinder head. In this way, pressure drops through the intake system are calibrated using a single multiplier which affects the mass flow through the valves according to the following equations for subsonic and supersonic flow, respectively:

$$\frac{dm}{dt} = c_{dc} A_{ref,v} p_1 \sqrt{\frac{2\gamma}{\gamma-1} \frac{1}{RT_1} \left[\left(\frac{p_2}{p_1}\right)^{2/\gamma} - \left(\frac{p_2}{p_1}\right)^{\gamma+1/\gamma} \right]} \quad (4.24)$$

$$\frac{dm}{dt} = c_{dc} A_{ref,v} p_1 \sqrt{\frac{\gamma}{RT_1} \left(\frac{2}{\gamma+1}\right)^{(\gamma+1)/(\gamma-1)}} \quad (4.25)$$

where $\frac{dm}{dt}$ is the mass flow rate, c_{dc} is the flow coefficient, $A_{ref,v}$ is the valve reference area, p_1 the valve upstream pressure, γ the adiabatic expansion coefficient, R the characteristic constant of the gas type and T_1 the valves upstream temperature.

4.5. Friction model

The friction model is essential to reliably estimate the engine performance. It accounts for all the friction losses and the power required by the engine's auxiliary systems, thus affecting most of the main engine parameters like mean effective pressure, brake torque and other correlated quantities. The Chen-Flynn model [61] has been adopted in this study, which is a semi-empirical relation and allows to estimate the friction mean effective pressure according to the following formulation:

$$fmep = a + b \cdot p_{max} + c \cdot v_{mean_piston} + d \cdot v_{mean_piston}^2 \quad (4.26)$$

where a , b , c and d are calibration constants, p_{max} is the maximum cylinder pressure that gives a measure of the engine load, and v_{mean_piston} is the mean piston speed. Friction mean effective pressure is usually estimated from the available experimental data as the difference between indicated mean effective pressure ($imep$) and brake mean effective pressure ($bmep$).

This parameter intervenes during the calculation of some fundamental quantities of the engine, for example $imep$, torque, power and all other quantities directly connected.

After determining the pressure trend in the cylinder, the software calculates the work indicated by the integrated circuit:

$$L_i = \oint p \, dv \quad (4.27)$$

Consequently, it is possible to know the Net Indicated Mean Effective Pressure ($imep_n$):

$$imep_n = \frac{L_i}{displacement} \quad (4.28)$$

$imep_n$ can be considered as that hypothetical differential pressure which, acting constantly during a single stroke of the piston, is able to provide the same work as the variable pressure cycle.

It is possible to obtain the net torque at the rotation axis, or the currently available at the engine output, by taking into account the torque necessary to overcome the mechanical friction between the moving parts and auxiliaries torque request, or:

$$ibmep = imep_n - fmep \quad (4.29)$$

or:

$$bmep = imep \cdot \eta_m \quad (4.30)$$

where η_m is the mechanical efficiency.

4.6. PID controller model

In order to develop an experimental campaign like the one described in *paragraph 1.4* and to best recreate the behavior of the internal combustion engine during the experimental tests have been used continuous proportional-integral-derivative (PID) controller. PID controllers are used to reach certain target values of quantities sensitive to some variables that can be used as input of the controller. They are used for a wide variety of different applications.

For example, as shown in *Figure 4.7*, a PID controller can be used to reach a pressure target p downstream of a throttle valve by controlling the opening angle of the α valve.

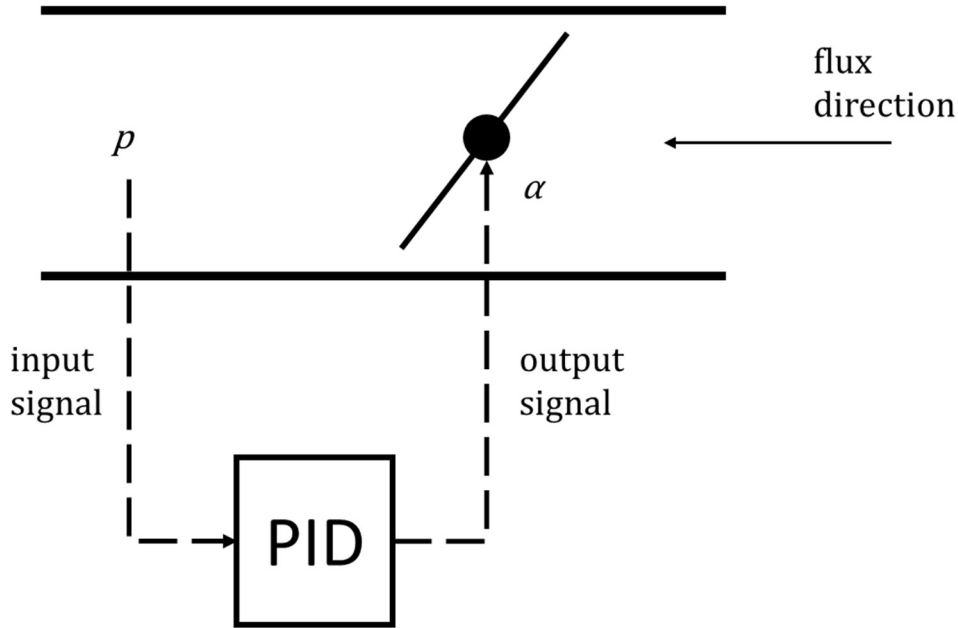


Figure 4.7 – schematization of the PID controller operation

The controller receives as input signal the pressure p downstream of the throttle valve and opens it in order to reach the target pressure value set by the user. The PID controller solves the following equations:

$$\frac{dx_1}{dt} = r \quad (4.31)$$

$$\frac{dx_2}{dt} = \frac{r - x_2}{T} \quad (4.32)$$

$$y = \left(K_p + \frac{K_d}{T} \right) r + K_i \cdot x_1 - \frac{K_d}{T} \cdot x_2 \quad (4.33)$$

where K_p is the Proportional Gain, K_i is the Integral Gain, K_d is the Derivative Gain, T is the Derivative Time Constant, y is the controller output, r is the difference between the Reference Signal value and the input signal value, and x_1 and x_2 are the state variables. If the initial input signal value is known, the user can control the initial output value using the State 1 and State 2 Initial Value attributes. The proportional term will produce a large controlling action in response to a large error. The integral term will produce a large controlling action output if the error has been accumulating over time. The derivative term will produce a great controlling action in response to a large change in error.

The PID controllers have great flexibility but their tuning is quite complex. In fact, suitable gains (see attributes below) have to be found for each operative scenario. Furthermore, sometimes a

"schedule" of gains is required so that the controller works well at each working condition. For example, a set of gains works well at 2000 RPM whereas it is no longer good at 5000 RPM.

5. Engine description and optimization

The second methodology, which is used to reduce the costs of carrying out the engine base calibration process and described extensively in chapter 6, is based on the use of a validated 0D-1D model of an engine. In this chapter, in addition to a description of the engine used architecture and its 0D-1D modeling, the robust validation of the model using a multi-variable multi-objective validation process, which represents one of the fundamental aspects to achieve the above mentioned purposes, is described. The use of a thermo-fluid-dynamic model of the engine that is capable of recreating the operation of the real engine throughout its operating range with a relatively low error is essential. The datasheets obtained virtually from the model, if they have a low error compared to the real ones, can be used as input in the computer aided calibration.

5.1. Engine architecture

An internal combustion reciprocating engine is a thermal engine that has the purpose of producing mechanical power from the chemical energy contained in a fuel [62]. Combustion is an exothermic chemical reaction that involves oxidation of a fuel by a comburent (generally oxygen present in the air). This phenomenon generates a strong increase in pressure and temperature of the working fluid inside the combustion chamber. The pressure generated determines a thrust on the piston which is converted into a rotation movement of the crankshaft through a connecting rod-crank mechanism.

Although the reciprocating engine has been designed at the end of the 19th century and it is thought that its technological and evolutionary limit has been reached, the evolution of the engine is still in progress with increasingly complex architectures, components and strategies.

One of the branches of this evolution is undoubtedly that related to the development of numerical simulation models of the engine that allow to obtain certain advantages. In fact, simulation models accompany the entire design phase of an engine and can have various purposes:

- to investigate whether any changes lead to improvements in terms of performance, or a reduction in consumption, or a reduction in emissions.
- To try to describe complicated phenomena to be studied with experimental tests, such as combustion inside a pre-chamber [63].
- Use of fast-running models in processes such as hardware in the loop or software in the loop.

In this way, hours and hours of experimental tests can be avoided.

In this Thesis work, as explained in greater detail in chapter 6, an innovative use of the simulation models is made: the properly validated numerical engine model replaces the real engine in the base calibration process, virtually carrying out experimental tests otherwise carried out on the bench test.





Table 5.1 – main characteristics of the engine used for the 0D-1D modelling






Engine model	0.9 1 85 CV Turbocharged
Number of cylinders, layout	2 in line
Total displacement [cm³]	875
Valves per cylinder	4
European emission standard	EURO5
Max power CE [kW (CV) @ RPM]	62 (85) @ 5500
Max torque CE [Nm (kg·m) @ RPM]	145 (14.8) @ 2000
Bore [mm]	80.5
Stroke [mm]	86
Connecting Rod Length [mm]	136.85
Compression Ratio	9.9
TDC Clearance Height [mm]	9.3

The modeled engine has the characteristics shown in *Table 5.1*. It is a two-cylinder indirect injection gasoline engine with a total displacement of 875 cm³, with 4 valves per cylinder, 2 intake and 2 exhaust valves. The valves are equipped with a variable actuation system. The engine is turbocharged and can deliver a maximum power of 62 kW at 5500 rpm. The engine is equipped on segment B cars and complies with EURO 5 anti-polluting regulations.

5.2. Engine modelling

Figure 5.1 shows the schematization of the engine model. The modeling starts from the intake pipe and ends with the upstream exhaust pipe of the after-treatment system. In particular:

-  represents the external environment related to suction,
-  represents the external environment related to the discharge. As will be seen later, an equation has been used to recreate the phenomenon of exhaust back pressure,
-  indicates the filter that has been schematized as a volume which causes a pressure drop,
-  represents schematization of the throttle valve,

-  represents the cylinders,
-  and  respectively represent the compressor and the turbine,
-  represents the intake and exhaust valves,
-  represents the injectors.

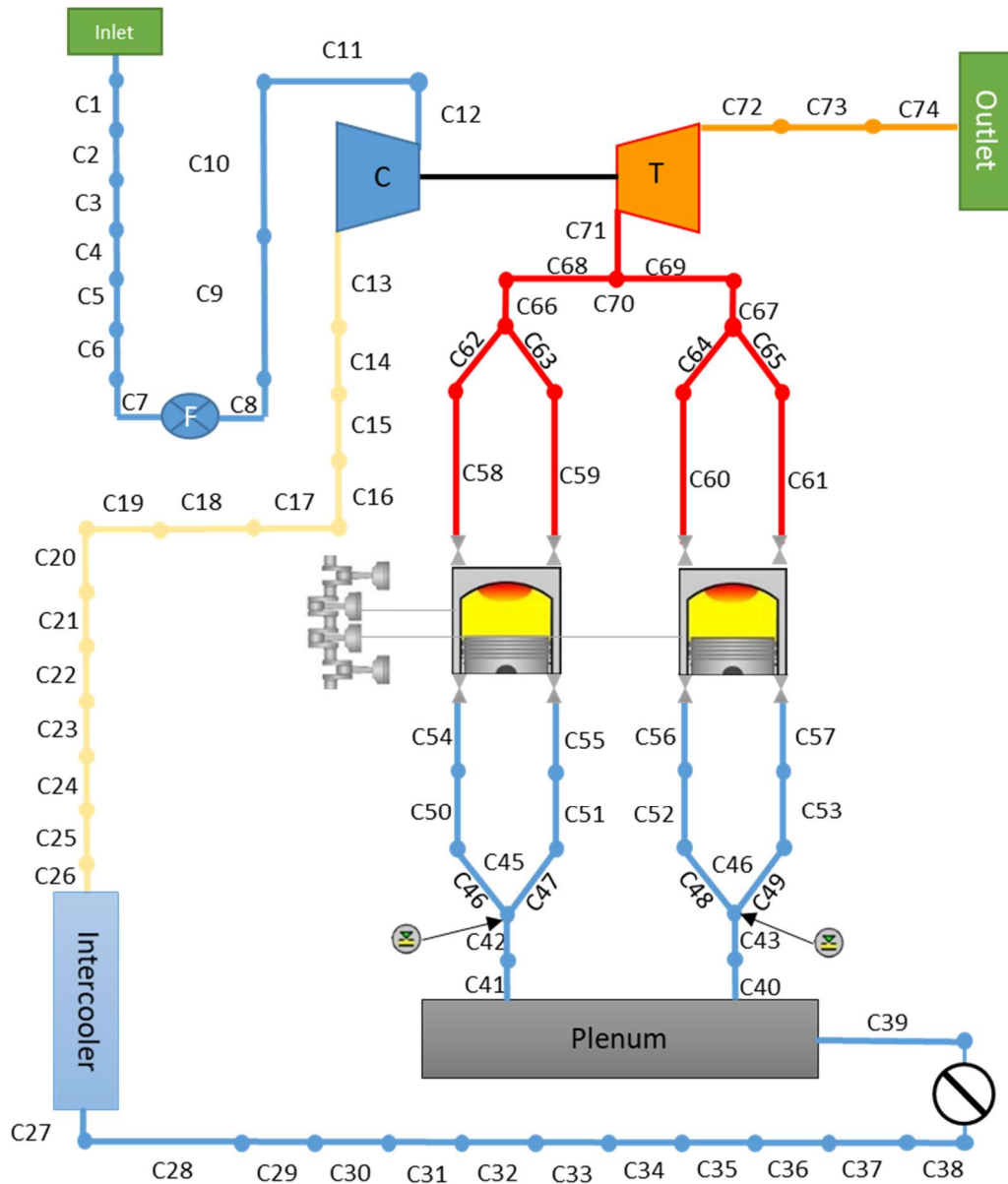


Figure 5.1 – 0D-1D engine schematization

From the geometric point of view, the intake and exhaust pipes have been schematized with a 0-D and 1-D approach. The intake and exhaust pipes have been divided into shorter pipes (pipes and

volumes) as represented in the figure by the elements named from C1 to C74, whose geometric characteristics are represented in the *Table 5.2* as for the pipes and *Table 5.3* as for the volumes.

Table 5.2 - geometrical characteristics of the pipes used in the model

	Φ [mm]		Length [mm]	Bend
	in	out		
C1	64.33	45.99	30	
C2	46	46	55	80
C3	46	46	159	
C4	46	47	78	51
C5	47.33	54.21	70	
C6	54.21	60.84	84.7	63
C7	60.84	62	40	
C8	68	66.7	48	
C9	66.7	50.4	134.4	68r
C10	50.4	46.5	40	
C11	46.5	42	71	58r
C12	42	41.7	64.1	
C13	23	23	16.7	
C14	23	23	28.1	40r
C15	23	23	65.7	
C16	23	23	17.8	40r
C17	23	23	40.6	
C18	23	33	23.9	
C19	33	34	34.5	
C20	34	34	36.7	60r
C21	34	34	34.3	
C22	34	34	41.3	60r
C23	34	34	36	
C24	34	37.5	36	60r
C25	37.5	37.5	53.4	
C28	38.5	38.5	48.5	
C29	38.5	38.5	76.6	75r
C30	38.5	46	43.5	
C31	46	46	67.1	
C32	46	46	23.9	45r
C33	46	46	88.8	
C34	46	46	28.8	50r
C35	46	46	102	
C36	46	46	75.5	45r
C37	46	62	32.4	
C38	58	57.5	19	
C39	57.5	60	19	
C40-41	42.02	41.26	34	10000R
C42-43	41.26	38.96	151.3	98.5
C46-47-48-49	26.64	24.22	25	10000R
C50-51-52-53	24.22	24.01	10	25A
C54-55-56-57	24.01	26	6.8	26A
C58	21.84	22.26	38	29.9R
C59-60-61	21.84	22.26	38	73.8A

C62-63-64-65	22.26	21.04	18	
C68-69	32.08	32.08	60.5	22A
C71	36.5	36.5	60.5	
C72	54.98	63.87	120	90A
C73	63.87	66.89	72.5	15A
C74	66.89	94.31	85	20A

Table 5.3 – sizes of volumes used in the engine model

	Volume [mm³]
C26-27	302619
C44-45	29916
C66-67	14576
C70	43191

A wall temperature of 295K in the intake pipes and volumes has been imposed, while a temperature of 773K has been imposed on the walls of the exhaust pipes to evaluate the heat exchange according to the equation (4.22).

The conditions of the intake external environment have been imposed with a pressure equal to 1 bar and a temperature close to 295 K. A temperature equal to 773 K has been imposed on the exhaust, while a pressure directly proportional to the air mass flow rate has been imposed to try to recreate the effect of the exhaust back pressure.

The intake filter has been schematized as two 1.8 l volumes each divided by an orifice that causes a small pressure drop. The intercooler has been schematized as a set of small pipes with a square section that form a tube bundle: each pipe has a length of 63.3 mm and a height, equal to the width, of 7.28 mm. The wall temperature is set at 321 K. The intake plenum has been schematized as a volume of 1.52 l. The injectors have been schematized with sequential injector models, which, once the fuel ratio value has been set, determine the fuel flow rate to be injected depending on the air mass flow rate in the runner.

The turbo-compressor has been schematized with map models in which the values of the following variables are imposed: the corrected rotation speed, the correct mass flow, the pressure ratio and the efficiency regarding the compressor, the reduced rotation speed, the reduced mass flow, the pressure ratio and the efficiency of the turbine.

As anticipated, the engine is characterized by the presence of two cylinders whose cycles are 360° out of phase. Each cylinder has been modeled by inserting some geometric characteristics concerning the connecting rod-crank system, the piston and the combustion chamber.

The geometric characteristics of the piston-connecting rod-crank system are listed in *Table 5.1* in accordance with the schematic representation in *Figure 5.2*.

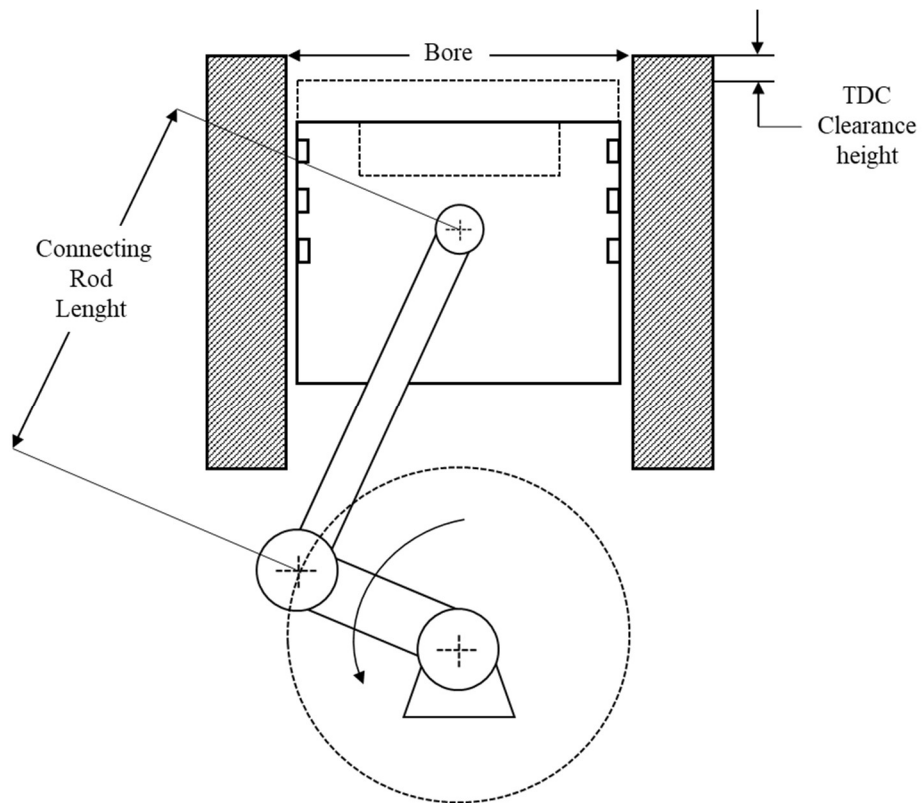


Figure 5.2 – schematization of the piston-rod-crank mechanism

It can be noted the piston is characterized by a simple geometry presenting a flat head cup. The geometric characteristics of the piston cup and dome are shown in the *Table 5.4* according to the scheme in *Figure 5.3*, which shows that the dome is hemispherical

Table 5.4 - geometrical characteristics of the combustion chamber

Piston Cup Diameter [mm]	70
Piston Cup Depth [mm]	2.68
Dome Diameter [mm]	75
Dome Height [mm]	12

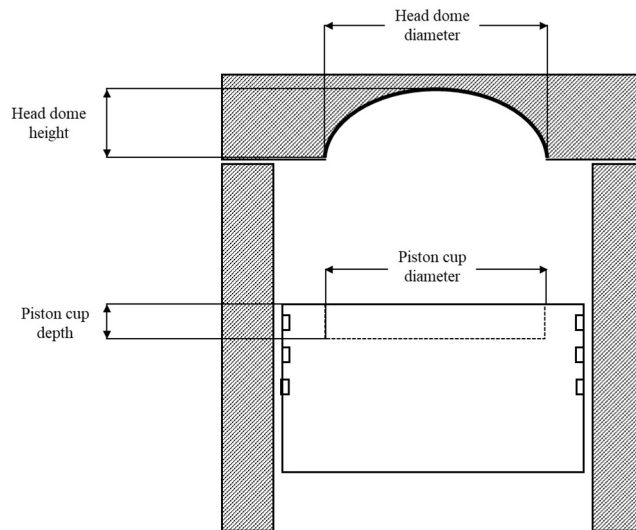


Figure 5.3 - schematization of the combustion chamber

5.3. Optimization – MOGA

Once the engine schematization has been completed, a first comparison has been made between some experimental quantities of the real engine and the quantities obtained from the model in 16 different operating conditions. A preliminary heuristic model validation has been made to carry out this comparison.

Table 5.5 – operating conditions used for the validation

RPM	LAMBDA	Spark advance	Manifol pressure	Throttle angle
[rpm]		[°ATDC]	[mbar]	[°]
5500	0.738	5.9	1909	81.92
5101	0.74	2.9	2050	81.7
4804	0.732	1.5	2172	81.94
4398	0.728	0	2294	81.94
4003	0.73	-1.8	2346	81.94
3602	0.736	-3.3	2335	81.95
3301	0.773	-2.8	2312	81.94
3099	0.791	-4.3	2297	81.94
3000	0.8	-5	2275	81.94
2704	0.798	-7.8	2259	81.94
2505	0.829	-9.2	2238	81.94
2506	0.828	-9.1	2239	81.94
2303	0.864	-9.6	2229	81.94
2099	0.885	-9.8	2195	81.94
1798	0.911	-12.2	2139	81.94
1492	0.984	-12.3	1728	79.99

The 16 engine operating points used for comparison are in full load conditions and are described in *Table 5.5*. In particular: the throttle valve is completely open (WOT condition), the spark advance (s.a.) is set in order to have the maximum torque, the λ is less than the unit as a rich mixture avoids the risk of detonation at high loads, the intake valves, which are equipped with VVA, perform the maximum lift. As regards the s.a., the table shows the values of degrees after the top dead center; therefore, a negative value indicates how many degrees before the top dead center the s.a. occurs.

Figure 5.4 shows the trend of six quantities that will be used for subsequent validation:

- Torque [Nm]
- Break specific fuel consumption (BSFC) [g/kWh]
- Air mass flow rate [kg/h]
- Turbine speed [rpm]
- Maximum pressure [bar]
- Crank angle at maximum pressure [°ATDC]

In particular, the black curves represent the trends of the experimental quantities obtained on the test bench under the operating conditions described in *Table 5.5*, while the red curves represent the quantities obtained from the numerical model in the same operating conditions.

Table 5.6 - error reached by a comparison between experimental data and numerical quantities using a heuristic validation

	Torque	BSFC	Air mass flow rate	Turbo Speed	Max pressure	Angle@ Max Pressure
Mean error %	9.5	6.3	6.6	2.3	5.4	7.9
Total Mean error %	6.6					
Max Error %	16.7 Torque @ 5500rpm					

Table 5.6 reports mean error $\bar{e}_{\%,i}$ evaluated as:

$$\bar{e}_{\%,i} = \sum_{j=1}^n \frac{(Q_{j,mod} - Q_{j,exp})}{Q_{j,exp}} \cdot \frac{100}{n} \quad (5.1)$$

where $Q_{j,exp}$ is the j-th experimental quantity, $Q_{j,mod}$ is the j-th quantity evaluated by the 1D engine model, n is the number of operating conditions. It can be noted that the total mean error is very high and above 6.5% with a maximum value of 16.68% relative to the torque at 5500rpm.

Table 5.7 - error achieved by a comparison between experimental data and numerical quantities using a heuristic calibration at 3000 rpm

	Experimental	Numerical	Error %
Torque [Nm]	143.4	158.8	10.7
Max cylinder pressure [bar]	68.3	73.1	7.1
Max pressure angle [deg ATDC]	38.3	35.2	8
Air mass flow rate [kg/h]	193.4	195.6	1.1
BSFC [g/kWh]	369	335	9.1
Boost pressure [bar]	2.3	2.4	3.5
Mean error			6.6

Table 5.7 reports a comparison in terms of single error e_j at 3000 rpm. The error has been evaluated as:

$$e_j = \frac{(Q_{j,mod} - Q_{j,exp})}{Q_{j,exp}} \cdot 100 \quad (5.2)$$

Again, a high percentage error greater than 6.5% can be noted, with a maximum error of 10.75% relative to the torque. The mean total error achieved is too high: in fact, the idea of reproducing with numerical models extensive experimental campaigns can only be realized when the numerical model manages to reproduce the physical phenomenon with good accuracy and precision in the whole operating range of the engine. Therefore, a more robust validation of the model is necessary. The discrepancy between the numerical model and the real engine is due to several factors involved in these analyses: possible errors in the experimental measurements, approximate physical models used in the 0D-1D modeling, experience of the model maker and so on. These approximations define ignorance of the model which traditionally is reduced manually by the model maker.

It is considered necessary to remove the human component from this process and introduce an automated one capable of reducing the times and costs of this process in order to carry out a useful procedure on an industrial level. For this automated method, a multi-variable-multi-objective validation process has been chosen that allows to calibrate the model variables automatically. Before proceeding with the automated validation, two parameters which are fundamental for the operation of the engine model have been individually calibrated: the model that evaluates the friction due to the interaction of the moving parts of the engine (friction between the cylinder, piston, connecting rod, crank etc.) and the throttle valve model.

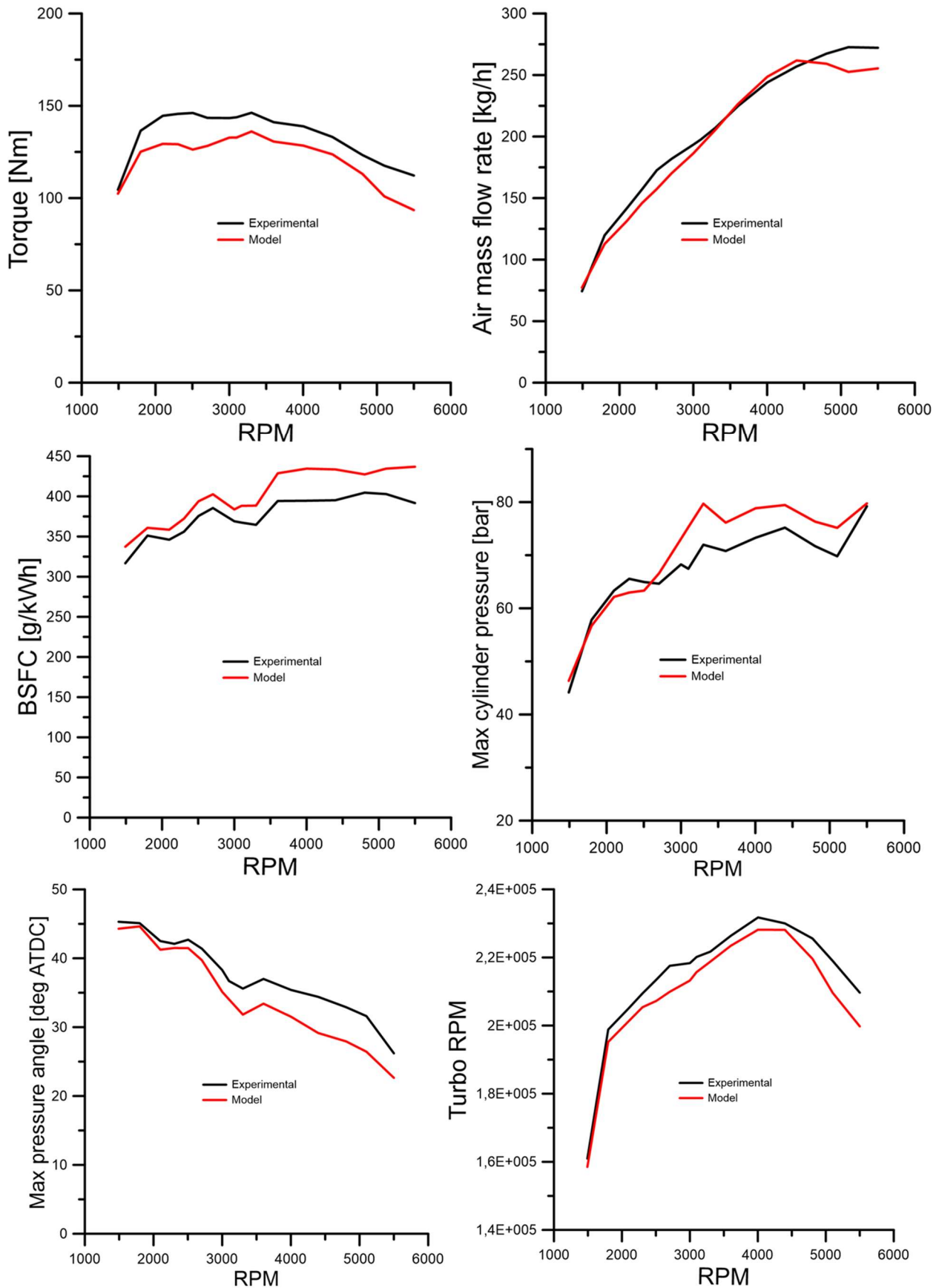


Figure 5.4 - comparison between trends of some experimental quantities (in black) and those obtained from the model (in red)

5.3.1. Calibration of the friction model

This parameter is essential for the correct operation of the model because it allows to take into account all the losses related to friction and the actuation of the auxiliaries. Among the semi-empirical relationships available in the literature, the Chen-Flynn friction model certainly plays a fundamental role, which provides a report for the calculation of the f_{mep} .

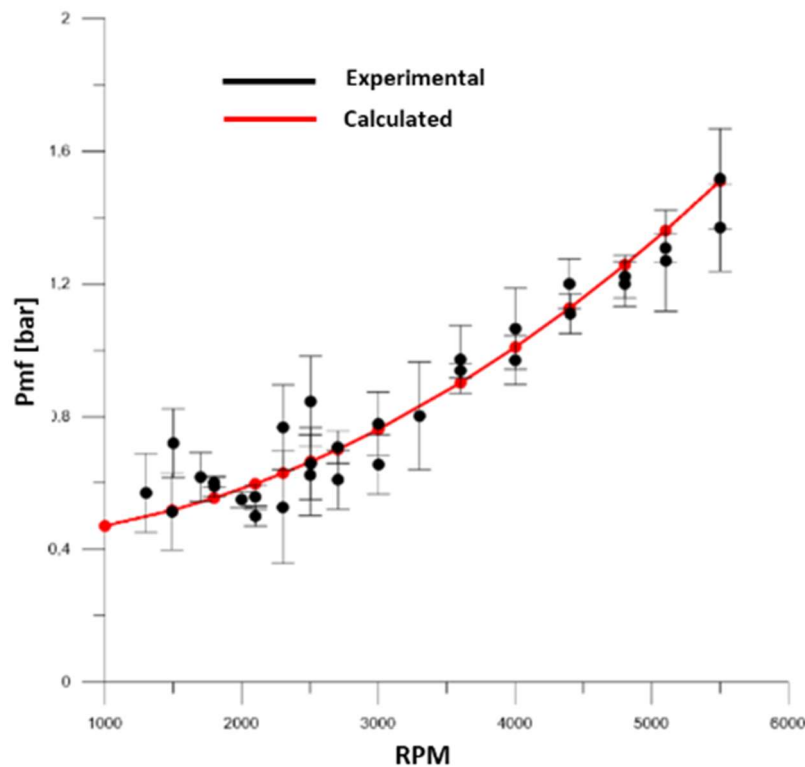


Figure 5.5 - Calibration achieved for the Chen-Flynn model.

The equation used in the model is presented in (4.26). It is quadratically sensitive with the engine speed and linearly with the maximum pressure inside the cylinder and the engine speed. The calibration of this equation has been carried out by modifying parameters a , b , c and d so that the f_{mep} evaluated by the equation is very close to the experimental one in the same operating conditions. For the calibration, the 16 operating conditions described in Table 5.5 have been chosen so as not to affect the number of experimental tests to be performed.

Table 5.8 – Calibration parameters values achieved for the Chen-Flynn model

a	b	c	D
0,43	0,00005	0,002	0,0042

Table 5.8 shows the values of the model calibration parameters reached at the end of the automatic calibration, while Figure 5.5 shows the comparison between experimental f_{mep} data and those obtained from the *Chen-Flynn* model using these parameters.

It can be noted that the model manages to faithfully recreate the f_{mep} trend, also considering that this experimental quantity is affected by a high uncertainty due to the difficulty with which it is assessed.

5.3.2. Calibration of the throttle model

Pressure drops across intake and exhaust systems have high influence on the fresh charge replacement process. Among them, pressure drops across the throttle valve widely affect the volumetric efficiency. However, they are characterized by great uncertainties and need proper calibration. As known, the angular position of the throttle is adjusted to ensure the desired engine power. Therefore, a pressure drop is induced downstream of the valve with the consequent regulation of the air mass flowing to the cylinders. As schematized in Figure 5.6, the throttle valve is modelled as an orifice with variable section and the air mass flow rate of the downstream flow is evaluated through the following equation:

$$\dot{m}_r = c_D A_{ref} \rho_{ref} U_{ref} \quad (5.3)$$

where A_{ref} is a constant reference section (i.e. the cross section at wide open throttle in this study), ρ_{ref} and U_{ref} are the density and the reference speed of the induced air at ambient conditions, respectively; c_D is the flow coefficient, which is a function of the angular position of the throttle valve and is given by the ratio between actual and the reference value of the theoretical mass flow rate:

$$c_D = \frac{\dot{m}_r}{\dot{m}_{ref}} \quad (5.4)$$

where:

$$\dot{m}_{ref} = A_{ref} \rho_{ref} U_{ref} \quad (5.5)$$

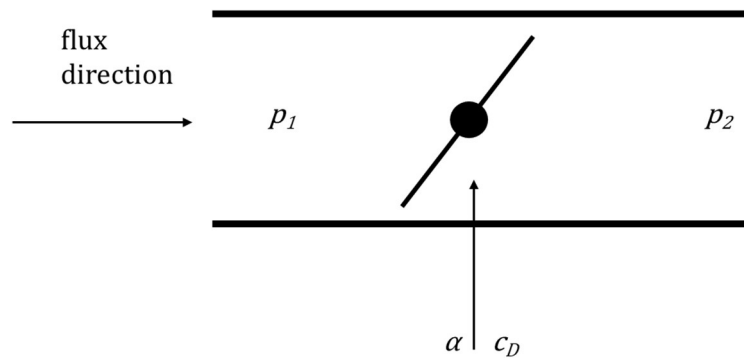


Figure 5.6 – schematization of the throttle model

This coefficient must therefore be calibrated to match the experimental data, so that at a certain throttle angle, the air mass flow rate calculated by the model is as close as possible to the measured mass flow rate at the same opening conditions. Therefore, this coefficient provides a description of the throttle behaviour.

Table 5.9 – operating conditions used for the calibration of the throttle model

RPM	Throttle angle	Air mass flow rate	Upstream pressure	Downstream pressure
-	[deg]	[kg/h]	[mbar]	[mbar]
1200	1.2	6.7	1014	403
1500	3.2	16.2	1015	612
2000	5.1	27.8	1018	714
2500	8.1	43.1	1033	820
4400	10.2	68.9	1063	739
3300	15.1	71.6	1066	954
5100	20.7	131.9	1209	1093
5500	25.2	159.6	1293	1192
5900	30.9	204.4	1402	1305
2700	34.5	66.4	1065	1021
2000	42.9	46.5	1037	1016
4400	54.7	120.4	1162	1131
4800	60.1	136.3	1202	1170
3300	70.5	85.5	1096	1067
1800	81.9	41.8	1031	1019

The throttle model has been calibrated using 15 experimental conditions that were available and collected in the *Table 5.9*, characterized by the air mass flow at the valve inlet, the opening angle of the throttle valve (α in the scheme in *Figure 5.6*) and the pressure upstream and downstream of the valve (p_1 e p_2 in the scheme in *Figure 5.6*).

According to *Figure 5.6*, the model has been calibrated individually with respect to the complete engine model, following these steps:

- The environment conditions upstream of the valve, pressure, temperature and composition have been imposed
- The environment conditions downstream of the valve, pressure, temperature and composition have been imposed
- The throttle valve opening angles are set
- For each valve opening angle, the parameter c_D has been adjusted so that the values of air mass flow rate and Δp between upstream and downstream of the valve calculated by the model are as close as possible to the real ones listed in *Table 5.9*.

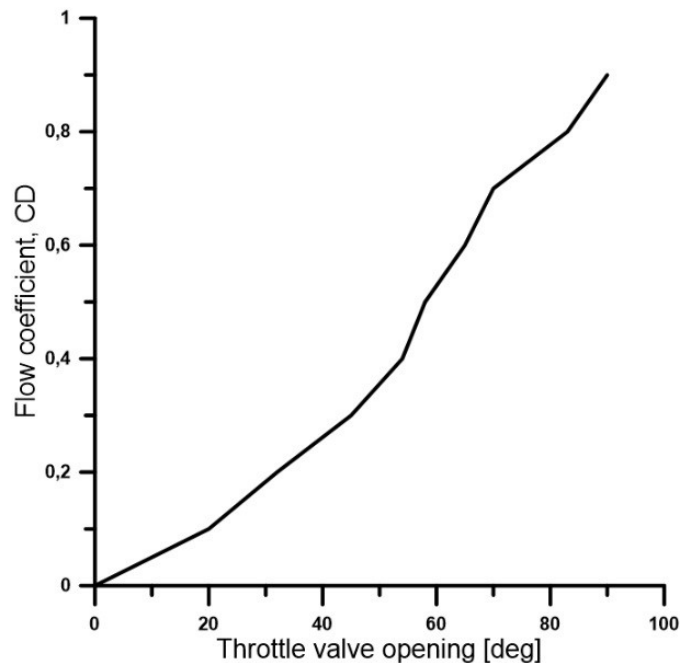


Figure 5.7 - values of c_D vs the opening angle of the throttle valve obtained at the end of the calibration

Figure 5.7 shows the values of c_D vs the opening angle of the throttle valve α obtained with this calibration.

5.3.3. General multi-variable multi-objective methodology applied to the engine model: MOGA

In the last years, the use of evolutionary multi-objective optimization algorithms has become increasingly important in the field of optimization processes. In particular, it has been demonstrated

how evolutionary genetic algorithm can be effectively adopted to solve vector optimization problems in many research fields, as demonstrated for example in [ICE, further papers by Alfredo, both ICE and CHP].

A vector optimization problem can be defined as follows:

$$\min \mathbf{F}(\mathbf{x}) = \min(F_1(\mathbf{x}), F_2(\mathbf{x}), \dots, F_k(\mathbf{x}))$$

$$\text{where: } \mathbf{x} \in X \quad F_i: R^n \rightarrow R \quad i = 1, \dots, k \quad k \geq 2$$

where R^k is the objectives space, while R^n is the decision variable space. Therefore, $\mathbf{x} \in R^n$ is a vector decision variable, while $\mathbf{y} = \mathbf{F}(\mathbf{x}) \in R^k$ is a vector of objectives. A vector optimization problem usually provides a set of optimal solutions instead of one single optimal solution, according to the concept of Pareto optimality. For this reason, there is another important problem that must be addressed once that the optimization problem has been solved, that is the decision-making process needed when the identification of a single solution among the optima is required. In particular, the minimum Euclidean distance has been used as decision-making criterion within the proposed methodology, i.e. the minimum distance from an ideal solution located in the axes origin of the objective function space. Indeed, if the minimization of the difference between experimental and numerical quantities is required as objective, an ideal optimal solution is overlapped to the axes origin. Concerning the 1D model calibration, as the best solution, it has been identified the one closest to the origin of the axes, described by the equation:

$$\min \sqrt{\sum_{i=1}^{16} \sum_{j=1}^6 x_{i,j}^2} \quad (5.6)$$

Where:

$$x_{i,j} = \left| \frac{Q_{exp,i,j} - Q_{mod,i,j}}{Q_{exp,i,j}} \right| \quad (5.7)$$

$Q_{exp,i,j}$ is the j experimental quantity in the i experimental condition. $Q_{mod,i,j}$ is the j quantity evaluated by the model in the i experimental condition.

In this Thesis, the vector optimization problem is formulated and solved according to the scheme represented in *Figure 5.8.*, where the objective functions are some of the main quantities obtained as output from the developed 1D thermo-fluid dynamic engine model already described in paragraph 5.2. This model, characterized by a certain number of input parameters and simulation output, is coupled to the genetic optimization algorithm MOGA II, whose details are discussed in [64]. If

compared to the MOGA, the MOGA II includes some features that avoid early convergence to local optimum. Before solving the problem, the input parameters are firstly defined as decision variables of the optimization problem. Then, a set of objective functions are selected among the main simulation output. Finally, number of generations, stop criteria, selection, mutation and crossover occurrence are set. The algorithm MOGA II uses the output values of the objective functions (i.e. air mass flow rate, BSFC, crank angle at maximum pressure, in-cylinder maximum pressure, torque and turbine speed) provided by the engine model to assess the fitness of the current population. Then, new populations are generated according to the predefined values adopted for the genetic operators' probabilities, namely selection, crossover and mutation. Therefore, the search efficiency can be improved by selecting proper values for its genetic operators, that are classical crossover, mutation and selection, as in the MOGA. Moreover, directional crossover is also implemented together with the use of elitism to preserve both the individuals that are closest to the Pareto optimal front and those characterized by the best dispersion.

A further set of mathematical methods, like the Sobol technique, is also used to generate the initial population provided to the optimization algorithm. In particular, Sobol is a deterministic algorithm aimed at performing a uniform sampling of the design space.

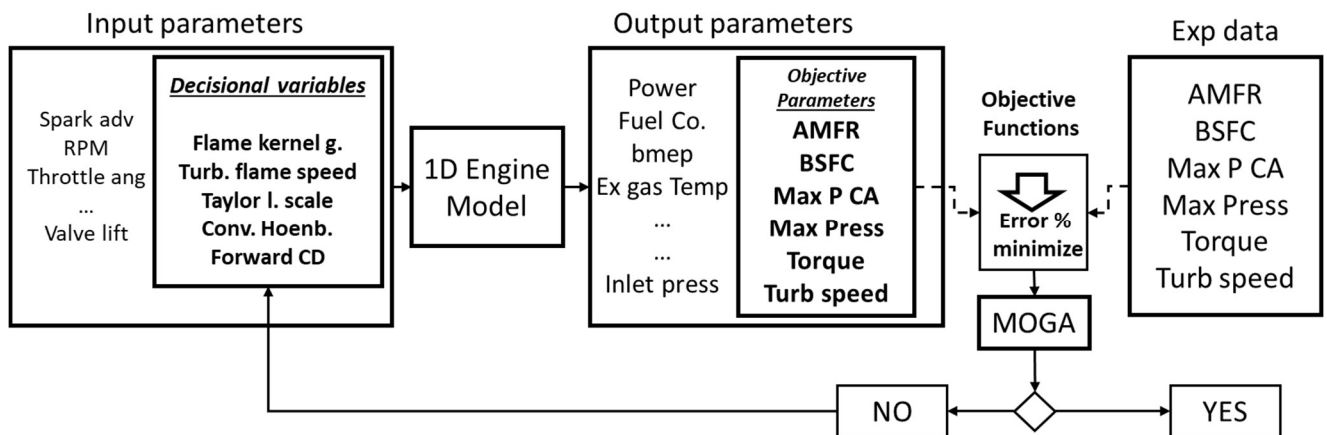


Figure 5.8 – schematization of the automated engine model validation process

The Figure 5.8 shows a schematization of the automated calibration process used. In this process, the input parameters can be distinguished in:

- Parameters that describe the operating condition of the engine such as boundary conditions, engine speed, ignition advance, opening angle of the throttle valve and so on,

- Decision variables, model calibration parameters that are invariant with the changing operating conditions.

To be correct from a physical and modelling point of view, each calibration parameter has the same value for all engine operating conditions. The chosen decision variables are:

- Flame kernel growth (C_1) described in the equation (4.13),
- Turbulent speed multiplier (C_2) described in the equation (4.14),
- Taylor length scale multiplier (C_3) described in the equation (4.15),
- Heat transfer multiplier (C_4) described in the equation (4.21)
- Forward flow coefficient (C_5) described in the equation (4.23).

Based on the boundary conditions, on the input parameters and the decision variables, the engine model will provide a large number of output parameters, such as power, exhaust gas temperatures, *bmep*, fuel mass flow rate. Among these, the parameters on which there is the greatest interest are those shown in *Figure 5.4*:

- Air mass flow rate
- BSFC
- Crank angle at maximum pressure
- In-cylinder maximum pressure
- Torque
- Turbine speed

In fact, these quantities have been chosen as target parameters: as objective function of the optimization problem, it has been chosen the minimization of the error among the 6 target parameters and the respective experimental quantities in the 16 operating conditions, described in *Table 5.5* according the equation:

$$\min \frac{(Q_{j,mod} - Q_{j,exp})}{Q_{j,exp}} \quad (5.8)$$

The genetic algorithm recombines the decision variables that give positive results in terms of achieving the objective functions, leaving the values of decision variables that give worse results "die".

3 different validations have been carried out by increasing the number of operating conditions of the engine in which the error between the quantity assessed by the model and the experimental quantity is reduced:

- The first validation is called 5x18 because 5 decision variables and 18 objective functions have been chosen, that is, the minimization of the error of the 6 objective parameters in 3 different operating conditions,
- The second validation is called 5x30 because 5 decision variables and 30 objective functions have been chosen, that is, the minimization of the error of the 6 objective parameters in 5 different operating conditions,
- The third validation is called 5x96 because 5 decision variables and 96 objective functions have been chosen, that is, the minimization of the error of the 6 objective parameters in 16 different operating conditions.

5.3.4. Validation 5x18

The first validation has been conducted with the aim of minimizing the 6 objective functions in 3 of the 16 operating conditions described in *Table 5.5* and in particular to those at 1492, 3000 and 5500 rpm. After 4200 iterations, 3506 points belonging to the Pareto front have been identified: this front, given the six control quantities, is a hyper-surface, that is, a surface visible only in a six-dimensional hyperspace. To determine the best solution, the percentage error has been first calculated for each of the six control quantities and then the one closest to the origin of the 6-dimensional hyperspace has been chosen, as described in the equations (5.6) and (5.7). This solution is the one identified by the decision variables described in the *Table 5.10*.

Table 5.10 – values of the decision variables reached at the end of the validation 5x18

Flame Kernel Growth	Turbulent Flame Speed	Taylor Length Scale	Conv_Hohenberg	Forward CD
1	1.2	1.6	1.2	1

These variables have been inserted as input into the model to simulate the 16 operating conditions in the *Table 5.5*. In this way it is possible to make a comparison between the 3 validations carried out. The table *Table 5.11* shows the mean error and the total mean error evaluated according to the equations (5.1). From a comparison between this table and table *Table 5.6* it can be seen that all the quantities analysed are characterized by a reduction in the mean error. The mean total error, in fact, is reduced by almost half, reducing from 6.58 to 3.52%.

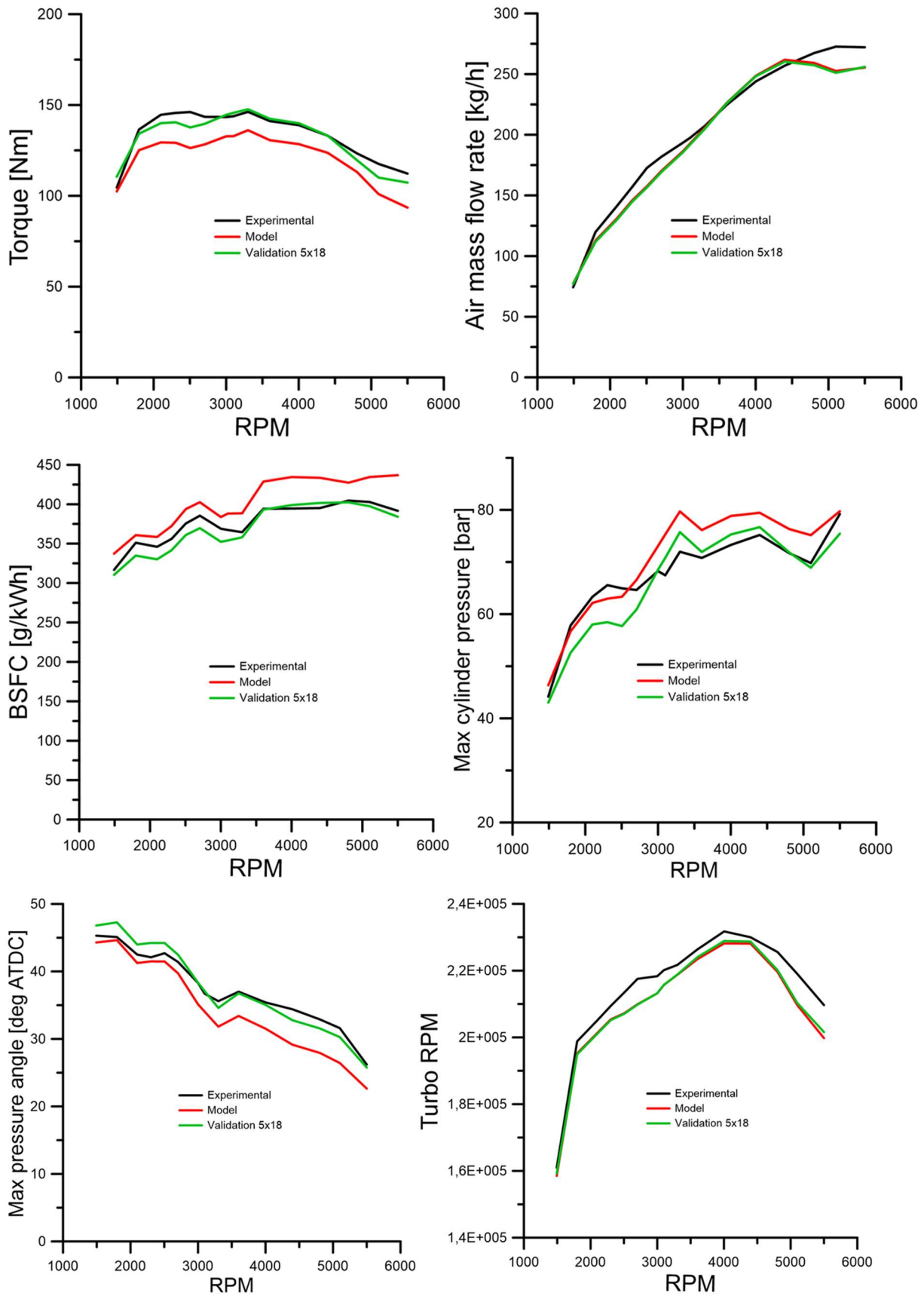


Figure 5.9 - comparison between trends of some experimental quantities (in black), numerical quantities using a heuristic validation (in red) and numerical quantities using the validation 5x18

Table 5.11 - error reached by a comparison between experimental data and numerical quantities after the validation 5x18

	Torque	BSFC	Air mass flow rate	Turbo Speed	Max pressure	Angle@ Max Pressure
Mean error %	2,9	2,7	5,1	2,2	5,1	2,8
Total Mean error %	3,5					
Max Error %	11,5 Pmax@2500					

Despite this, there are still quite high errors (greater than 10%), such as the 11.46% error relating to the maximum pressure at 2500 rpm.

The graphs in the *Figure 5.9* show the trends relating to the 6 experimental quantities used as objective parameters in the 16 operating conditions analyzed. The graphs confirm what has been described above, namely that the trends relating to the 5x18 validation (in green) describe the experimental trends with greater faithfulness (black curves).

5.3.5. Validation 5x30

A second validation has been carried out in order to reduce the error between the quantities evaluated by the model and the experimental quantities: the objectives are, as for the validation 5x18, the minimization of the 6 objective functions by adding 2 conditions out of the 16 operating conditions described in *Table 5.5* to the 3 previously analyzed and in particular to those at 1492, 3000 and 5500 rpm have been added the two conditions at 2303 and 4398 rpm.

The validation ended after 4800 reiterations, identifying 3541 points belonging to the Pareto front. The best solution is that obtained using the calibration variables described in the *Table 5.12*.

Table 5.12 - values of the decision variables reached at the end of the validation 5x30

Flame Kernel Growth	Turbulent Flame Speed	Taylor Length Scale	Conv_Hohenberg	Forward CD
0.4	1.4	1.5	1.2	1.1

Also in this case, the variables have been inserted as input to carry out a comparison with the experimental data in all 16 operating conditions.

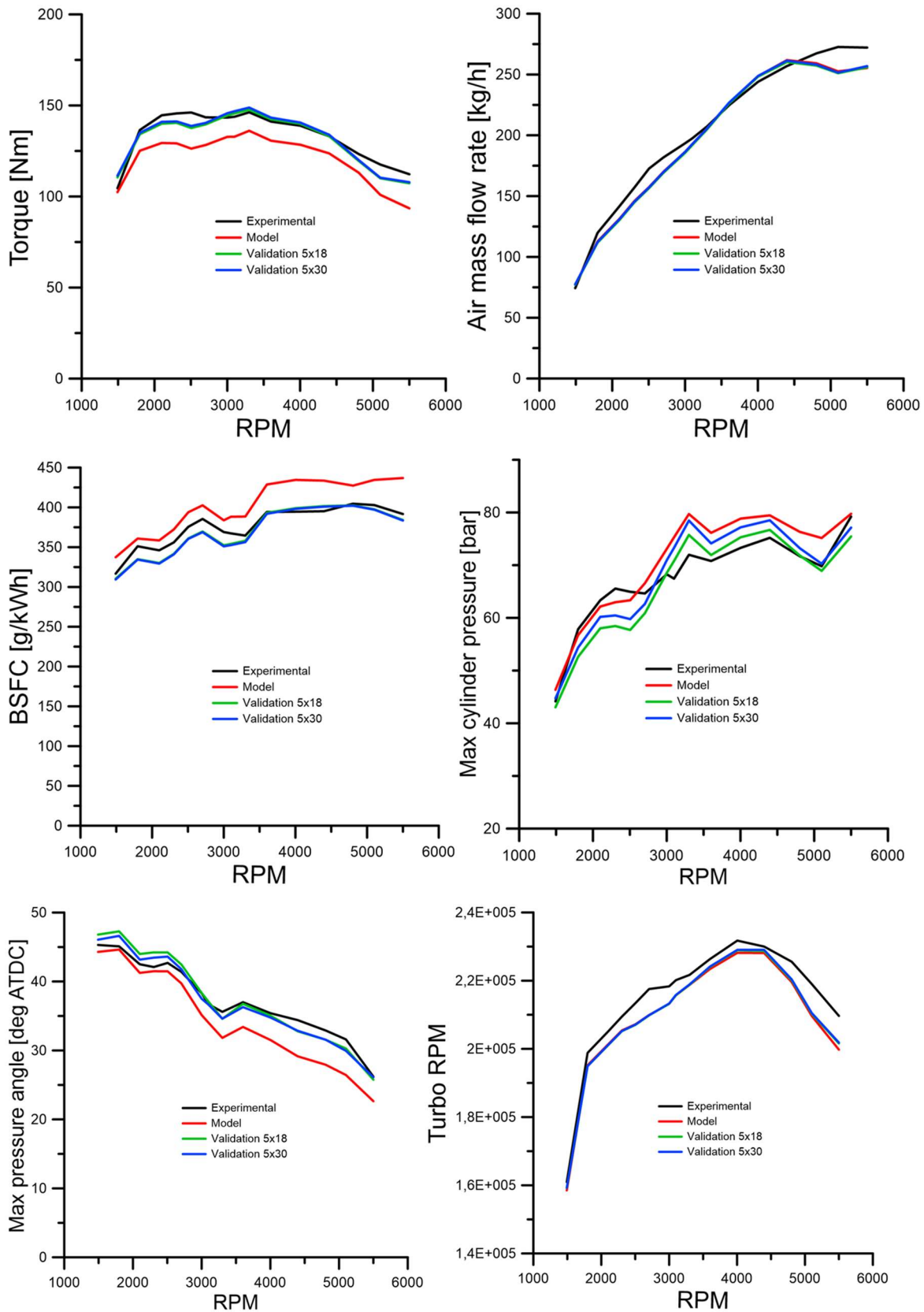


Figure 5.10 - comparison between trends of some experimental quantities (in black), numerical quantities using a heuristic validation (in red), using a validation 5x18 (in green) and using a validation 5x30 (in blue)

The *Table 5.13* shows the mean errors of the 6 quantities used as objective parameters and the mean total error. It can be noted that, compared to the results relating to the 5x18 validation in *Table 5.11* not all errors have been reduced: in particular the mean errors relating to the air mass flow rate and the BSFC increase slightly, despite a reduction of the mean total error. The most interesting thing to note, which is the purpose of this further validation, is the reduction of the maximum error, which goes from 11.46% relative to the maximum pressure at 2500 rpm to 8.97% relative to the air mass flow rate always at 2500 rpm.

Table 5.13 - error reached by a comparison between experimental data and numerical quantities after the validation 5x30

	Torque	BSFC	Air mass flow rate	Turbo Speed	Max pressure	Angle@ Max Pressure
Mean error %	2,9	2,9	4,9	2,1	5,1	2,3
Total Mean error %	3,4					
Max Error %	9, air mass flow rate @ 2500					

This can also be seen graphically. In fact in the graphs in the *Figure 5.10* the blue curve relating to the 5x30 validation is very close to the green curve (5x18 validation), but the maximum errors are reduced as can be seen, for example, in the graph relating to the maximum pressure in the cylinder, with the reduction of the error peak to 2500 rpm.

5.3.6. Validation 5x96

This trend of reduction of the total mean error and of the maximum errors due to an increase in the experimental tests used in the validation process suggested further validation, this time using all 16 available operating conditions. After 5000 iterations 4320 solutions belonging to the Pareto front have been identified. Again, the one closest to the origin of the axes has been chosen as the optimal solution. The values of the decision variables of the best solution are shown in *Table 5.14*.

Table 5.14 - values of the decision variables reached at the end of the validation 5x96

Flame Kernel Growth	Turbulent Flame Speed	Taylor Length Scale	Conv_Hohenberg	Forward CD
0.763	1.199	1.531	1.26	1.03

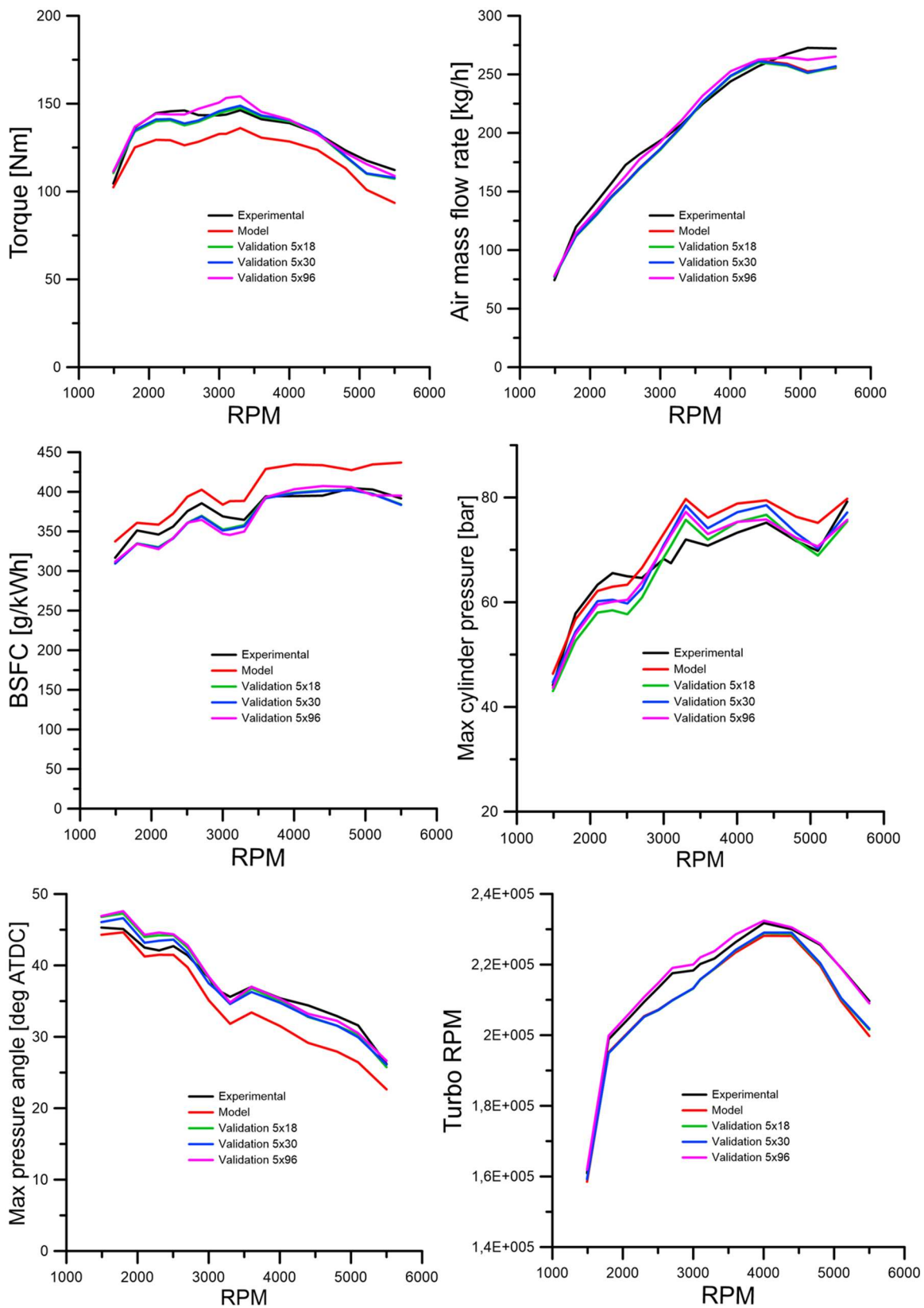


Figure 5.11 - comparison between trends of some experimental quantities (in black), numerical quantities using a heuristic validation (in red), using a validation 5x18 (in green), using a validation 5x30 (in blue) and using a validation 5x96 (in purple)

The *Table 5.15* shows the mean errors relating to the 6 experimental quantities used for the validation process. Also in this case, as in the previous one, it can be noted that not all errors are reduced: the errors relating to the torque, air mass flow rate and maximum pressure decrease, while the errors relating to the BSFC, turbine rotation speed and in the cylinder maximum pressure crank angle increase slightly.

Table 5.15 - error reached by a comparison between experimental data and numerical quantities after the validation 5x96

	Torque	BSFC	Air mass flow rate	Turbo Speed	Max pressure	Angle@ Max Pressure
Mean error %	2,6	3,4	3,2	3,5	4,2	2,8
Total Mean error %	3,3					
Max Error %	8,5 p Max @ 2500 rpm					

Despite this, the total mean error is further reduced compared to the 5x30 validation. This is due to the fact that also in this case there is a reduction of the maximum error peaks, going from a maximum error of 8.97% relative to the air mass flow rate at 2500 rpm to 8.5% relative to the in cylinder maximum pressure always at 2500 rpm, as can be seen from the graphs in the *Figure 5.11*. This reduction is mainly due to the criterion for choosing the optimal solution. By choosing the solution closest to the origin of the axes, all the objective functions are given the same weight, favouring a solution that determines a simultaneous reduction of all errors.

5.4. Analysis and results of the validations

The multi-variable-multi-objective validation methodology is an adequate procedure for automating the calibration process of the 1D engine models, as it reduces the degree of ignorance of the model.

The histogram in *Figure 5.12* shows the mean total error in the 16 operating conditions for various validations carried out by increasing both the calibration variables and the objective functions. In particular, in addition to the 3 validations described above, 2 validations have been carried out: a validation with 4 calibration variables and 1 objective function using 1 operating condition and a validation with 4 calibration variables and 6 objective functions in 1 operating condition. The graph highlights that when the calibration variables and the objective functions increase, the error between

experimental quantities and quantities obtained from the model decreases. In addition to the reduction of the mean total error, this procedure, unique from the criterion of choosing the optimal solution, determines a reduction in the maximum error, attributing robustness to the engine model.

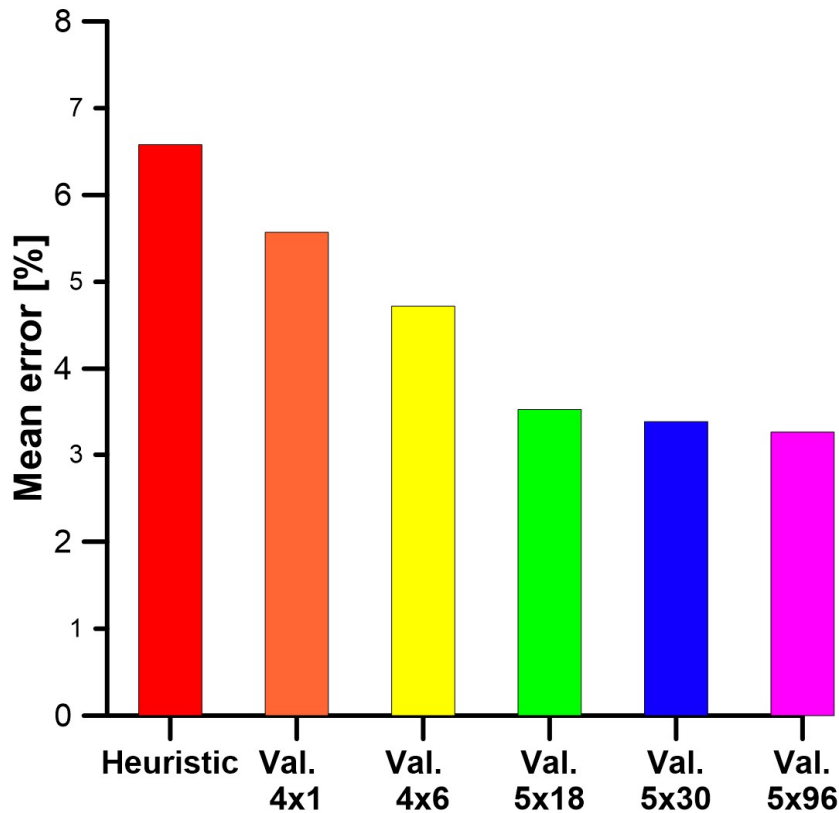


Figure 5.12 – total mean error using different validation

Since the engine model should be used to derive numerous experimental quantities in a wide range of engine operations, the error reduction must involve all the engine quantities estimated by the model, and not just six target parameters.

The *Figure 5.13* and *Figure 5.14* show the mean total error relating to some quantities not used as objective parameters in the validation procedure. As can be seen, this procedure not only reduces the error relating to the six engine parameters used for validation but improves all the operating parameters of the engine. In particular, the trend of the percentage error for the volumetric efficiency, the pressure at the top death center, the fuel mass flow rate and the manifold pressure are reported.

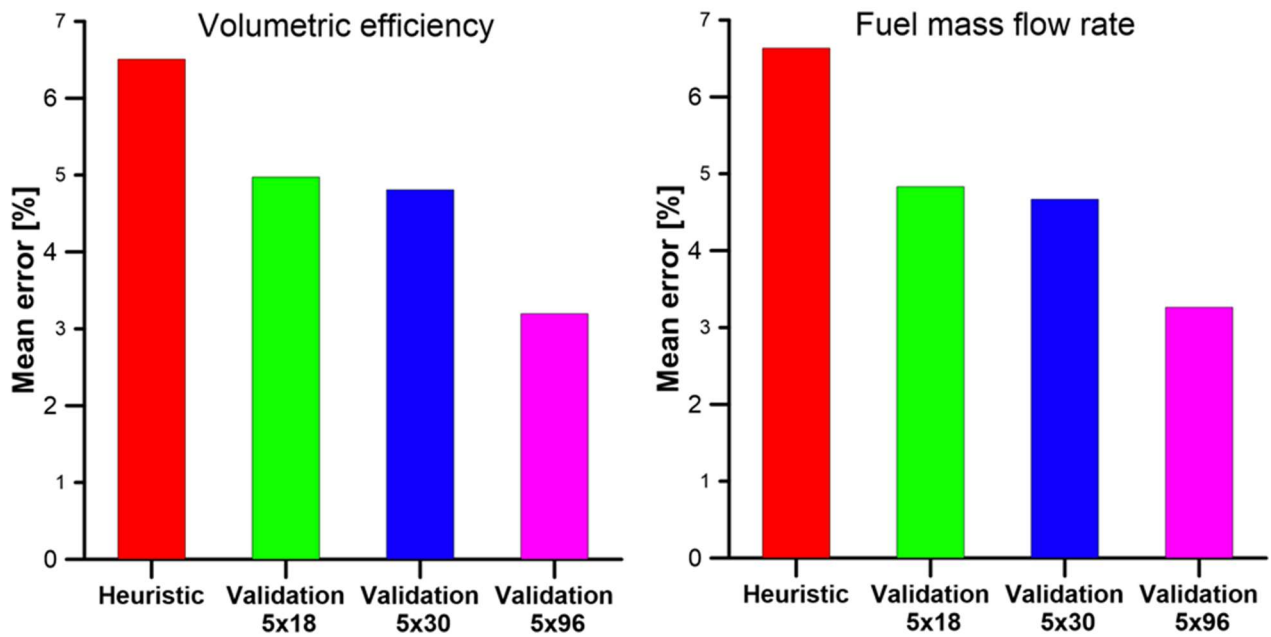


Figure 5.13 - total mean error relating to some quantities not used as objective parameters in the validation procedure: volumetric efficiency (left) and fuel mass flow rate (right)

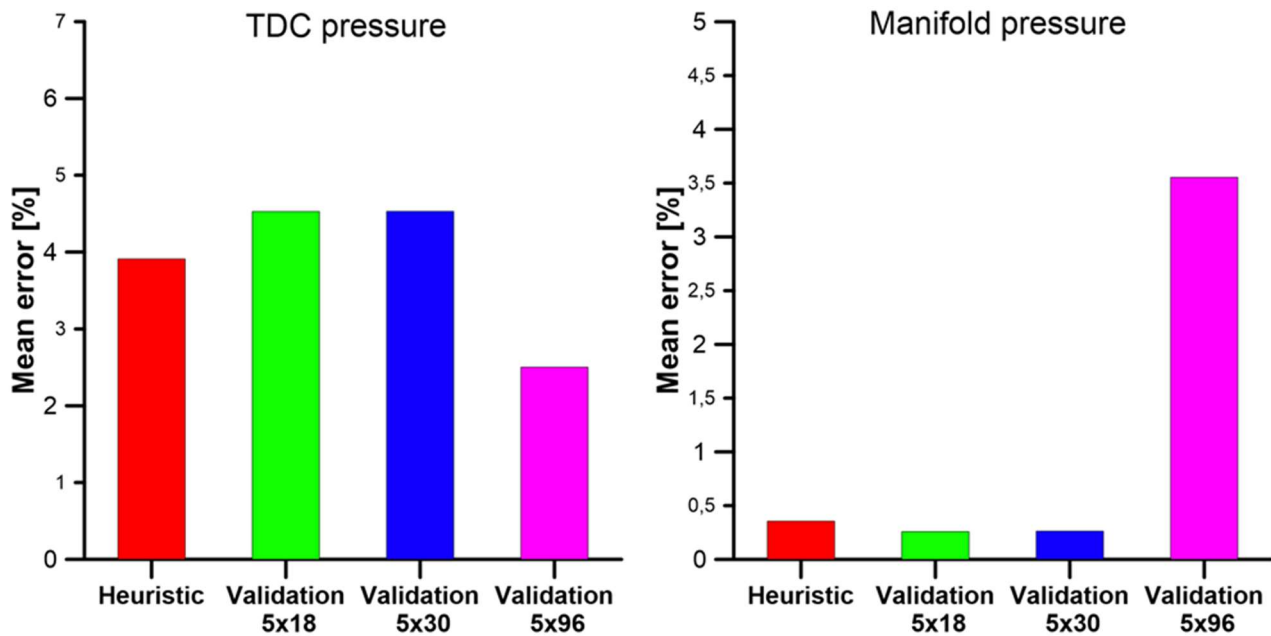


Figure 5.14 - total mean error relating to some quantities not used as objective parameters in the validation procedure: top dead center pressure (left) and manifold pressure (right)

Figure 5.14 shows the trend of the percentage error relating to the manifold pressure. It can be noted that in the last validation the error is greater than the previous ones and even greater than the heuristic calibration. This is not an error in the optimization, but the latter has made it possible to

identify an error that could be due to experimental data, or more likely to an incorrect scaling of the turbo compressor maps.

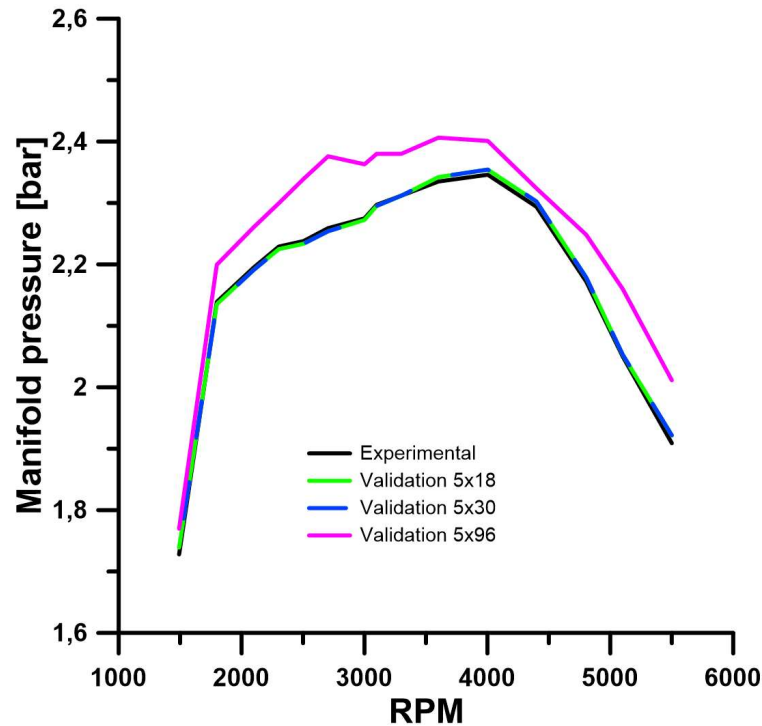


Figure 5.15 – trend of the manifold pressure: experimental data (black), validation 5x18 (green), validation 5x30 (blue) and validation 5x96 (purple)

In the 5x18 and 5x30 validations the wastegate valve PID controller is set to chase the boost pressure: in practice the wastegate valve is opened or closed to chase the set boost pressure value. In the 5x96 validation, however, the PID controller has been set to track the speed of the turbocharger: in this case the wastegate valve is opened or closed to track the set value of the turbocharger speed. The figure *Figure 5.15* shows the trend of the boost pressure obtained from the 3 validations: it can be seen that in the 5x18 and 5x30 validation the pressure value is very close to the experimental one, precisely because it was imposed as a parameter to be followed. The 5x96 validation shows instead a higher error since in this case the speed of the turbocharger was set as a parameter to be followed. The opposite is true, however, as regards the trend of the turbocharger speed as shown in *Figure 5.1*. This is probably due to an error either in acquiring the speed of the turbocharger or in the maps of the compressor and the turbine. In fact, at the same compressor speed, air mass flow rate, upstream and downstream pressure and temperature, the calculated pressure drop is different from the experimental one.

6. Development of experimental campaign thought the use of validated 1D-0D engine model

6.1. Description of the Engine calibration with 1D simulation

After the validation of the engine model, according to the calibration variables in *Table 5.14*, and the friction (*paragraph 5.3.1*) and throttle valve (*paragraph 5.3.2*) models, it is possible to proceed with the method proposed and described in *Figure 4.1*. At this point, it is possible to perform virtually an experimental campaign in order to obtain the experimental data and virtual datasheets that will be used as input in the computer aided calibration.

Two experimental campaigns have been carried out virtually, which are the same as those actually used in an industrial calibration process and hence the experimental data are available. Furthermore, the operating conditions of the two strategies are completely different from the 31 used for validating the model. To distinguish the two strategies, they will be renamed respectively as Strategy A and Strategy B. Both strategies can be described according to various steps to follow which describe the operating conditions that the engine, in this case the engine model, must perform. Generally, an operating condition is described by:

- Engine speed
- Throttle valve angle
- Spark advance
- Air to fuel ratio
- Wastegate valve strategy
- Intake and exhaust valves strategy

The last two items are present only if, as in this case, the engine is equipped with a turbocharger and variable valve actuation system.

6.2. Development of experimental campaign: Strategy A

Strategy A can be described as follows:

- The engine speed is fixed and increased by steps. The chosen engine speeds are: 1500, 1800, 2100, 2300, 2500, 2700, 3000, 3300, 3600, 4000, 4400, 4800, 5100, 5500 rpm.
- The wastegate valve is completely opened

For each engine speed the following operations are performed:

- An intake valve closing sweep (EIVC) is made, from the maximum to the minimum allowed value (i.e. 630, 625, 620... 430 CA degrees)
- The throttle valve is regulated to reach a downstream/upstream pressure ratio of 0.88
- The spark advance is modified in order to obtain the maximum torque or incipient detonation.

The 0D-1D engine model schematized in *Figure 5.1* has been implemented by adding two PID controllers as described in *Figure 6.1*. A first controller has been applied to the throttle valve. This controller receives as input the pressure signals upstream and downstream of the throttle valve and activates the opening angle of the valve in order to reach the pressure ratio equal to 0.88. A second controller has been applied to the two cylinders to adjust the spark advance so as to reach the maximum torque. In *Figure 6.2* part of the valve lifts of the intake valves imposed in the various operating conditions are represented.

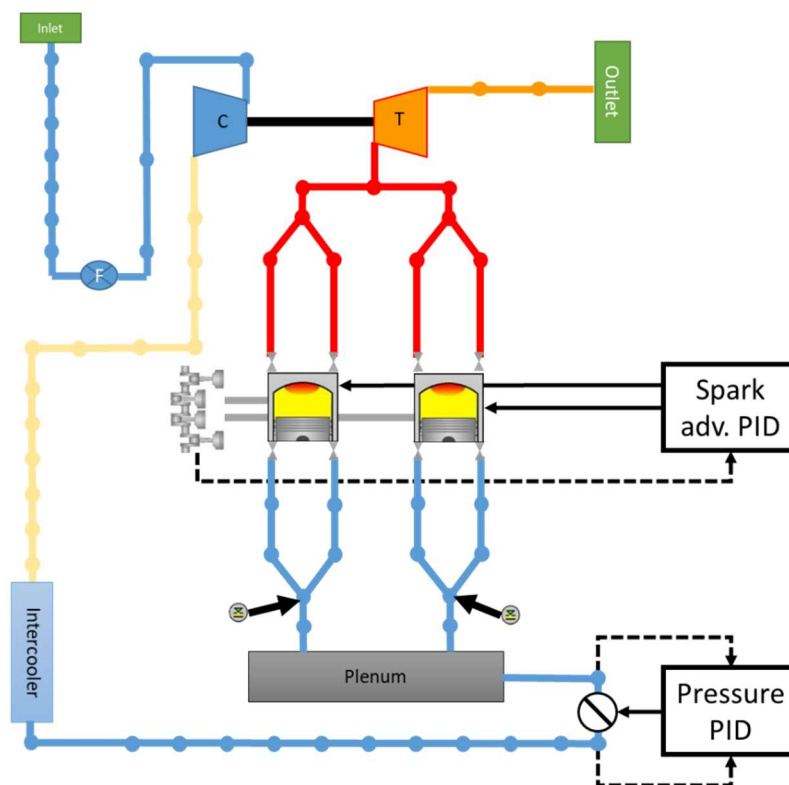


Figure 6.1 – 0D-1D engine configuration for Strategy A

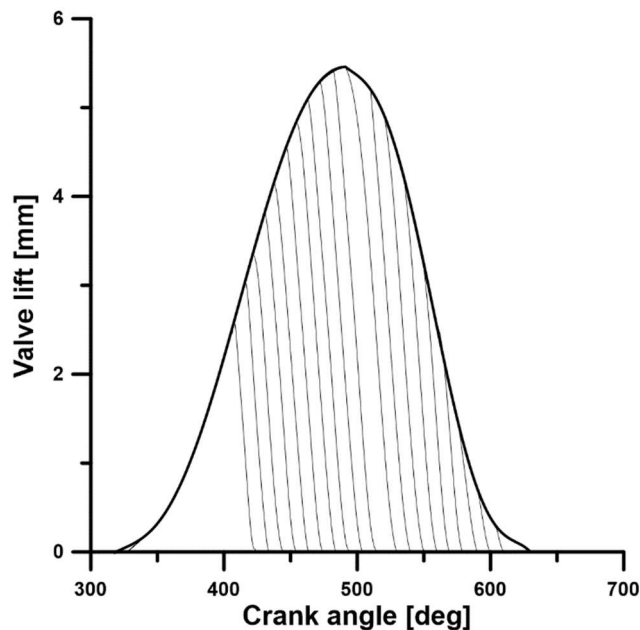


Figure 6.2 – valve lifts used in different engine conditions

With this strategy 285 different simulated operating conditions have been obtained, from which all the experimental quantities necessary for the ECU base calibration process are obtained.

6.3. Development of experimental campaign: Strategy B

This strategy can be divided into two different phases, namely Phase 1 and Phase 2, depending on the use of the turbocharger wastegate valve.

Phase 1:

- The engine speed is fixed and increased by steps as for Strategy A
- The intake valves perform the maximum lift
- The wastegate valve is completely opened

for each engine speed the following operations are performed:

- A throttle valve opening sweep is performed from the minimum to the WOT condition
- The spark advance is modified in order to obtain the maximum torque or incipient detonation.

Phase 2:

- The engine speed is fixed and increased by steps as for Phase 1
- The intake valves perform the maximum lift
- The throttle valve is completely opened (WOT)

for each engine speed the following operations are performed:

- A boost pressure sweep is performed by adjusting the opening of the wastegate valve until reaching the maximum boost pressure for that engine speed.
- The spark advance is modified in order to obtain the maximum torque or incipient detonation.

In this case, two different configurations have been used for the two phases. The first configuration requires the presence of a single PID controller which determines the spark advance to obtain the maximum torque, since that the wastegate is completely open and the opening of the throttle valve is imposed condition by condition. The second phase involves the presence, in addition to the spark advance control, a second control that determines the opening of the wastegate valve in order to achieve a target pressure of the manifold. The new implementation is schematized in *Figure 6.3*.

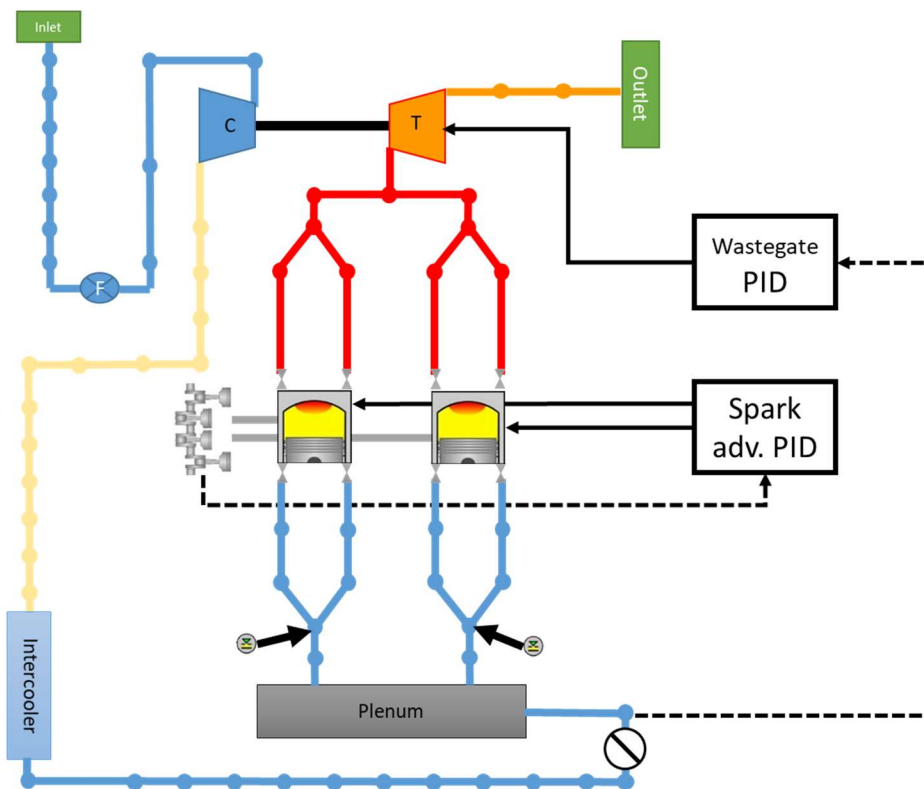


Figure 6.3 - 0D-1D engine configuration for Strategy B

With this strategy we have obtained 243 operating conditions, 160 for Phase 1 and 83 for Phase 2, for a total of 528 operating conditions at different engine speeds: 1500, 1800, 2000, 2300, 2500, 2700, 3000, 3300, 3600, 4000, 4400, 4800, 5100, 5500 RPM.

6.4. Analysis and results

After obtaining all the physical quantities necessary for the calibration process from the engine model, these quantities have been collected in two different datasheets, called Virtual Datasheet A and B respectively. The virtual datasheets have been compared with the respective real datasheets in the same operating conditions, in order to verify the validity of the proposed methodology.

The results of this comparison are shown in *Figure 6.4* for strategy A and in *Figure 6.5* for strategy B. *Figure 6.4* represents the trend of the error between experimental and calculated quantities using the first strategy described.

The quantities shown are: torque, manifold pressure, air mass flow rate. Each column represents the mean percentage error at each engine speed $\bar{e}_{\%,i}$, calculated as:

$$\bar{e}_{\%,i} = \sum_{j=1}^n \frac{(Q_{j,mod} - Q_{j,exp})}{Q_{j,exp}} * \frac{100}{n}$$

where $Q_{j,exp}$ is the j-th experimental quantity, $Q_{j,mod}$ is the j-th quantity evaluated by the 1D engine model, n is the number of operating conditions at the same engine speed. As can be seen from the graph the mean error varies from 0.35% for the manifold pressure at 1500 RPM to 8.05% for the torque at 1500 RPM. *Figure 6.5* shows the trend of the mean percentage errors for the torque, BSFC and air mass flow rate for the second strategy. In this case the error varies from 1.02% for the torque at 5100 RPM to 11.77% for the BSFC at 5500 RPM. However, the mean total error valued as:

$$\bar{e}_{\%} = \sum_{i=1}^n \frac{\bar{e}_{\%,i}}{N}$$

always remains below 5%.

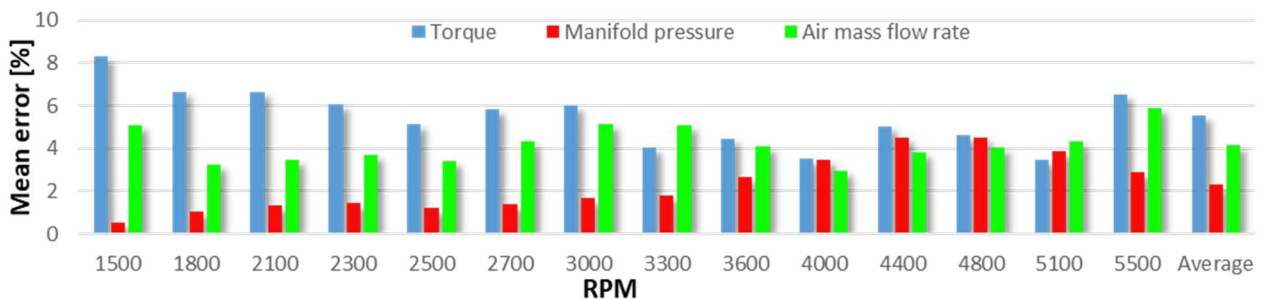


Figure 6.4 - Comparison between experimental and calculated mean data for Strategy A.

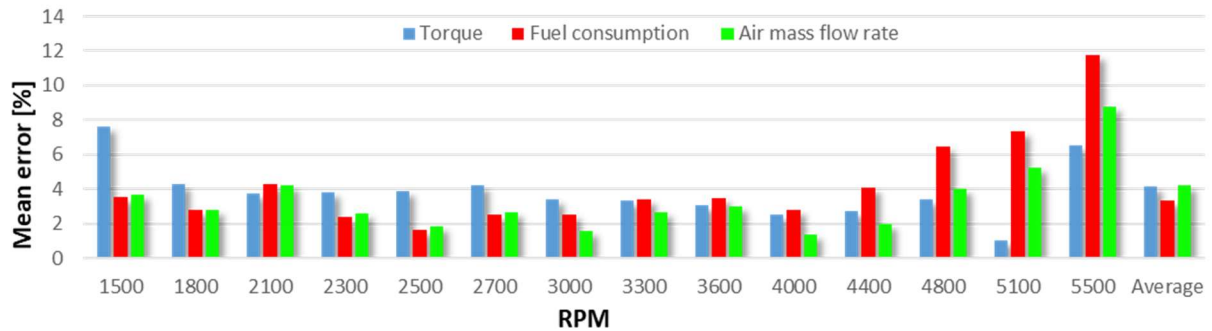


Figure 6.5 - Comparison between experimental and calculated mean data for Strategy B.

The quantities obtained from the one-dimensional model faithfully reproduce the trend of the experimental quantities in all operating conditions. In support of this statement, the Figure 6.6 shows the trend of the torque obtained with the model in the two experimental campaigns: Figure 6.6 (a) shows the torque as a function of the IVC angle values at 4400 rpm according to the strategy A. Similarly, Figure 6.6 (b) represents the torque at 4400 rpm according to the strategy B. In both cases it is possible to appreciate how the trend of the calculated torque faithfully follows the trend of the experimental one.

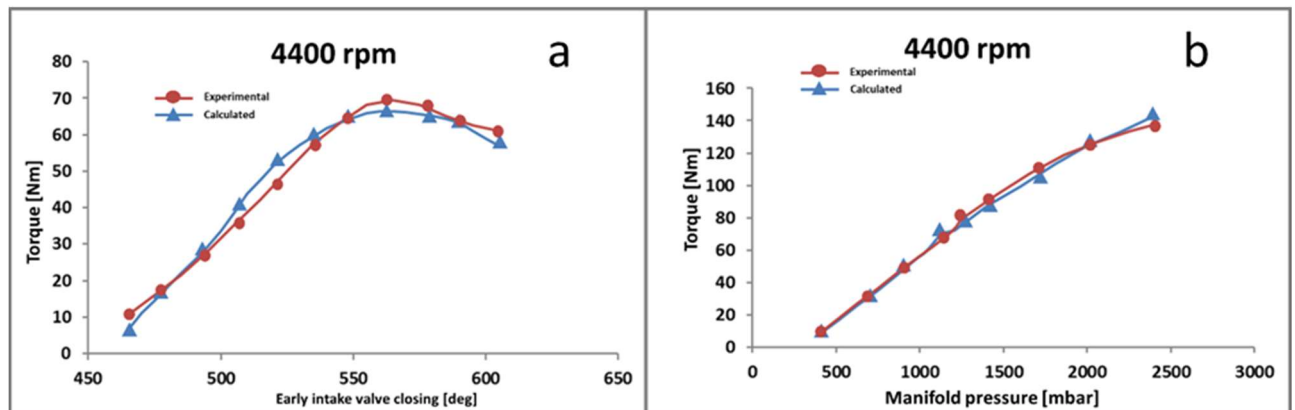


Figure 6.6 - Comparison between experimental and calculated torque at 4400 rpm for the two strategies

After obtaining the datasheets, the next step has been carried out, i.e. using the datasheets as input in the computer aided calibration. Initially, a new calibration of the volumetric efficiency function has been performed with real experimental data using only the operating conditions that are present in both the datasheets.

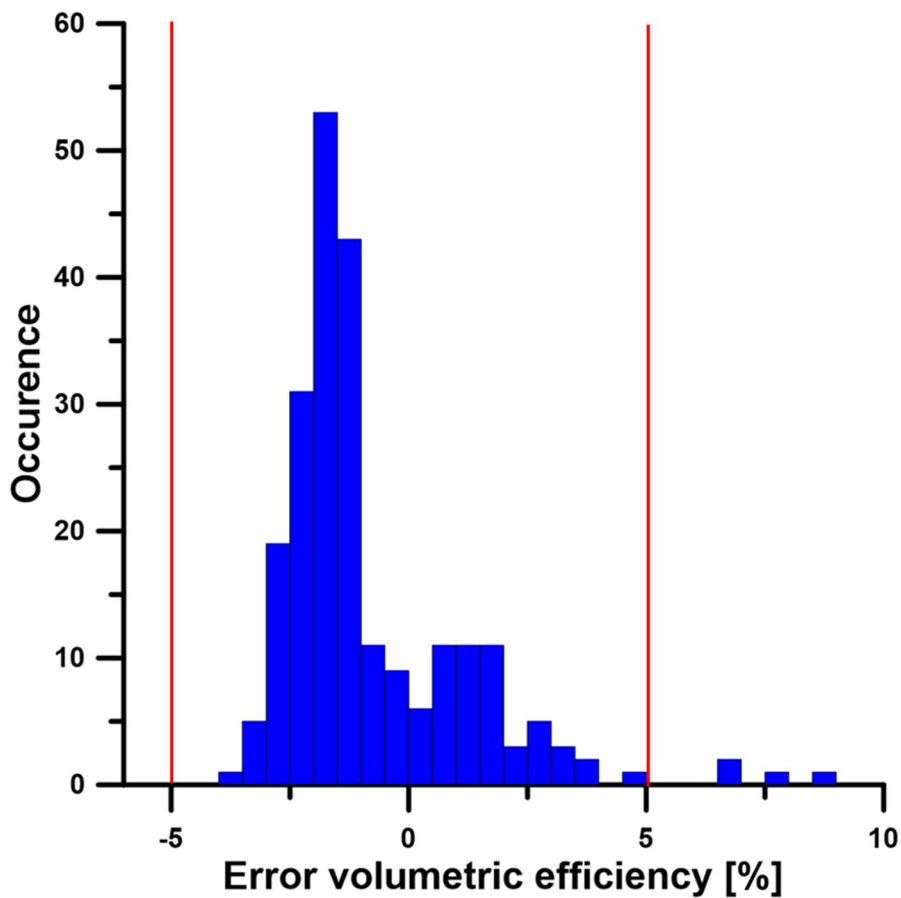


Figure 6.7 – occurrence of the volumetric efficiency function error using the experimental datasheet

Figure 6.7 shows the error distribution between the volumetric efficiency assessed by the control unit function calibrated with the real datasheet and the experimental volumetric efficiency. In this case, the calibration performance is very high: over 98% of errors fall within the acceptable range of $\pm 5\%$.

Subsequently, the same procedure has been carried out with the datasheet obtained from the virtual campaign, in particular the experimental campaign carried out with strategy B. Figure 6.8 shows the calibration results of the function that assesses volumetric efficiency. It can be seen that the calibration performance has remained high. In fact, the error distribution between the volumetric efficiency evaluated by the control unit calibrated with the virtual datasheet and the experimental volumetric efficiency shows that 90% of the errors fall within the acceptable range of $\pm 5\%$. This is a very positive result, remembering that the 0D-1D model has been validated by acquiring only 31 experimental tests.

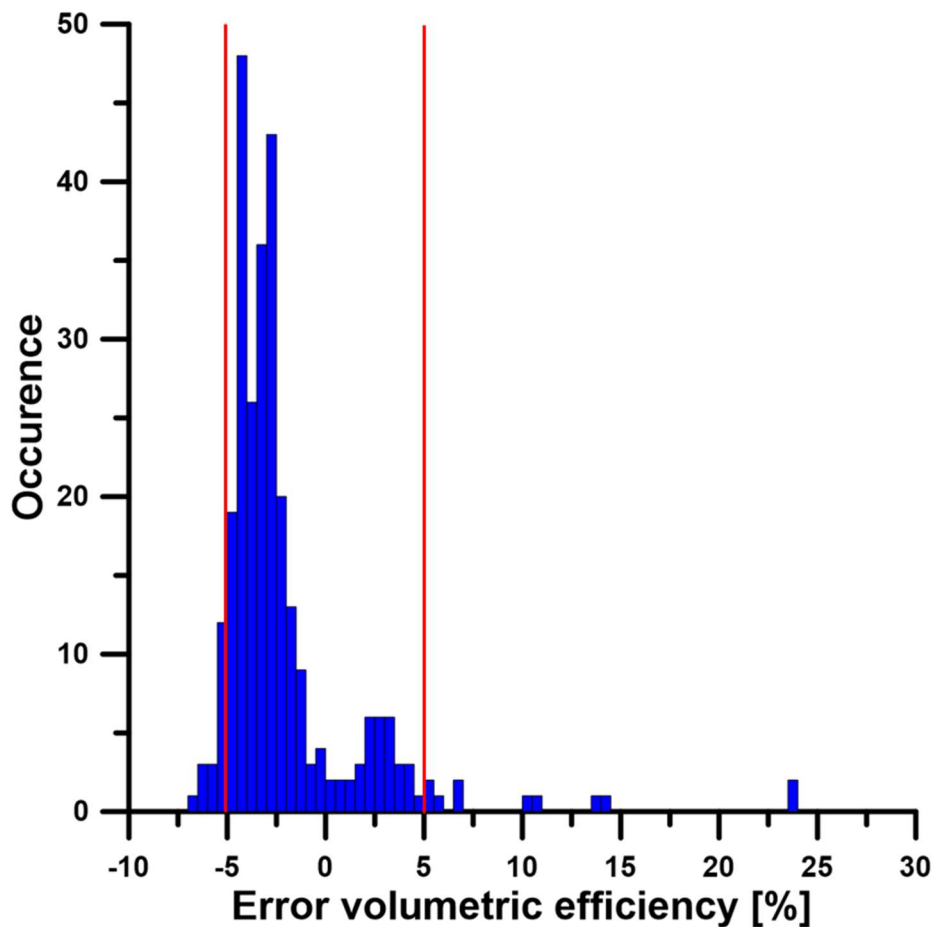


Figure 6.8 - occurrence of the volumetric efficiency function error using the virtual datasheet

First, the 90% performance value relating to the virtual datasheet is considered acceptable for the function in question. Secondly, the uncertainty of the experimental tests must be taken into account. In addition to the uncertainty caused by measuring instruments, the uncertainty of the operator and the controller must be considered. In fact, when it's set an objective to control, such as the pressure ratio value of 0.88 in strategy B, experimentally it's accepted that this value is not exact but there is a small error. On the other hand, the numerical control is carried out in a more rigorous manner.

Table 6.1 shows an extract of the two datasheets highlighting the P1 and P2, which are respectively the pressure upstream and downstream of the throttle valve, and P2/P1 which is one of the targets to be reached during strategy B. The value of this ratio must be 0.88. From the table it can be seen that the control to achieve the target is carried out with greater precision in the numerical tests. In fact, the ratio between the downstream pressure and the upstream pressure of the throttle valve is always equal to 0.88.

Table 6.1 - extract of the datasheet that highlights the pressure upstream and downstream of the throttle valve

Virtual datasheet			Real datasheet		
P1	P2	P2/P1	P1	P2	P2/P1
[mbar]	[mbar]		[mbar]	[mbar]	
1202	1057	0.88	1228	1063	0.87
1142	1003	0.88	1250	1076	0.86
1100	968	0.88	1253	1074	0.86
1065	937	0.88	1248	1074	0.86
1040	915	0.88	1240	1068	0.86
1029	905	0.88	1219	1053	0.86
1033	908	0.88	1189	1028	0.86
1038	912	0.88	1151	1000	0.87
1056	928	0.88	1113	966	0.87
1074	944	0.88	1087	949	0.87
1102	968	0.88	1072	935	0.87
1134	996	0.88	1047	914	0.87
1180	1036	0.88	1031	902	0.87
1230	1079	0.88	1030	900	0.87

While in the real case there is an oscillation of this value which in some cases can even exceed 10% with respect to the value of 0.88, generating an alteration of the measurements and consequently of the volumetric efficiency values.

When comparing the real and virtual conditions, it must be considered that the two conditions are not exactly the same, but that this difference on the pressure ratio leads to an error that propagates in the calibration of the function. Probably, a more robust comparison would be made if the actual values of the pressure ratio of each operating condition have been imposed, rather than the goal of reaching the pressure ratio of 0.88. The realization of this comparison, in the face of a considerable effort, would not add significant information on the goodness of the proposed method, since the calibration of the control unit function by using the virtual data sheet would take place considering the results of the virtual data sheet itself as experimental data.

The computer aided calibration software automatically discarded the operating conditions whose error with respect to the 0.88 target value is too high. In this way it is possible to avoid harmful increase in the calibration process costs.

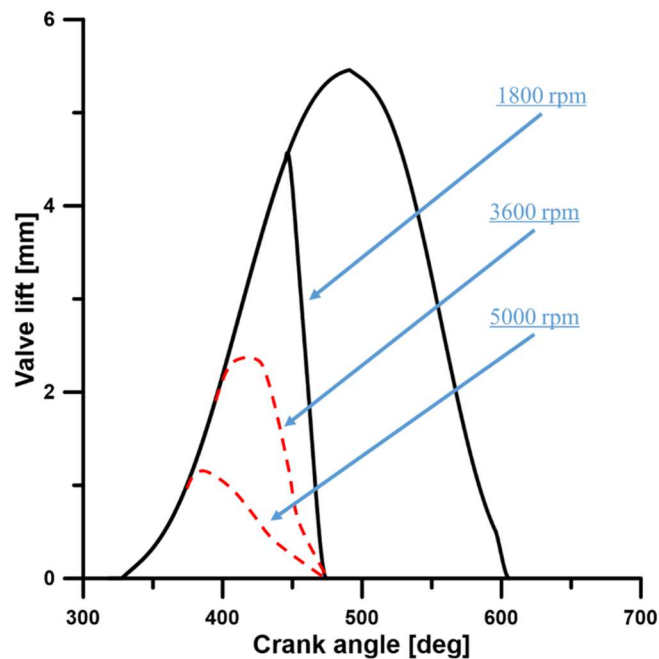


Figure 6.9 – effect of engine speed variation on the valve lift

Furthermore, a simplification that has been made in the realization of the model must also be considered. Strategy B involves a sweep of the closing angle of the intake valves as shown in *Figure 6.2*. The simplification carried out consists in using the same valve lift at different engine speeds, without taking into account the effect of the change in engine speed on the valve closing lift by actuating the same closing angle as shown in *Figure 6.9*. In fact, as the engine speed increases, in order to close at the same angle, due to the inertia present in the intake system, the descent phase will begin first, causing a decrease in the filling of the cylinder and consequently in the operation of the engine. In *Figure 6.9*, the example of 3 valve lifts is shown as the engine speed changes (1800, 3600, 5000 rpm), with the same closing angle of the intake valve (475°). For the realization of the experimental campaign, only the black valve lift was used when the engine speed changed. This simplification is due to the inability of the model to predict the effect of the change in the engine speed on the closing of the intake valves.

As for the second methodology, the use of thermo-fluid dynamic simulation software is recommended. In the market there are various software such as GT-Suite®, produced by Gamma Technologies, AVL-Boost™ or Amesim®, developed by Siemens. Although some of these software have integrated the vector optimization methodology, it is recommended to use dedicated software such as modeFrontier®, produced by Esteco, or MOEA Framework. The thermofluid dynamics simulation software have costs that vary from 20'000 a 40'000 €/year for a single license, while

modeFrontier has a cost that varies between 8'000 and 15'000 €/year. MOEA Framework is a free open-software. The use of these programs requires excellent modeling and engine knowledge, as well as a good knowledge of the problems of multivariable-multi-object optimization.

7. Conclusions and future development

This Thesis work addresses two methodologies developed to overcome some critical issues concerning the base calibration of ECU estimation functions in engine management systems: the reduction of the experimental effort of this process.

Specifically, the first methodology is based on the use of Neural Networks to provide a detailed engine data sheet starting from a reduced number of experimental data. To verify the potential of the proposed methodology, this detailed data set has been used as input to a specific Computer Aided Calibration algorithm and the achievable calibration performance have been evaluated. In particular, reference has been made to the volumetric efficiency function implemented in the electronic control unit of a modern downsized engine. The research clearly demonstrates the effectiveness of the proposed approach since the calibration performance falls within acceptable limits even after a 60% cut of the experimental data usually acquired for calibration purposes. The results highlighted that the proposed methodology may lead to a reduction of development time and costs of the calibration process due to a reduction of the experimental effort. In fact, a cut from 40 to 60% of the available experimental data can be accepted while obtaining similar calibration performance. A future development could be the investigation of the use of neural networks directly on the ECU, paying attention to the problem of the increase in computational times.

The second methodology suggests the use of 1D-0D engine model in substitution of the real one in order to carry out the experimental quantities necessary to the computer aided calibration. In practise the 1D-0D is used as a test bench to carry out extensive experimental campaigns. This methodology strictly depends on a robust validated engine model. Multi-variables multi-objective validation process proved to be fundamental to validate the model. The purpose of this method is to provide, at the end of the research, general guidelines to be followed to carry out the calibration process virtually. Multiple validations have been carried out with the aim of providing more details on which modeling parameters to choose as calibration parameters, or which experimental tests and which quantities to use as objective functions.

The most important and useful result achieved through the developed methodology consists in the fact that the mean error remains relatively low: in the case of the quantities taken into consideration the mean error varies between 5.52% of the torque to 2.30% of the manifold pressure, both obtained from the second acquisition strategy. This, as mentioned, is relevant because the mean percentage error falls within the instrumental errors: in fact, the experimental quantities do not have a perfect

precision and accuracy but they could carry a series of statistical and systematic errors that depend on the instrument used, the type of measurement performed and the experience of the operator. As seen from the comparisons between the two datasheets (*Figure 6.4* and *Figure 6.5*), a very low mean error emerges, which is of the same order of magnitude as the experimental errors: the data thus obtained can be used as input of the computer aided calibration in order to calibrate the control unit functions and complete in this way the ECU base calibration process shown in *Figure 4.1*.

With this methodology 2 datasheets have been developed starting from only 31 operating conditions, making sure that the one-dimensional model of the engine manages to recreate the behaviour of the real engine in completely different operating conditions, which can lead to enormous advantages in terms of production costs of the whole base calibration process.

In this way, only a few dozens of real experimental tests will be required to carry out the calibration process instead of thousands. In the current state, the methodology does not allow to achieve acceptable errors for all the engine operating conditions.

The virtual datasheet has been used as input in a calibration software to calibrate the volumetric efficiency function. From a first comparison between the calibration obtained with the real datasheet and that obtained from the model, it can be seen that, although the calibration performance decreases from 97 to 89%, this is a very promising result as regards future developments.

Indeed, the 1D simulation methodology seems to be the more promising solution since it allows to strongly reduce the experimental effort. A possible future step, to further improve the model reliability, as well the calibration performances, could be the enhancement of the valve model, including the effect of the variation of the engine speed on the valves closure. As regards the final aim of providing general guidelines, even if the use of the 16 experimental tests has proven effective, other validations will be carried out in which experimental tests are chosen at different load values.

Moreover, the final validation of the proposed methodology is to use an ECU equipped with functions calibrated with this method on a real engine on test bench or on a real vehicle.

The two methodologies have been developed through the use of dedicated software, commercially available or to be developed independently.

Although the costs of the recommended software may seem high, it is emphasized that all the major car manufacturers, or companies that deal with calibration, already have dozens of licenses of these software, minimizing the impact on fixed costs.

References

- [1] R. Isermann, Engine Modeling and Control, Modeling and Electronic Management of Internal combustion engines, DOI 10.1007/978-3-642-39934-3.
- [2] Kleppmann W (2003) Versuchsplanung, 3rd edn. Hanser Verlag, M"unchen.
- [3] MontgomeryD (2005) Design and analysis of experiments, 6th edn. John Wiley and Sons, New York.
- [4] Santner J, Williams B, Notz W (2003) The design and analysis of computer experiments. Springer, New York.
- [5] «Centobelli, P. et al., Flow shop scheduling algorithm to optimize warehouse activities, International Journal of Industrial Engineering Computations, Volume 7, Issue 1, 1 December 2016, Pages 49-66. ISSN: 19232926. DOI: 10.5267/j.ijiec.2015.8.001. Sco».
- [6] «Lowe D. et al., Validation of Neural Networks in Automotive Engine Calibration. Artificial Neural Networks, 7-9 July 1997, Conference Publication No. 440, IEE.».
- [7] «Yu-Jia Zhai, Ding-Li Yu, Neural network model-based automotive engine air/fuel ratio control and robustness evaluation, Engineering Applications of Artificial Intelligence 22 (2009) 171–180.».
- [8] «P.J. Shayler et al., The exploitation of neural networks in automotive engine management systems, Engineering Applications of Artificial Intelligence, Volume 13, Issue 2, 1 April 2000, Pages 147-157.».
- [9] «Shivakumar, P. Srinivasa Pai, B.R. Shrinivasa Rao, Artificial Neural Network based prediction of performance and emission characteristics of a variable compression ratio CI engine using WCO as a biodiesel at different injection timings, Applied Energy».
- [10] «Abdullah Uzun, Air mass flow estimation of diesel engines using neural network, Fuel 117 (2014) 833–838. <http://dx.doi.org/10.1016/j.fuel.2013.09.078>.».
- [11] «Harun Mohamed Ismail, Hoon Kiat Ng, Cheen Wei Queck, Suyin Gan, Artificial neural networks modelling of engine-out responses for a light-duty diesel engine fuelled with biodiesel blends, Applied Energy 92 (2012) 769–777. doi:10.1016/j.apenergy.2011.08».
- [12] «Hamid Taghavifar, Hadi Taghavifar, Aref Mardani, Arash Mohebbi, Modeling the impact of in-cylinder combustion parameters of DI engines on soot and NOx emissions at

-
- rated EGR levels using ANN approach, *Energy Conversion and Management* 87 (2014) 1–9. ht».
- [13] «Necla Kara Togun, Sedat Baysec, Prediction of torque and specific fuel consumption of a gasoline engine by using artificial neural networks, *Applied Energy* 87 (2010) 349–355. doi:10.1016/j.apenergy.2009.08.016.».
- [14] «Sumit Roy, Rahul Banerjee, Probir Kumar Bose, Performance and exhaust emissions prediction of a CRDI assisted single cylinder diesel engine coupled with EGR using artificial neural network, *Applied Energy* 119 (2014) 330–340. <http://dx.doi.org/10.1016/>».
- [15] «T. Sardarmehni, J. Keighobadi, M.B. Menhaj, H. Rahmani, Robust predictive control of lambda in internal combustion engines using neural networks, *archives of civil and mechanical engineering* 13 (2013) 432–443. <http://dx.doi.org/10.1016/j.acme.2013.05.>».
- [16] «José Manuel Luján, Héctor Climent, Luis Miguel García-Cuevas, Ausias Moratal, Volumetric efficiency modelling of internal combustion engines based on a novel adaptive learning algorithm of artificial neural networks, *Applied Thermal Engineering* 123 (2)».
- [17] «Sebastian Grasreiner, Jens Neumann, Michael Wensing, Christian Hasse, Model-based virtual engine calibration with the help of phenomenological methods for spark-ignited engines, *Applied Thermal Engineering* 121 (2017) 190–199. <http://dx.doi.org/10.1016/>».
- [18] «Amir-Mohammad Shamekhi, Amir H. Shamekhi, A new approach in improvement of mean value models for spark ignition engines using neural networks, *Expert Systems with Applications* 42 (2015) 5192–5218. <http://dx.doi.org/10.1016/j.eswa.2015.02.031.>».
- [19] «P.J. Shaylera, M. Goodman, T. Ma, The exploitation of neural networks in automotive engine management systems, *Engineering Applications of Artificial Intelligence* 13 (2000) 147-157. [https://doi.org/10.1016/S0952-1976\(99\)00048-2.](https://doi.org/10.1016/S0952-1976(99)00048-2.)».
- [20] «Bozza F. et al., The Prediction of the Performance and Gasdynamic Noise Emitted by a Medium-Size Spark-Ignition Engine by Means of 1D and 3D Analyses. SAE paper 2007-01-0380. DOI: 10.4271/2007-01-0380.».
- [21] «Bozza F. et al. 1D-3D Analysis of the Scavenging and Combustion Process in a Gasoline and Natural-Gas Fuelled Two-Stroke Engine. SAE paper 2008-01-1087.».
- [22] «Bozza F. et al., Numerical and Experimental Investigation of Fuel Effects on Knock Occurrence and Combustion Noise in a 2-Stroke Engine. *SAE International Journal of Fuels and Lubricants*, ISSN: 1946-3952, May 2012, vol. 5 no. 2, 674-695. doi:10.4271/».

-
- [23] «Bozza F. et al., Pre-Lift Valve Actuation Strategy for the Performance improvement of a DISI VVA Turbocharged Engine, Energy Procedia, Volume 45, pages 819-828. ISSN: 18766102. DOI: 10.1016/j.egypro.2014.01.087.».
- [24] «Gimelli A. et al., Study of a New Mechanical VVA System. Part II: Estimation of the Actual Fuel Consumption Improvement through 1D Fluid Dynamic Analysis and Valve Train Friction Estimation, International Journal of Engine Research, SEP 2015, Volume:».
- [25] [Online]. Available: <https://www.epa.gov/caa-permitting/clean-air-act-permitting-california>.
- [26] [Online]. Available: <https://www.embitel.com/blog/embedded-blog/automotive-control-units-development-innovations-mechanical-to-electronics>.
- [27] Brevetto US20130282946A1.
- [28] «Riegel, A., Montalto, I., & De Cristofaro, F. (2007). Interactive optimization methodology for robust base engine calibration. European Automotive Congress. Budapest.».
- [29] «J. Shayler et al., The exploitation of neural networks in automotive engine management systems, Engineering Applications of Artificial Intelligence, Volume 13, Issue 2, 1 April 2000, Pages 147-157.».
- [30] «Castagné M. et al., Comparison of Engine Calibration Methods Based on Design of Experiments (DoE), Oil & Gas Science and Technology – Rev. IFP, Vol. 63 (2008), No. 4, pp. 563-582, DOI: 10.2516/ogst:2008029.».
- [31] «Miettinen, K. (1999). Nonlinear Multiobjective Optimization. Kluwer Academic Publishers.».
- [32] «Rao, S. (1996). Engineering Optimisation Theory and Practice. J.Wiley and Sons.».
- [33] «Wu, C., & Hamada, M. (2000). Experiments. Planning, Analysis, and Parameter Design. Wiley.».
- [34] «Widrow B, Hoff M (1960) Adaptive switching circuits. IRE WESCON Conv Rec pp 96–104.».
- [35] «McCulloch W, Pitts W (1943) A logical calculus of the ideas immanent in nervous activity. Bull Math Biophys 5:115–133.».
- [36] Hecht-Nielson R (1990) Neurocomputing. Addison-Wesley, Reading, M.

-
- [37] Haykin S (1994) Neural networks. Macmillan College Publishing Company, Inc., New York.
- [38] Bishop, C. M. (s.d.). Neural Networks for Pattern Recognition, Oxford university press..
- [39] «Introduction to radial basis function networks, Mark J. L. Orr, Centre to cognitive science, University of Edinburgh».
- [40] Orr, M. J. (1996). Introduction to Radial Basis Function Networks, Centre for Cognitive Science, University of Edinburgh, 2, Buccleuch Place. Edinburgh..
- [41] M. D. Buhmann, Radial basis functions, Acta numerica, 2000, Acta Numer., vol. 9, Cambridge Univ. Press, Cambridge, 2000, pp. 1–38.
- [42] M. D. Buhmann, Radial basis functions, Cambridge Monographs on Applied and Computational Mathematics, vol. 12, Cambridge University Press, Cambridge, 2003..
- [43] Holger Wendland, Scattered data approximation, Cambridge Monographs on Applied and Computational Mathematics, vol. 17, Cambridge University Press, Cambridge, 2005..
- [44] «Boretti, A. Scalzo, J., “Exploring the Advantages of Variable Compression Ratio in Internal Combustion Engines by Using Engine Performance Simulations,” SAE Technical Paper 2011-01-0364, 2011, doi:10.4271/2011-01-0364.».
- [45] «Demesoukas, S., Caillol, C., Higelin, P., Boiarciuc, “Zero-Dimensional Spark Ignition Combustion Modeling-A Comparison of Different Approaches”, SAE Technical Paper, 2013-24-0022, 2013, doi:10.4271/2013-24-0022.».
- [46] «Richard, S., Bougrine, S., Font, G., Lafossas, F.A., Le Berr, F., “On the Reduction of a 3D CFD Combustion Model to Build a Physical 0D Model for Simulating Heat Release, Knock and Pollutants in SI Engines”, Oil & Gas Science and Technology 64(3):223-».
- [47] «Matthews, R., D., Chin, Y., W., “A Fractal-Based SI Engine Model: Comparisons of Predictions with Experimental Data”, SAE Paper 910075, 1991, doi:10.4271/910079.».
- [48] «De Bellis, V., Bozza, F., and Tufano, D., "A Comparison Between Two Phenomenological Combustion Models Applied to Different SI Engines," SAE Technical Paper 2017-01-2184, 2017, doi:10.4271/2017-01-2184.».
- [49] «Review of the development and applications of the Wiebe function: A tribute to the contribution of Ivan Wiebe to engine research. J. Ghojel. International Journal of Engine Research. DOI: <https://doi.org/10.1243/14680874JER06510>».

-
- [50] «Wahiduzzaman, S., Morel, T., and Sheard, S., "Comparison of Measured and Predicted Combustion Characteristics of a Four-Valve S.I. Engine," SAE Technical Paper 930613, 1993, doi:10.4271/930613».
- [51] «Chen, S.K., and Flynn, P.F., "Development of a Single Cylinder Compression Ignition Research Engine," SAE Paper 650733.».
- [52] «Hires, S.D., Tabaczynski, R.J., and Novak, J.M., "The Prediction of Ignition Delay and Combustion Intervals for a Homogeneous Charge, Spark Ignition Engine," SAE Paper 780232.».
- [53] «Blizard, N.C. and Keck, J.C., "Experimental and Theoretical Investigation of Turbulent Burning Model for Internal Combustion Engine," SAE Paper 740191, 1974».
- [54] «Bozza, F., Gimelli, A., Strazzullo, L., Torella, E. et al., "SteadyState and Transient Operation Simulation of a "Downsized" Turbocharged SI Engine," SAE Technical Paper 2007-01-0381, 2007, doi:10.4271/2007-01-0381».
- [55] «Morel, T. and Keribar, R., "A Model for Predicting Spatially and Time Resolved Convective Heat Transfer in Bowl-in-Piston Combustion Chambers," SAE Technical Paper 850204, 1985, doi:10.4271/850204».
- [56] «Poulos, S. and Heywood, J., "The Effect of Chamber Geometry on Spark-Ignition Engine Combustion," SAE Technical Paper 830334, 1983, doi:10.4271/830334.».
- [57] «Morel, T. and Mansour, N., "Modeling of Turbulence in Internal Combustion Engines," SAE Technical Paper 820040, 1982, doi:10.4271/820040».
- [58] «Woschni, G. "A universally applicable equation for the instantaneous heat transfer coefficient in the internal combustion engine," SAE Technical paper, 670931, 1967, doi:10.4271/670931.».
- [59] «Hohenberg, G., "Advanced Approaches for Heat Transfer Calculations," SAE Technical Paper 790825, 1979, doi: 10.4271/790825.».
- [60] «Thermodynamics and Fluid Mechanics Group, & Annand, W., "Heat transfer in the cylinders of reciprocating internal combustion engines," Proceedings of the Institution of Mechanical Engineers, 177(1), 973-996,1963, doi: 10.1243/PIME_PROC_1963_177_069_02».
- [61] «Chen, S.K., and Flynn, P.F., "Development of a Single Cylinder Compression Ignition Research Engine," SAE Paper 650733».

-
- [62] J.B. Heywood "Internal combustion engine fundamentals", Massachusetts Institute of Technology.
- [63] «Bozza, F., De Bellis, V., Tufano, D., Malfi, E. et al., "1D Numerical and Experimental Investigations of an Ultralean Pre-Chamber Engine," SAE Int. J. Engines 13(2):2020. ISSN: 1946-3936, e-ISSN: 1946-3944».
- [64] «C. Poloni, V. Pediroda. GA coupled with computationally expensive simulations: tools to improve efficiency. Genetic Algorithms and Evolution Strategies in Engineering and Computer Science, pages 267-288, John Wiley and Sons, England, 1997.».